STRATEGIES FOR INVERSE PROFILING OF TWO DIMENSIONAL DIELECTRIC SCATTERERS USING ELECTROMAGNETIC ILLUMINATION

Thesis submitted to the
Cochin University of Science and Technology
in partial fulfillment of the
requirements for the degree of
Doctor of Philosophy
under the Faculty of Technology

By

VINU THOMAS

DEPARTMENT OF ELECTRONICS
FACULTY OF TECHNOLOGY
COCHIN UNIVERSITY OF SCIENCE AND TECHNOLOGY
COCHIN 682 022, INDIA
SEPTEMBER 2008

COCHIN UNIVERSITY OF
SCIENCE AND TECHNOLOGY

CERTIFICATE

This is to certify that this thesis entitled **"STRATEGIES FOR INVERSE PROFILING OF TWO DIMENSIONAL DIELECTRIC SCATTERERS USING ELECTROMAGNETIC ILLUMINATION"** is a bona fide record of the research work carried out by Mr. Vinu Thomas, under my supervision in the Department of Electronics, Cochin University of Science and Technology. The results presented in this thesis or parts of it have not been presented for any other degree.

Dr. K. T. MATHEW
(Supervising Teacher)
Professor Emeritus
Department of Electronics
Cochin University of Science and Technology

Cochin 682 022
9th September 2008

DECLARATION

I hereby declare that the work presented in this thesis entitled **"STRATEGIES FOR INVERSE PROFILING OF TWO DIMENSIONAL DIELECTRIC SCATTERERS USING ELECTROMAGNETIC ILLUMINATION"** is based on the original work done by me under the supervision of **Dr. K. T. Mathew** in the Department of Electronics, Cochin University of Science and Technology, and that no part thereof has been presented for any other degree.

VINU THOMAS

Cochin
9th September 2008

Abstract

Electromagnetic tomography has been applied to problems in nondestructive evolution, ground-penetrating radar, synthetic aperture radar, target identification, electrical well logging, medical imaging etc. The problem of electromagnetic tomography involves the estimation of cross sectional distribution dielectric permittivity, conductivity etc based on measurement of the scattered fields. The inverse scattering problem of electromagnetic imaging is highly non linear and ill posed, and is liable to get trapped in local minima. The iterative solution techniques employed for computing the inverse scattering problem of electromagnetic imaging are highly computation intensive. Thus the solution to electromagnetic imaging problem is beset with convergence and computational issues. The attempt of this thesis is to develop methods suitable for improving the convergence and reduce the total computations for tomographic imaging of two dimensional dielectric cylinders illuminated by TM polarized waves, where the scattering problem is defined using scalar equations. A multi resolution frequency hopping approach was proposed as opposed to the conventional frequency hopping approach employed to image large inhomogeneous scatterers. The strategy was tested on both synthetic and experimental data and gave results that were better localized and also accelerated the iterative procedure employed for the imaging. A Degree of Symmetry formulation was introduced to locate the scatterer in the investigation domain when the scatterer cross section was circular. The investigation domain could thus be reduced which reduced the degrees of freedom of the inverse scattering process. Thus the entire measured scattered data was available for the optimization of fewer numbers of pixels. This resulted in better and more robust

reconstructions of the scatterer cross sectional profile. The Degree of Symmetry formulation could also be applied to the practical problem of limited angle tomography, as in the case of a buried pipeline, where the ill posedness is much larger. The formulation was also tested using experimental data generated from an experimental setup that was designed. The experimental results confirmed the practical applicability of the formulation.

Table of Contents

Acknowledgement

I thank God Almighty for his immense blessings all throughout this endeavour.

I would like to express my deepest gratitude to Professor K. T. Mathew for his faithful guidance, valuable advice, immense patience, directive comments, continuous supervision and encouragement throughout the course of this research.

I also express my heartfelt gratitude to the Head of Department of Electronics, CUSAT, Professor K Vasudevan for his constant support and motivation.

I deeply thank Professors K G Balakrishnan, P R S Pillai, P Mohanan, Tessamma Thomas, C K Aanandan, James Kurian, Supriya M H and D Rajaveerappa for their continuous encouragement.

I acknowledge with gratitude the suggestions and comments provided by my co researchers of the Microwave Tomography and Material Research Lab, especially Dr Joe Jacob, Dr Jaimon Yohannan, Anil Lonappan, Dr G Bindu, Dr V Hamsakutty, Praveen Kumar A V, Robin and Ullas.

Special thanks are due to Dr. Thomaskutty Mathew, School of Technology and Applied Sciences, M.G. University, Kerala, Mr Cyriac M. Odakkal, Assistant Professor, VJCET, Muvattupuzha and my colleague and friend Mr. C Gopakumar, for their valuable suggestions and criticism.

I also acknowledge the help rendered by my other co researchers of the Department of Electronics of CUSAT. Thanks are also due to the technical and office staff of the Dept of Electronics, CUSAT, for all the help they have rendered to me.

I also acknowledge the support of my parent institution, the Institute of Human Resource Development, Government of Kerala, for supporting me during my research.

I would also like to thank my parents, my late grand father, my wife

and our three children and all my friends and relatives for their patience, endurance and spiritual support.

CHAPTER 1

Introduction

1.1 Introduction

Inverse problems are ubiquitous in science and engineering and have rightfully received a great deal of attention from applied mathematicians, statisticians and engineers. This is due in part to the importance of applications like biomedical, geophysical and seismic imaging that require the practical solution of inverse problems. It is also due to the recent development of powerful computers and fast reliable numerical methods with which to carry out the solution process.

Inverse problems involve the estimation of certain quantities based on indirect measurement of these quantities. For example seismic exploration yields measurements of vibrations recorded on the earth surface. These measurements are only indirectly related to the subsurface geological formations that are to be determined. In medical computerized tomography, structures within the body are sought to be imaged form measurements of x-rays that have passed through the body. In ground water flow modeling one estimates the material parameters of an aquifer from measurements of pressure of a fluid that immerses the aquifer.

Inverse problems are typically ill posed, as opposed to the well-posed problems more typical when modeling physical situations where the model parameters or material properties are known (forward problems). According to the definition given by Jacques Hadamard [1], the three conditions for a well-posed problem are existence, uniqueness, stability of the solution or solutions. In most inverse problems, the condition of stability is most often violated [2]. In the sense of functional analysis, the inverse problem is represented by a mapping between metric spaces. While inverse problems are often formulated in infinite dimensional spaces, limitations to a finite number measurement, and the practical consideration of recovering only a finite number of unknown parameters, may lead to the problems being recast in discrete form. In this case the inverse problem will typically be ill-conditioned.

Inverse problems can be either linear or non-linear problems [3]. In general all inverse problems maybe expressed in the form

$$m = Gf \qquad (1.1),$$

where m is the measurement made, f is the physical quantity to be estimated and G is the operator matrix. When G is a linear operator, the inverse problem is a linear one. From a theoretical point of view, many linear inverse problems are well understood [3]. When G is a non linear operator, the inverse problem is inherently more difficult to solve. Non linear inverse problems are characterized by multiple solutions [4]. Thus solution procedures for solving non linear inverse problems are liable to get trapped in local optima.

The solution strategies for solving the non linear inverse problem could be deterministic or stochastic. Deterministic methods involve linearizing the inverse problem around a current estimate and solving the problem iteratively, each time improving the correctness of the estimate. The iterative procedure is gradient based, with a cost functional minimized in every iteration. Therefore the deterministic procedures are likely to be trapped in local minima. The stochastic methods, such as Genetic algorithms or Simulated annealing, converge to the global optimum of the solutions. However the stochastic methods are extremely computation intensive, and are not employed when the number of unknowns of the inverse problem is large [5].

1.2 Imaging and Inverse Problems in Electromagnetics

The attempt to image an object that is invisible to the naked eyes is an important aim of scientists in many disciplines. The imaging problem is an in inverse scattering problem, where one attempts to infer the profile of a scattering object from measurement data collected at a distance away from the scattered, as shown in figure 1.1.
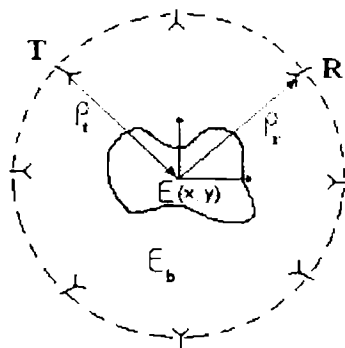

Figure 1.1
The inverse scattering problem of imaging.
Here the cross sectional profile of the object is sought to be reconstructed from the scattered field measurements at the receivers.

In addition to obtaining the shape of an object, a quantitative description of its permittivity, velocity, or conductivity profile is also obtainable from an inverse – scattering experiment. This can be extremely valuable diagnostic information [6].

The advent of X-rays brought much enthusiasm to the scientific community even though it was discovered to have an adverse radiation effect. An X-ray picture is a shadow cast on a photographic film by denser media that are more opaque to X-rays compared with less dense media. Later it was discovered how to make three-dimensional pictures out of a series of shadows cast by X-rays. This is known as X-ray tomography, which later developed to become computer-aided tomography (CAT) [7, 8].

Another very significant modality is the use of nuclear magnetic resonance imaging (MRI). MRI makes use of the fact that spin echoes of protons have different resonance frequencies depending on the ambient static magnetic field. The stronger the magnetic field, the higher is the resonance frequency of the proton spin. Hence, by immersing a body in a static magnetic field that has a linear gradient in a three-dimensional space, the spins echo with different frequencies when excited by a time varying electromagnetic signal. By performing the same experiment again by varying the linear gradient over a number of directions, enough data diversity can be generated so that a two- or three-dimensional image of an object maybe reconstructed [9].

Another modality is ultrasonic imaging [10]. This works almost like X-ray tomography. However, due to the lower frequencies and longer wavelengths of ultrasonic waves, they do not travel exactly in a straight line but diffract around objects. Also there may be multiple – scattering effects within an object when ultrasonic waves enter it. Hence, when ultrasonic images are reconstructed based upon assuming straight rays and no multiple scattering, image distortion arises. An imaging scheme called diffraction tomography (DT) attempts to correct for the diffraction effect but not for the multiple scattering effects [11].

To date electromagnetic (microwave and radio wave) imaging has not found wide medical applications due to its longer wavelength and hence, lower resolution. The wavelength can be reduced by using higher frequencies, but the ensuring material loss is also higher greatly reducing the penetration depth. However, electromagnetic imaging has found a niche in nondestructive evolution, ground-penetrating radar [12], synthetic aperture radar [13], target identification and electrical well logging [14]. Many rugged and constrained environments are not amenable to having X-ray or nuclear magnetic resonance equipment on site. Also, it is often much easier to couple electromagnetic signals into material media at an air- solid interface compared to ultrasonic signals. At such interfaces, the acoustic impedance contrast between the air and the solid is often huge while the electromagnetic impedance contrast is generally lower. The high impedance contrast gives rise to a small transmission coefficient for acoustic signals but a reasonable one for electromagnetic signals. Electromagnetic waves can propagate long distances with little attenuation in air or vacuum. Consequently, electromagnetic waves are extremely useful for remote sensing and

imaging using SAR techniques where the sensor – target separation is often enormous [13].

The inverse- scattering solution is sought from the field perturbation, or the scattered field induced by the presence of the object in the transmitted fields. This solution is often difficult to obtain, especially when multiple scattering effects are present within the object. Such effects can cause the scattered field to be nonlinearly related to the object function to be reconstructed. Object function describes the velocity, permittivity, or conductivity distribution of the object whose profile is to be reconstructed.

The solution to the inverse scattering problem of the Electromagnetic/Microwave imaging problem is non unique because high spatial frequency portions of the object give rise to evanescent waves. These waves are exponentially small at the receiver locations, and in practice are not measurable unless the receivers are extremely close to the scatterer. Hence, the scattering operator is a low-pass filter that removes high spatial-frequency information about the object function. All low-pass filtering operations do not have a unique inverse operation unless some assumptions are made about the solution.

In the past, many methods have been proposed to solve particular classes of inverse scattering problems by making certain assumptions about the object or the scattering process. For example in Computer Aided Tomography, a ray picture is used wherein waves are assumed to propagate in straight lines but all diffraction and multiple-scattering effects are ignored., Diffraction Tomography takes into

account wave diffraction but ignores multiple scattering and assumes the object is small. Methods have been proposed to solve the inverse-scattering problem exactly for one-dimensional objects such as planar layered media [16]. However, such methods are not possible for multi dimensional objects.

The relationship between the scattered field and the scattering object is a non linear one in the inverse scattering problem of electromagnetic imaging. The non linearity increases with multiple scattering effects within the object [17.] as shown in the figure 1.2. Assuming that when only one scatterer 1 is present, the scattered field is $\overline{E_{1s}}$ and when only scatterer 2 is present, it is $\overline{E_{2s}}$. When both scatterers are simultaneously present, the scattered field is not just $\overline{E_{1s}} + \overline{E_{2s}}$, but $\overline{E_{1s}} + \overline{E_{2s}} + \overline{E_{ms}}$, where $\overline{E_{ms}}$ is the result of multiple scattering between the scatterers. Thus linear superposition cannot be employed to solve the scattering problem.
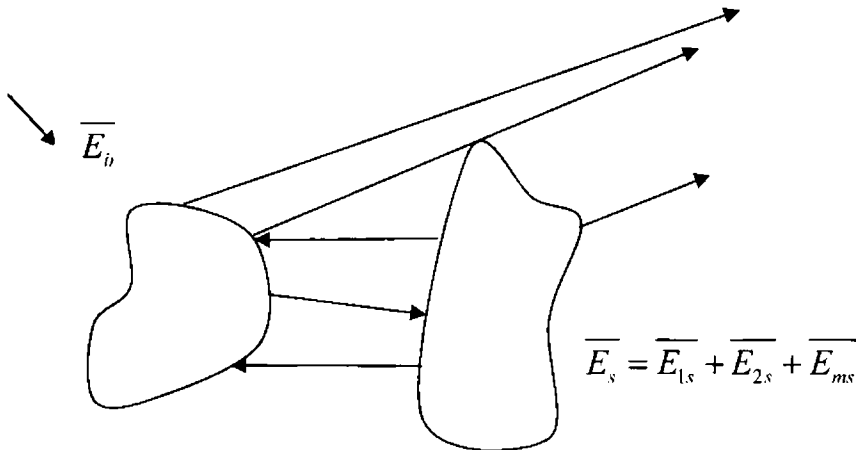

$$\overline{E_s} = \overline{E_{1s}} + \overline{E_{2s}} + \overline{E_{ms}}$$

Figure 1.2
Multiple scattering gives rise to non linearity in the inverse problem that precludes the use of linear

This nonlinear relationship prevents a simple solution to the inverse – scattering problem. One way to solve this nonlinear problem has been to cast it into an optimization format. Here, a cost functional is minimized by applying a gradient – search technique. With such an approach, a forward – scattering solution is sought whenever the gradient is required. Since scattering by an arbitrary object has to be obtained by a numerical method, the nonlinear inverse scattering method is often computationally intensive. However, this method can have an important technological impact if the computational burden is reduced to an acceptable level. Overall, some of the issues that nonlinear inverse scattering theories should address are [18]

- Resolution of the reconstructed object.
- Maximum object contrast that can be accurately inverted
- Maximum object size that can be inverted
- Algorithm speed
- Robustness and numerical stability relative to noisy or imperfect measured data.
- Validity for practical scattering measurement geometries.
- Generality allowing application to other wave equations and scattering phenomena (for example, ultrasound as well as electromagnetic waves)
- Minimizing the amount of a priori information about the object.

One of the most pressing problems for nonlinear inverse – scattering theory is the speed of solution. Solving the inverse problem numerically, often involves solving the forward – scattering problem numerically. However, the latter solution is by itself computationally

intensive. Hence there is considerable need to develop algorithms that can either rapidly solve forward scattering also.

The ways in which microwave interacts with matter will be discussed so as to develop a comprehensive picture of the electromagnetic inverse scattering problem.

1.3 Effect of electromagnetic waves on matter

Electromagnetic waves propagate in uniform dielectrics according to the relation,

$$E = E_0 e^{-yz} \qquad (1.2)$$

where E is the scalar instantaneous electric field in the dielectric at a distance z from the origin, E_0 is the electric field at the origin, and y is the complex propagation constant [19, 20]. The complex propagation constant is defined as

$$y = j\omega\sqrt{\mu\varepsilon} \qquad (1.3)$$

where ω represents the angular frequency, μ the magnetic (complex permeability) and ε the dielectric (complex permittivity) property of the medium. For perfect dielectrics, the magnetic properties are assumed to be those of free space, i.e. purely real with no attenuation or phase shift.

In lossy dielectric materials, the dielectric properties are complex [20] when polarized by an electric field or when subjected to a time harmonic electric field. This is due to the formation of both

conduction and displacement currents. The conduction currents represent the current flow that is in phase with the applied voltage whereas the displacement currents are in phase quadrature with the applied voltage. The complex relative permittivity is represented as,

$$\varepsilon_r = \varepsilon_r' - j\varepsilon_r'' \tag{1.4}$$

where ε_r' is the real part of complex relative permittivity known as the dielectric constant and ε_r'' is the imaginary part known as the dielectric loss. The real and imaginary parts of complex relative permittivity represent the complimentary processes of energy storage and dissipation respectively. Since heat production is related to the frequency and the dielectric loss factor, these are combined to be known as the conductivity σ as,

$$\sigma = \omega\varepsilon_o\varepsilon_r'' \tag{1.5}$$

and loss tangent as, $\qquad \tan\delta = \dfrac{\varepsilon_r''}{\varepsilon_r'}. \tag{1.6}$

1.4 Dielectric polarization

The common feature of dielectric materials is their ability to store electromagnetic energy. This is accompanied by the displacement of positive and negative charges under the influence of the applied electric fields, against the force of atomic and molecular attraction [21]. The mechanism of charge displacement (polarization) depends on the type of dielectric material and the frequency of the applied field. The

electrical equilibrium is disturbed because the applied field causes spatial separation of charges of opposite signs.

Space charge polarization occurs at low-frequency ranges such as VLF and LF bands. It occurs when the material contains free electrons whose displacements are restricted by obstacles such as boundaries. When an electric field is applied, the electrons accumulate on the obstacle, and the resulting charge separation polarizes the material. Entire regions of the material become either positive or negative.

Polarization by dipole alignment occurs at higher frequencies of the HF band and microwave region, at the molecular level. Dielectric heating takes place due to this phenomenon.

Ionic polarization takes place at infrared frequencies due to the separation of positive and negative ions in the molecule.

Electronic polarization occurs at very high frequencies close to the ultraviolet region. The negative electronic cloud surrounding the positive nucleus is displaced in the direction of the applied field.

1.5 Brief sketch of the present study

The aim of this thesis is to develop algorithms for electromagnetic inverse scattering for dielectric scatterers that address the important issues of convergence, computational speed and robustness.

Chapter two describes the background literature about various inverse scattering algorithms that have been developed for tomographic reconstruction of the scatterers.

Chapter three introduces the mathematical formulations for the electromagnetic forward and inverse scattering problems and the discretization model employed.

Chapter four discusses the multi-scaled frequency hopping approach that was formulated for two dimensional dielectric scatterers for addressing the problem of local minima.

Chapter five discusses the Degree of Symmetry $(D.O.S)$ formulations that have been developed for the tomographic reconstruction of two dimensional dielectric pipelines of circular cross section.

Chapter six describes an experimental set up for performing inverse scattering experiments and the experimental verification of the $D.O.S$ formulations.

Chapter seven describes the conclusion arrived at and the possible future directions that might be pursued.

References

1. Hadamard, J., *Lectures on Cauchy's problem in linear partial differential equations,* New Haven, C.T, Yale University Press, 1923.

2. Vogel, C. R., *Computational methods for inverse problems,* SIAM, Philadelphia, 2002.

3. Tarantola, A., *Inverse problem theory and methods for model parameter estimation,* SIAM, Philadelphia, 2005.

4. Kleinman, R.E. and P.M. van den Berg, "Non linearized approach to profile inversion", *Int. J. Imag. Sys. Tech,* Vol.2, 1990, pp 119-126.

5. Franchois, A., *Contribution A La Tomographie Microonde: Algorithms De Reconstruction Quantitative Et Verfications Experimentales,* PhD Thesis, University of Paris, 1993.

6. Chew, W.C., G. P. Otto, W. H. Weedon, J. H. Lin, C. C. Lu, Y. M. Wang and M. Moghaddam, "Non-linear diffraction tomography, the use of inverse scattering for imaging", *Int. J. Imag. Sys. Tech,* Vol.7, 1996, pp 16-24.

7. Raviv, J., F. Greenleaf and C. T. Herman, *Computer Aided Tomography and Ultrasonics in Medicine,* Elsevier, North Holland, 1979.

8. Kak, A.C., "Computerized tomography with X-Ray, emission and ultrasound sources", *Proceedings of IEEE,* Vol. 67, 1979, pp 1245-1272.

9. Krestel, E., *Imaging systems for Medical Diagnosis, Fundamentals and technical solutions: X-Ray diagnostics, Computed Tomography, Nuclear Medical diagnostics,*

Magnetic Resonance Imaging and Ultrasound technology, New York, Wiley, 1990.

10. Lee, H. and G. Wade, *Modern Acoustic Imaging*, New York, IEEE Press, 1986.

11. Devaney, A.J., "A filtered Back projection method for diffraction tomography", *Ultrasonic Imaging*, Vol. 4, 1982, pp 336-360.

12. Maser, K.R., *Ground penetrating radar surveys to characterize pavement layer thickness variations at GPR sites*, Strategic highway research program, 1994.

13. Curlander, J.C. and R.N. McDonough, *Synthetic Aperture Radar: systems and signal processing*, New York, 1991.

14. Chew, W.C and Q. H. Liu, " Inversion of Induction tool measurements using Distorted Born Iterative Method and CG-FFT", *IEEE Transactions on Geo-science and Remote Sensing*, Vol. 32, 1994, pp 878-884 .

15. Chew, W.C., G. P. Otto, W. H. Weedon, J. H. Lin, C. C. Lu, Y. M. Wang and M. Moghaddam, "Non-linear diffraction tomography, the use of inverse scattering for imaging", *Int. J. Imag. Sys. Tech*, Vol.7, 1996, pp 16-24.

16. Bube, K.P and R. Burridge, "The one-dimensional problem of reflection seismology", *SIAM Review*, Vol. 25, 1983, pp 497-559.

17. Chew, W.C., *Waves and Fields in Inhomogeneous Media*, New York, Van Nostrand Reinhold, 1990.

18. Taflove, A., ed., *Advances in Computational Electrodynamics, The Finite Difference Time Domain Method*, Artech House, Boston, 1998.

19. Larsen, L.E. and J. H. Jacobi, *Medical Applications of Microwave Imaging*, IEEE Press, 1985, pp 118-137.

20. Grant, E.H., R. J. Sheppard and G. P. South, *Dielectric behavior of Biological Molecules in Solution*, Oxford-Clarendon Press, 1978.

21. Thurey, J., *Microwaves, Industrial, Scientific and Medical Applications,* Artech House, Boston, 1992.

CHAPTER 2

Review of Literature

In linear inverse scattering theories, approximations are made such that a linear relationship exists between the measured data and the object. Then the information about the object is obtained by solving an associated set of linear equations. This is true for modalities such as Computer Aided Tomography (C.A.T) where the modality employed, X- Ray, is assumed to travel in a straight line path and traverse an object only once. A Back projection algorithm using the projection slice theorem is used to reconstruct the object efficiently in such cases [1, 2]. The Back projection algorithm is based on the WKB (Wentzel, Kramer and Brillouin) approximation which states that at high frequencies, a wave propagates mainly in the forward direction with very little reflection [3]. Here the object, whose tomographic profile is to be reconstructed, is described by its attenuation profile [4], which can be obtained using a radon transformation [5], which have two dimensional as well as three dimensional forms [6].

In projection tomography, one assumes that the waves propagate as straight line rays without diffraction. While this is a correct assumption at the extreme short wavelengths of X-Ray tomography, at the shorter wavelengths employed in ultrasonic and electromagnetic tomography, diffraction is an important phenomenon.

Therefore back projection tomography does not give satisfactory results at the longer wavelengths. Diffraction was incorporated in the context of the Born and Rytov approximations and a reconstruction algorithm was developed accordingly, called diffraction tomography [7-15]. In diffraction tomography, the Born or Rytov approximation is used to calculate the scattered field, when a linear relationship will exist between the scattered field and the object [16]. A Fourier Transform relationship exists between the scattered field and the object function and the Fourier spectrum of the object function maybe recovered using a filtered back propagation algorithm. The object can thus be determined [7]. The Born and Rytov approximations are valid when the contrast of the scatterer is so small that only single scattering is important. Thus when multiple scattering effects are important, as in electromagnetic inverse profiling of objects having strong contrasts, the Diffraction Tomography technique breaks down [17]. Diffraction Tomography is often used in ultrasonic imaging, to achieve good reconstruction when multiple scattering effects are small [18].

Many non linear inverse scattering theories have been proposed to deal with inverse scattering problems involving substantial multiple scattering effects. In one dimension, the problem has been thoroughly studied by a large number of scientists. Several algorithms have been developed which are layer stripping algorithms, in which the reconstruction is done in layers. An elegant algorithm for solving the one dimensional inverse scattering problem is the Gelfand- Levitan Marchenko Method [19]. Bube and Bridge [20] and Sezginer [21] suggested a time domain algorithm which is also a layer stripping technique, called the method of characteristics. Coen et al [22, 23] describes an algorithm for the inverse scattering problem of profiling layered earth.

Ge [24] describes an iterative technique for one dimensional profile inversion. However these algorithms are suitable only for one dimensional objects and have not been verified for higher dimensional inverse scattering [25].

The only general non linear inverse scattering theory valid for higher dimensions that has been verified till date involves numerical methods [3]. These methods are usually iterative and are traditionally expressed as optimization problems. The Born Iterative method was proposed by Wang et al [26] which improved over the simple Born approximation and allowed scatterers of relatively large size or high contrast to be constructed. Moghaddam et al [27, 28] comment on the improved performance of the Born Iterative method in solving an inverse electromagnetic time domain problem. Lu et al [29] describe the use of Born Iterative method to reconstruct a scatterer inside dielectric walls. Abubakar et al suggested an improved robust iterative method for Born Inversion [30]. While the Born iterative method is simple to implement, it has the disadvantage that it does not offer second order convergence [25]. An improved method, the Distorted Born Iterative method (DBIM), was proposed by Chew et al [31, 32]. Leone et al [33] applied the Distorted Born Iterative procedure to reconstruct two dimensional dielectric scatterers for cylindrical geometries. Super resolution was observed by Chen et al [34] for reconstructions employing the Distorted Born Iterative method. The DBIM was employed by Lu et al [35] for electromagnetic and ultrasonic inverse scattering of two dimensional dielectric scatterers. Haddadin and Ebbini [36] employed a multiple frequency distorted Born iteration method for imaging strongly scattering media. A method similar to the Newton Raphson method for solving the electromagnetic inverse scattering problem was

proposed by Joachimowicz et al [37] and Tarantola [38] and is known as the Newton Kantarovich (NK) method. Joachimowicz et al [39] performed a systematic assessment of the effect of experimental and model noise on the NK method and concluded that the NK algorithm is very robust. Franchois and Pichot [40] proposed a Levenberg – Marquardt variant of the Newton Kantarovich method with a cross validation scheme for obtaining the regularization parameter. The DBIM and NK methods have been shown to be computationally equivalent [41-45].

Gradient descent based algorithms have been proposed for the electromagnetic inverse scattering problem of microwave imaging. Though these algorithms have the advantage that the forward problem need not be solved in the iterations, they suffer from the disadvantage that only single profile (permittivity or conductivity) reconstructions are possible, or the background has to be assumed lossless [46]. The modified gradient procedure was proposed by Kleinman et al [47]. Baussard et al [48] employed a regularization scheme based on a Markovian approach for the modified gradient procedure to reconstruct the permittivity profile. Souriau et al [49] developed a modified gradient approach to inverse scattering of binary objects in stratified media. Lambert et al [50] employed a constrained modified gradient method for the retrieval of a buried cylindrical obstacle. Harada et al [45] applied the conjugate gradient descent method for minimizing the cost functional in the inverse scattering problem of diffraction tomography. Moghaddam et al [51] showed that the conjugate gradient method can be used to minimize the cost functional. Rekanos et al [52, 53] combined the finite-element method and the Polak-Ribiere nonlinear conjugate gradient optimization algorithm for reconstructing

the electromagnetic properties of unknown scatterers. Rubaek et al [54] employed a technique based on conjugate gradient least squares method for nonlinear microwave imaging for breast-cancer screening. Reconstructions employing experimental data using a conjugate gradient method with an edge preserving regularization scheme was proposed by Lobel et al [55]. Pastorino [56] discusses the various inversion algorithms for microwave imaging in biomedical, subsurface detection and nondestructive evaluation applications. The contrast source inversion method, which is also a gradient based algorithm, was suggested to provide more robust reconstructions of the dielectric scatterer cross sections [57-60]. The Local shape function T-matrix method was developed to invert strong metallic scatterers [61-64]. It was also found out that the LSF method can reconstruct scatterers with a large dielectric contrast for TE polarized incidence or variable density acoustic waves [65, 66].

Stochastic methods also were employed for microwave imaging. The simulated annealing technique was employed by Franchois, Garnero et al [67, 68] for reconstructing the cross sectional profile of a 2-D dielectric scatterer under TM Polarization. Simulated annealing was also employed by Park et al [69] for microwave imaging of a perfectly conducting cylinder. A Gibbs Markov random field model was employed for active imaging at microwave frequencies by Regazzoni and Foresti [70]. Real Coded Genetic algorithm was employed for the inverse scattering problem of imaging parallel perfectly conducting cylinders [71]. Genetic algorithms have been used for microwave imaging for non destructive evaluation of civil structures [72]. A genetic algorithm based strategy was proposed for the tomographic subsurface detection of defects [73]. Li and Cheng proposed

an application of the genetic algorithm for microwave imaging of a layered dielectric object [74]. Noghanian et al [75] proposed a numerical method based on genetic algorithm optimization for microwave imaging. Qing et al [76] suggested an improved strategy for microwave imaging of parallel perfectly conducting cylinders where the real coded genetic algorithm was employed to provide starting estimates for Newton Kantarovich iterations. A technique where a parallel genetic algorithm was combined with finite domain time difference was applied to the inverse scattering problem of imaging 3-D buried objects by Chen et al [77]. Xiao and Yabe tested the performance of the genetic algorithm for microwave imaging of parallel perfectly conducting cylinders on real data which gave very good results [78]. Caorsi et al [79] applied a hybrid genetic algorithm for nondestructive testing of two dimensional structures. Huang and Mohan [80] employed the micro-genetic algorithm (m-GA) to solve the three dimensional inverse scattering problem of microwave imaging of dielectric objects. However, in general, stochastic methods require a large number of forward solutions to the scattering problem and are hard to apply unless the scattering problem is small [81].

Neural networks have also been employed to solve the inverse scattering problem of microwave imaging. Caorsi and Gamba employed a two layer perceptron neural network trained with the YPROP variant of the backpropagation algorithm which is significantly faster than conventional backpropagation [82]. Wang and Gong [83] employed a coupled gradient neural network to reconstruct the complex permittivity of the biological tissues illuminated by the transverse magnetic (TM) incident waves. Lee employed a neural network with radial-basis functions to the problem of microwave

imaging of cylinders. The RBF-NN was trained by some direct-scattering data sets and thus could predict the images of the target cylinders [84].

The frequency hopping approach has been proposed for the imaging of large inhomogeneous bodies [85-90]. The idea is to collect measurement data over a set of frequencies starting from a low frequency where the inverse scattering problem is solved first. This is then taken as initial guess for iterations at progressively increasing frequencies. Thus better convergent reconstructions are possible when compared to the results obtained from high frequency measurement data alone.

Electromagnetic imaging has also been employed for inverse scattering of dielectric objects buried in inaccessible media. The Distorted Born Iterative procedure was employed by Cui et al [91] to image two dimensional scatterers buried in lossy earth. Higher order extended Born approximation was applied for low frequency detection of two-dimensional buried objects [92]. The finite domain time difference method was used by Toshiyuki et al for microwave imaging of buried objects using time domain data [93]. A differential evolution method was applied by Massa et al [94] to the inverse scattering problem of imaging a buried two dimensional scatterer. Objects embedded in cured concrete could be imaged by using inverse scattering techniques [95]. Vertiy and Gavrilov [96] employed first-order diffraction tomography methods for tomographic reconstructions of two-dimensional objects in millimeter wavelengths band. Guillermin et al [97] proposed a diffraction tomography based algorithm for imaging objects buried in the sediment bottom of deep sea. Chaturvedi and Plumb [98] used the

constrained optimization method for electromagnetic imaging of underground targets. Baussard et al [99] developed an adaptive multiscale reconstruction method for imaging underground scatterers. Helaoui et al [100] proposed a multi illumination approach for buried object detection.

References

1. Raviv, J.J., F. Greenleaf and G. T. Herman, eds., *Computer Aided Tomography and Ultrasonics in Medicine*, Elsevier North Holland, 1979.

2. Herman, G.T, *Image reconstruction from Projections*, New York, Academic Press, 1980.

3. Chew W.C, *Waves and fields in inhomogeneous media*, New York, IEEE Press, 1995.

4. Kak A.C, "Computerized tomography with X-Ray, emission and ultrasound sources", *Proceedings of the IEEE*, Vol. 67, 1979, pp 1245-1272.

5. Radon, J., "Uber die bestimmung von funktionen durch thre intergralwerte langs gewisser mannigfaltigkaiten", *Berichte Saechsische Akademie der Wissenschafien*, Vol. 69, 1917, pp 262-277

6. Deans, S. R., *The Radon Transformation and some of its applications*, New York, Wiley, 1983.

7. Devaney, A. J., " A Filtered Back propagation algorithm for diffraction tomography," *Ultrasound imaging* , Vol. 4, Jan. 1982, pp 336-350

8. Devaney, A. J., "Geophysical diffraction tomography," *IEEE Transaction on Geological Science: Special issue on Remote Sensing,*, Vol. GE-22, Jan. 1984, pp 3-13.

9. Kak A.C, "Tomographic imaging with diffracting and non diffracting sources", *Array Processing systems*, Simon Haykin ed., Prentice Hall, 1984

10. Kaveh, M., M. Soumekh and R. K. Mueller, "Tomographic Imaging via wave equation inversion", *ICASSP 82,* May 1982, pp 1553-1556.

11. Kenue, S.K. and J. F. Greenleaf, "Limited angle diffraction tomography", *IEEE Transactions on Sonics and Ultrasonics,* Vol. SU-29, July 1982, pp 213-217.

12. Lu, Z. Q., M. Kaveh and R. K. Mueller, "Diffraction tomography using beam waves: Z-average reconstruction", *Ultrasonic Imaging,* Vol. 6, Jan. 1984, pp 95- 102.

13. Mueller, R. K., M. Kaveh and G. Wade, " Reconstructive tomography and applications to Ultrasonics", *Proceedings of the IEEE,* Vol. 67, 1979, pp 567-587

14. Nahamoo, D. and A. C. Kak, *Ultrasonic Diffraction imaging,* TR-EE 82-20, School o Electrical Engineering, Purdue University, 1982.

15. Nahamoo, D., S. X. Pan and A. C. Kak, "Synthetic aperture diffraction tomography and its interpolation free computer implementation", *IEEE Transactions on Sonics and Ultrasonics,* Vol. SU- 31, July 1984, pp 218-229.

16. Born, M. and E. Wolf, *Principles of Optics,* New York, Pergamon Press, 6th ed., 1980.

17. Slaney, M., A. C. Kak and L. E. Larsen, "Limitations of imaging with first order diffraction tomography", *IEEE Transactions on Microwave Theory and Techniques,* Vol. MTT-32, 1984, pp 860-874.

18. Lee, H. and G. Wade, *Modern Acoustic Imaging,* IEEE Press, New York, 1986.

19. Chew, W. C., *Waves and fields in Inhomogeneous media,* New York, Van Nostrand Reinhold, 1990.

20. Bube, K. P and R. Burridge, "The one dimensional problem of reflection seismology", *SIAM Review*, 25(4), 497-559.

21. Sezginer, A., *Forward and Inverse Problems in Transient Electromagnetic fields*, Ph.D. Thesis, MIT, 1985.

22. Coen, S., "Inverse scattering of a layered and dispersionless dielectric half-space, Part 1: refelection data from plane waves at normal incidence", *IEEE Transactions on Antennas and Propagation*, AP-29, 1981, pp 298-306,

23. Coen, S. and W. Yu, "The inverse problem of direct current conductivity profile of layered earth", *Geophysics*, 46, 1981, pp 1702-1713.

24. Ge, D. B., "An iterative technique for one dimensional profile inversion", *Inverse Problems*, 3, pp 399-406, 1987.

25. Taflove, A., ed., *Computational Electrodynamics, the Finite Difference Time Domain Method*, Artech House, Boston, 1998.

26. Wang, Y. M. and W. C. Chew, "An iterative solution of two-dimensional electromagnetic inverse scattering problem", *International Journal of Imaging Systems Technology*, Vol. 1, No. 1, 1989, pp 100-108.

27. Moghaddam, M., W. C. Chew, and M. Oristaglio, "Comparison of the Born iterative method and Tarantola's method for an electromagnetic time-domain inverse problem," *Int. J. Imaging Syst. Tech.*, vol. 3, 1991, pp. 318-333.

28. Moghaddam, M. and W. C. Chew, "Study of some practical issues in inversion with the Born iterative method using time-domain data," *IEEE Trans. Antennas Propagat.*, vol. 41, no. 2, 1993, pp. 177-184.

29. Lu, C.C. and X.G. Zhong., "Image reconstruction of two dimensional objects inside dielectric walls", *Microwave and Optical technology letters*, Vol. 36, Issue 2, Dec. 2002, pp 91-95.

30. Abubakar A., Van den Berg P.M., Semenov S.Y, "A robust iterative method for Born inversion", *IEEE Trans Geoscience and Remote Sensing*, 2004, 42, 2, pp 342-354.

31. Chew, W.C and Y.M Wang, "Reconstruction of two-dimensional permittivity distribution using the distorted Born interative method", *IEEE Transactions on Medical Imaging.*, Vol. 9, 1990, pp. 218-225.

32. Chew, W. C. and S.L Chuang, "Profile inversion of a planar medium with a line source of a point source", *IEEE Int. Geoscience and Remote Sensing Society Symposium*, Strasbourg, France, 1984.

33. Leone, Giovanni., R. Persico and R. Pierri, "Inverse scattering under the Distorted Born approximation for cylindrical geometries", *Journal of Optical Society of America*, Vol. 16, Issue 7, pp 1779-1787.

34. Chen, F. C. and W. C. Chew, "Experimental verification of super resolution in non linear inverse scattering", *Applied Physics Letters,* 72, 3080, 1998.

35. Lu, C., J. Lin, W. C. Chew and G. Otto, "Image reconstruction with acoustic measurement using the distorted Born iteration method", *Ultrasonic Imaging*, 1996 April, 18(2), pp 140-156.

36. Haddadin, S. and E. S. Ebbini, "Imaging Strongly scattering media using a multiple frequency distorted Born iterative method", *IEEE Transactions on Ultrasonics, Ferroelectrics and Frequency Control,* 1998, 45(6), pp 1485-1496.

37. Joachimowicz., N., C, Pichot and J. P. Hugonin, "Inverse scattering - An iterative numerical method for electromagnetic imaging", *IEEE Transactions on Antennas and Propagation*, Vol. AP-39, 1991, pp 1742-1752

38. Tarantola, A., " The seismic reflection inverse problem", *Inverse problems of acoustic and elastic waves,* F. Santosa, Y. H. Pao, W. Symes and C. Holland eds., New York, Society of Industrial and Applied Mathematics, 1984.

39. Joachimowicz, N., J. Mallorquí, J. C. Bolomey and A. Broquetas, "Convergence and stability assessment of Newton-Kantorovich reconstruction algorithms for microwave tomography", *IEEE Transactions on medical imaging*, 1998, vol. 17, No. 4, pp. 562-570.

40. Franchois, A. and C. Pichot, "Microwave Imaging – Complex permittivity reconstruction with a Levenberg – Marquardt method", *IEEE Trans. Antennas Propagat.*, vol. 45, no. 2, pp 203 – 215, Feb. 1997.

41. Remis, R.F. and P.M. van den Berg, "On the equivalence of the Newton Kantarovich and Distorted Born methods", *Inverse Problems*, vol. 16, No.1, February 2004, L1-L4.

42. Leone, G., A. Brancaccio and R. Pierri, "Quadratic distorted approximation for the inverse scattering of dielectric cylinders", *Journal of Optical Society of America*, Vol. 18, Issue 3, 2001, pp 600-609.

43. Yao, Y. and Yao Wang, "Frequency domain optical imaging of absorption and scattering distributions by a Born Iterative method", *Journal of Optical Society of America*, Vol. 14, No. 1, 1997, pp 325-342.

44. Joachimowicz, N., J. J. Mallorqui, J. C. Bolomey and A. Broquets, "Convergence and stability assessment of Newton Kantarovich reconstruction algorithms for microwave tomography", *IEEE Transactions on Medical Imaging*, Vol. 17, Issue 4, August 1998, pp 562-570.

45. Harada, H., D. J. N. Wall, T. Takenaka and M. Tanaka, "Conjugate gradient method applied to inverse scattering problem", *IEEE Transactions on Antennas and Propagation*, Vol. 43, NO. 8, Aug. 1995, pp 784-792.

46. Kleinman, R.E., P. M. van den Berg, B. Duchene and D. Lesselier, "Location and reconstruction of objects using a modified gradient approach", *Inverse Problems of Wave Propagation and Diffraction*, Springer Berlin / Heidelberg, 1997, pp 143-158.

47. Cui, T. J., W. C. Chew, A. A. Aydiner and S. Chen, "Inverse Scattering of Two- Dimensional Dielectric objects buried in Lossy Earth using the Distorted Born Iterative Method", *IEEE Transactions on Geoscience and Remote Sensing*, Vol. 39, No:2, February 2001, pp 339-346.

48. Baussard, A, K. Belkebir and D. Premel, "A Markovian regularization approach of the modified gradient method for solving a two-dimensional inverse scattering problem", *Journal of electromagnetic waves and applications*, Vol. 17, No. 7, pp. 989-1008.

49. Souriau, L., B. Duchene, D. Lesselier, and R. Kleinman, "Modified gradient approach to inverse scattering of binary objects in stratified media," *Inverse Problems*, Vol. 12, 1996, pp 463–481.

50. Lambert, M., D. Lesselier, and B. J. Kooij, "The retrieval of a buried cylindrical obstacle by a constrained modified gradientmethod in the H-polarization case and for Maxwellian materials," *Inverse Problems*, Vol. 14, 1998, 1265–1283.

51. Moghaddam, M., W. C. Chew and M. Oristaglio, "Comparison of the Born iterative method and the Tarantola's method for an electromagnetic time domain inverse problem", *International Journal of Imaging systems and Technology*, Vol. 3, 1991, pp 318-333.

52. Rekanos, I.T., M. S. Efraimidou and T. D. Tsiboukis, "Microwave imaging: inversion of scattered near-field measurements", *IEEE Transactions on Magnetics*, Volume 37, Issue 5, Sep 2001, pp 3294 – 3297.

53. Rekanos, I.T., S. M. Panas, and T.D. Tsiboukis, "Microwave imaging using the finite-element method and a sensitivity analysis approach", *IEEE Transactions on Medical Imaging*, Vol. 18, Issue 11, Nov 1999, pp 1108-1114.

54. Rubaek, T, P. M. Meaney, P. Meincke and K. D. Paulsen, "Nonlinear microwave imaging for breast-cancer screening using gauss-newton's method and the CGLS inversion algorithm", *IEEE transactions on Antennas and Propagation*, Vol. 55, No. 8, 2007, pp. 2320-2331.

55. Lobel ,P., C. Pichot , L. Blanc-Féraud and M. Barlaud, "Microwave imaging: Reconstructions from experimental data using conjugate gradient and enhancement by edge-preserving regularization", *International Journal of Imaging Systems and Technology*, Volume 8 Issue 4, 1998, pp 337 – 342.

56. M. Pastorino, "Recent inversion procedures for microwave imaging in biomedical, subsurface detection and nondestructive

evaluation applications", *Imaging Measurement Systems*, Vol. 36, Issues 3-4, October-December 2004, pp 257-269.

57. van den Berg, P. M. and R. E. Kleinman, " A contrast source inversion method", *Inverse Problems,* Vol. 13, 1997, pp 1607-1620.

58. van den Berg, P. M and A. Abubakar, "Microwave tomography using linear and non linear contrast source inversion", *Proceedings of the URSI EMTS,* 2004, pp 1089 – 1091.

59. van den Berg, P. M, A. Abubakar and J. T. Fokkema, "Multiplicative regularization for contrast profile inversion", *Radio Science*, Vol. 38, No. 2, 2003, 23-1 to 23-9.

60. van den Berg, P. M and A. Abubakar, " Contrast source inversion method- state of the art", *PIER,* Vol. 34, 1997, pp 189-218, 2001.

61. Chew, W. C and G. P. Otto, "Microwave imaging of multiple metallic cylinders using shape functions", *IEEE Microwave Guided Wave Letters*, Vol.2, 1992, pp 284-286.

62. Otto, G. P and W. C. Chew, "Inverse scattering of H_z waves using local shape function imaging: A T Matrix formulation", *International Journal of Imaging Systems and Technology*, Volume 5, 1994, pp 22- 27.

63. Weedon, W. H and W. C. Chew, "Time domain inverse scattering using the local shape function (LSF) method", *Inverse Problems*, Vol. 9, 1993, pp 551-564.

64. Otto, G. P and W. C. Chew, "Time Harmonic impedence tomography using the T Matrix method", *IEEE Transactions on Medical Imaging,* Vol. 13, 1994, pp 508-516.

65. Lin, J. H. and W. C. Chew, "Ultrasonic imaging by local shape function method with CGFFT", *IEEE Transactions on*

Ultrasonics, Ferroelectrics and Frequency Control, Vol. 43, 1996, pp 956-969.

66. Lu, C. C and W. C. Chew, "Processing Ipswich data with the local shape function method", *IEEE Antennas and propagation magazine*, Vol. 38, No.3, 1996, pp 51-53.

67. Franchois, A., L. Garnero, C. Pichot and J. P. Hugonin, "Application of the Simulated Annealing technique to Microwave Tomography: preliminary results", *Inverse methods in action*, P. C. Sbatier Ed., Springer-Verlag, Berlin, 1990.

68. Garnero, L., A. Franchois, J. P. Hugonin, C. Pichot, and N. Joachimowicz, "Microwave imaging-complex permittivity reconstruction-by simulated annealing", *IEEE Transactions on Microwave Theory and Techniques*, Vol. 39, Issue 11, Nov 1991, pp1801 – 1807.

69. Park ,S. K., Cheon Seok Park , Jung Woong Ra, "Microwave imaging of a perfectly conducting cylinder with the use of a simulated annealing approach", *Microwave and Optical Technology Letters*, Vol. 11, Issue 5, pp 263 – 265

70. Regazzoni, C. S. and G. L. Foresti, "A Gibbs Markov random field model for active imaging at microwave frequencies", *Signal Processing*, Vol. 47 , Issue 2 (November 1995) pp 169 – 185.

71. Qing, A., "Microwave imaging of parallel perfectly conducting cylinders", *International Journal of Imaging Systems and Technology*, Vol.11, Issue 6, Nov. 2001, pp 365 – 371.

72. Massa, A., M. Donelli , M. Pastorino and A. Rosani, "Microwave imaging for non-destructive evaluation of civil structures", *Insight - Non-Destructive Testing and Condition Monitoring*, Vol. 47, Issue 1, January 2005, pp 11-14.

73. Benedetti, M., M. Donelli, G. Franceschini, A. Massa, and M. Pastorino, "Evaluation study of the effectiveness of the integrated genetic-algorithm-based strategy for the tomographic subsurface detection of defects", *Journal of Optical Society of America*, Vol. 23, Issue 6, 2006, pp. 1311-1325.

74. Li , C. L and Y. Y. Cheng, "Application of the genetic algorithm for microwave imaging of a layered dielectric object via the regular shape expansion technique", *International Journal of Imaging Systems and Technology*, Vol. 10, Issue 4, Jul 1999, pp 347 – 354.

75. Noghanian, S., A. Sabouni and S. Pistorius , "A numerical approach to microwave imaging based on genetic algorithm optimization", *Proceedings of SPIE, the International Society for Optical Engineering, Conference on Health monitoring and smart nondestructive evaluation of structural and biological systems V*, vol. 6177, 2006, pp. 1B.1-1B.12.

76. Qing, A., K. Lee and S. Yang, "An improved algorithm for microwave imaging of parallel perfectly conducting cylinders", IEEE *Antennas and Propagation Society International Symposium*, 2000, Vol. 3, pp 1772 – 1775.

77. Chen, X., D. Liang and K. Huang, "Microwave imaging 3-D buried objects using parallel genetic algorithm combined with FDTD technique", Journal of electromagnetic waves and applications, Vol. 20, no13, 2006, pp. 1761-1774.

78. Xiao, F. and H. Yabe, "Computational Electromagnetics. Microwave Imaging of Perfectly Conducting Cylinders from Real Data by Micro Genetic Algorithm Coupled with Deterministic Method", *IEICE Transactions on Electronics*, Vo. E81-C, No.12, 1998, pp 1784-1792.

79. Caorsi, S., A. Massa, Andrea M. Pastorino and M. Donelli, "Improved Microwave Imaging Procedure for Non-Destructive Evaluations of Two-Dimensional Structures", *Technical Report DIT-03-040, Informatica e Telecomunicazioni, University of Trento*, 2003.

80. Huang, T. and A. S. Mohan, "Microwave Imaging of Three-Dimensional Dielectric Objects", *IEICE Transactions on Communications* 2005 E88-B(6), pp 2369-2376.

81. W. C. Chew, "Imaging and inverse problems in electromagnetics", *Advances in Computational Electrodynamics: the Finite-Difference Time-Domain Method, Allen Taflove (Editor)*, Artech House, 2003.

82. Caorsi. S and P. Gamba, "Electromagnetic detection of dielectric cylinders with a neural network approach", *IEEE Transactions on Geoscience and Remote sensing*, Vol. 37, No. 2. 1999.

83. Wang , Y. and X. Gong, "A neural network approach to microwave imaging", *International Journal of Imaging Systems and Technology*, Vol. 11 Issue 3, 2001, Pages 159 – 163.

84. Lee, K. C., "A neural-network-based model for 2D microwave imaging of cylinders", *International Journal of RF and Microwave Computer-Aided Engineering*, Volume 14 Issue 5, August 2004, pp 398 – 403.

85. Chew, W.C. and J. H. Lin, "A frequency-hopping approach for microwave imaging of large inhomogeneous bodies", *Proceedings of the Antennas and Propagation Society International Symposium*, AP-S. Digest, Volume 3, Jun 1995, pp 1610 – 1613.

86. Chew, W.C. and J. H. Lin, "A frequency-hopping approach for microwave imaging of large inhomogeneous bodies", *IEEE Microwave guided wave letters*, Vol. 5, 1995, pp 439-441.

87. Marklein, R., Balasubramanian, K., Qing, A. and Karl J Langenberg, "Linear and nonlinear iterative scalar inversion of multi-frequency multi-bistatic experimental electromagnetic scattering data", *Inverse Problems,* Vol.17, 2001, pp 1597-1610.

88. Belkebir, K., R. E. Kleinman and C. Pichot, "Microwave imaging-Location and shape reconstruction from multifrequency scattering data", *IEEE Transactions on Microwave Theory and Techniques*, Vol. 45, Issue 4, Apr 1997, pp 469 – 476.

89. Semenchik, V., V. Pahomov and S. Kurilo, "Multifrequency microwave imaging", *Proceedings of the Fifth International Kharkov Symposium on Physics and Engineering of Microwaves, Millimeter, and Submillimeter Waves, 2004. MSMW 04*, Vol. 1, pp 193- 195.

90. Belkebir, K. and M. Saillard, "Special section: Testing Inversion Algorithms against Experimental Data", *Inverse Problems*, Institute of Physics Publishing, vol. 17, 2001, pp 1565-1571.

91. Cui, T. J., W. C. Chew, A. A. Aydiner and S. Chen, "Inverse Scattering of Two- Dimensional Dielectric objects buried in Lossy Earth using the Distorted Born Iterative Method", *IEEE Transactions on Geoscience and Remote Sensing*, Vol. 39, No:2, February 2001, pp 339-346.

92. Cui, T. J., Y. Qin, G. L. Wang and W. C. Chew, " Low Frequency detection of two-dimensional buried objects using high-order extended Born approximation", *Inverse Problems*, 20, 2004, S41-S62.

93. Toshiyuki, T. , T. Takashi and H. Jia, "Microwave Imaging of Buried Objects using Time Domain Data", *Institute of Electronics, Information and Communication Engineers Technical Report*, Vol.100,2001, No. 583, pp 97-103.

94. Massa, A., M. Pastorino and A. Randazzo, "Reconstruction of two-dimensional buried objects by a differential evolution method", Inverse Problems 20, 2004, S135-S150.

95. Chang ,M., P. Chou and H. Lee, "Tomographic microwave imaging for nondestructive evaluation and object recognition of civil structures and materials", *29th Asilomar Conference on Signals, Systems and Computers (2-Volume Set)*, p. 1061.

96. Vertiy, A. A. and S. P. Gavrilov, "Modeling of Microwave Images of Buried Cylindrical Objects", *International Journal of Infrared and Millimeter Waves*, Springer New York, Vol. 19, Number 9 September, 1998, pp 1201-1220.

97. Guillermin, R., P. Lasaygues, J. P. Sessarego and A Wirgin, "Imaging an object buried in the sediment bottom of a deep sea by linearized inversion of synthetic and experimental scattered acoustic wavefields", *Inverse Problems*, 16, 2000, pp 1777-1797.

98. Chaturvedi. P. and R. G. Plumb, "Electromagnetic Imaging of Underground Targets using Constrained Optimization", *IEEE Transactions on Geoscience and Remote Sensing*, Vol. 33, No. 3, pp 551-561, May 1995.

99. Baussard. A, E. L. Miller, D. Lesselier, "Adaptive Multiscale Reconstruction of Buried Objects", *Inverse Problems*, 20, 2004, S1-S15.

100. Helaoui, L., J. B. H. Tahar and F. Choubani, "Multi-source illumination approach for Buried Objects Exploration",

$$\boxed{}$$

Formulation of the Problem

3.1 Introduction

In the inverse scattering problem of Electromagnetic (RF) and Microwave imaging, one attempts to infer the properties of the scatterer which is located in an investigation domain D_{obj} that includes all possible locations of the scatterer, from the scattered field measurements which are made in the measurement domain D_M, which is outside the investigation domain. The forward scattering problem, where the object and the incident field that illuminates the investigation domain are assumed to be known and the measured scattered field is assumed to be unknown, maybe modeled using integral equation formulations. The solution to this forward scattering problem is needed in many inverse scattering techniques and also for generating the simulated synthetic measured scattered field data for the inversion. The formulations leading to the mathematical modeling of the forward scattering problem is discussed next. In this work the imaging of two dimensional dielectric scatterers is considered. Hence the discussions are limited to the case of the unknown object whose tomographic image is to be reconstructed being a 2-D dielectric scatterer.

Integral equation formulations have attracted the interest of mathematicians for a long time. Most integral equations do not have a

closed form solution. However they can often be discretized and solved on a digital computer. Proof that a solution exists by discretization of the integral equation was first presented by Fredholm [1]. The volume integral method is employed for the modeling of the forward scattering problem in microwave imaging [2]. The volume integral equation offers a good physical picture of the mechanism that gives rise to scattering, providing an insight as to how approximate scattering solutions can be obtained. In this method, the unknowns in the problem are expressed in terms of volume currents flowing in the inhomogeneity. The volume current consists of conduction as well as displacement currents induced by the total electric field. An integral equation can then be formulated from which the total field is solved.

Certain physical phenomena maybe expressed by the scalar wave equation, such as the acoustic waves and the Schrödinger waves. Certain electromagnetic problems also maybe described by the scalar wave equation. In the case of a two dimensional scatterer in the investigation domain, the electromagnetic scattering can be modeled by a scalar wave equation when the incident field used for illuminating the scatterer is TM polarized as in figure 3.1. By a two dimensional scatterer, one refers to the fact that the complex permittivity does not vary along one of the three Cartesian coordinate axes.

When the incident wave is TM polarized, the magnetic field is transverse to the axis of the scatterer, or in other words, the electric field is parallel to the cylinder axis.
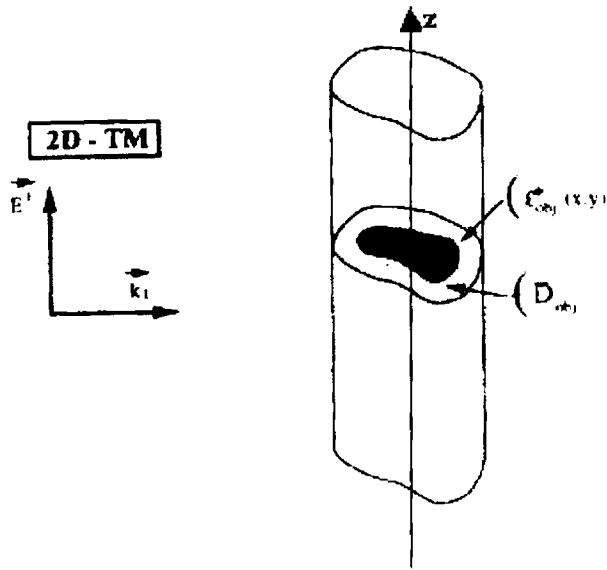
Figure 3.1
Two dimensional dielectric cylinder
illuminated by a TM polarized source

The scalar wave equation is considered here, for the case of the two dimensional scatterer illuminated by TM polarized electromagnetic wave. In the equations, a time factor of $e^{j\omega t}$ is understood. In a homogenous medium containing a source $q(r)$, a scalar wave $\psi(r)$ (electric field component parallel to the cylinder axis), satisfies the homogenous wave equation of the form

$$(\nabla^2 + k_b^2)\psi(r) = q(r), \tag{3.1}$$

where the wave number k_b represents the wave number of the background medium, i.e., the spatial frequency of the plane wave and is a function of the wavelength λ_b or

$$k_b = \frac{2\pi}{\lambda_b} = \omega^2 \mu_b \varepsilon_b , \tag{3.2}$$

where μ_b being the permeability and ε_b being the complex permittivity.

For imaging, an inhomogeneous medium is of interest and hence the more general form of the wave equation is considered,

$$(\nabla^2 + k^2(r))\psi(r) = q(r) , \tag{3.3}$$

where $k^2(r) = \omega^2(r)\mu(r)\varepsilon(r)$, ω being the angular frequency of the incident wave that illuminates the scatterer, μ being the permeability and ε being the complex permittivity. Here $k^2(r)$ represents the inhomogeneous medium over a finite domain D_{obj}. Both medium and the scatterer are considered to be non magnetic, so $\mu = \mu_b = 1$, everywhere in the investigation domain and measurement domain.

The equation (3.4) is rewritten as

$$(\nabla^2 + k_b^2)\psi(r) = q(r) - [k^2 - k_b^2(r)]\psi(r) \tag{3.4}$$

The right hand side of equation (3.4) can be considered to be an equivalent source. An integral formulation for finding the unknown total field for the forward problem can now be formulated in terms of the Greens function. The Greens function of a wave equation is defined as the solution of the wave equation for a point source. When the solution of a wave equation due to a point source is known, then

the solution due to a general source can be obtained by the principle of linear superposition.

The Greens function is given by

$$(\nabla^2 + k^2(r))g(r,r') = -\delta(r-r'),\qquad (3.5)$$

with $g(r,r')$ being the solution for the wave equation for a point source at r'. By reciprocity, $g(r,r') = g(r',r)$. Any arbitrary source $q(r)$ maybe represented as

$$q(r) = \int dr' q(r')\delta(r-r')\ .\qquad (3.6)$$

This is actually a linear superposition of point sources in mathematical terms. Hence the solution to equation (3.1) is therefore

$$\psi(r) = -\int dr' g(r,r') q(r-r'),\qquad (3.7)$$

which is an integral linear superposition of the solution of equation (3.5). Since the Greens function corresponding to the differential operator on the left hand side of equation (3.5) is known, by the principle of linear superposition one can write

$$\psi(r) = -\int dr' g(r,r') q(r') + \int dr' g(r,r')[k^2(r') - k_b^{\ 2}]\psi(r').\qquad (3.8)$$

In the above equation the first term is just the field due to the source in the absence of any inhomogeneity, and hence is the incident

field (i.e., the component of the incident electric field parallel to the cylinder axis). Therefore the above equation can be rewritten as

$$\psi(r) = \psi^{inc}(r) + \int dr' g(r,r')[k^2(r') - k_b^2]\psi(r').$$ (3.9)

In the above equation, if the total field $\psi(r')$ inside the investigation domain, which contains the inhomogeneity, is known, then $\psi(r)$ maybe calculated everywhere. However $\psi(r)$ is unknown at the point r'. Therefore this equation is a Fredholm integral equation of the second kind, where the unknown quantity $\psi(r)$ is both inside and outside the integral operator. The second term on the right hand side of the equation (3.9) is the scattered field due to the inhomogeneity $k^2(r) - k_b^2$. For the case of a two dimensional dielectric scatterer (the axis of the cylinder being oriented in the z- direction) illuminated by a TM polarized electromagnetic wave, the Greens function is the solution to the equation

$$(\nabla^2 + k^2(r))g(r,r') = -\delta(x - x')\delta(y - y').$$ (3.10)

It can be shown that the solution to the above equation is given by

$$g(r,r') = \frac{j}{4} H_0^2(k_b(r - r'))$$ (3.11)

where H_0^2 is the Hankel's function of the zeroth order and second kind, $r = [x, y]$ and $r' = [x', y']$ [2, 3, 4].

In three dimensions, the Greens function is given by

$$g(r,r') = -\frac{e^{jk_b|r-r'|}}{4\pi|r-r'|}.$$
(3.12)

For modeling the general three dimensional electromagnetic scattering problems, the integral equation is of the form

$$E(r) = E^{inc}(r) + \int dr' \overline{G}(r,r')[k^2(r') - k_b^2]E(r')$$
(3.13)

where E and E^{inc} are the total and incident vector electric fields respectively and $\overline{G}(r,r')$ is the dyadic Greens Function, which relates the electric field vector $E(r)$ to the current density $J(r)$ via

$$E(r) = j\omega\mu \int_V \overline{G}(r,r').J(r')dr'$$
(3.14)

and is given by the dyad

$$\overline{G}(r,r') = [I + \frac{\nabla\nabla}{k_b^2}]g(r,r').$$
(3.15)

The integral equations may thus be written for the vector integral equations of the 2-D TE and 3-D cases as

$$E(r) = E^{inc}(r) + \int dr'(1 + \frac{1}{k_b^2} grad\, div')\frac{j}{4}H_0^2(k_b|r-r'|)[k^2(r') - k_b^2]E(r')$$

(3.16)

and

$$E(r) = E^{inc}(r) + \int dr' (1 + \frac{1}{k_b^2} grad\ div') \frac{e^{jk_b|r-r'|}}{4\pi |r-r'|} [k^2(r') - k_b^2] E(r')$$

$$(3.17)$$

3.2 Approximate solution of the forward scattering problem

The solution to the volume integral equation has to be solved for numerically. This is in general computationally intensive. For many problems, however, when the scattering from the inhomogeneity is weak, it suffices to derive approximate solutions to the scattering problem. One of the popular approximations is the Born approximation [5]. In the case when $k^2 - k_b^2$ is small, or when the contrast of the scatterer is weak so that the second term of the equation (3.9) or (3.13) is small when compared to the first term, the total field maybe approximated by the incident field.

i.e.,

$$E(r) = E^{inc}(r) , \qquad (3.18)$$

where the field could be either the scalar field of (3.9) or the vector field of (3.13). The volume integral equation therefore maybe approximated as

$$E(r) = E^{inc}(r) + \int dr' \overline{G}(r,r')[k^2(r') - k_b^2] E^{inc}(r') . \qquad (3.19)$$

This is the first order Born approximation. It is also the first order approximation in the Taylor's series approximation of $E(r)$ using $(k^2 - k_b^2)$ as a small parameter [2].

The Born approximation assumes single scattering. As per the equation (3.19), the incident wave enters the scatterer with no distortion, induces a polarization current proportional to $(k^2 - k_b^2)E^{inc}$ and causes a re-radiation, or scattering. Since the incident field is unaffected when it gives rise to the scattered field, Born approximation violates energy conservation. However, because of the symmetry of the dyadic Greens function, reciprocity is still preserved under the Born approximation. The constraint on the Born approximation to be valid for the scalar wave case or the case of a TM wave impinging on an infinite dielectric cylinder is

$$k_b^2 L^2 \Delta \varepsilon_r \ll 1 . \tag{3.20}$$

Thus for this case the Born approximation becomes exceedingly good at low frequencies, since the constraint can be met even when $\Delta \varepsilon_r > 1$ if $k_b L \ll 1$. However this is not true for the vector electromagnetic field [2].

3.3 Numerical solution of the forward scattering problem

Defining $k^2(r) - k_b^2$ as the object contrast function $c(r)$, the integral equation (3.9) now maybe rewritten as

$$\psi(r) = \psi^{inc}(r) + \int_{D_{obj}} dr' g(r,r') c(r') \psi(r'), r \in D_{obj} \qquad (3.21)$$

$$\psi^s(r) = \int_{D_{obj}} dr' g(r,r') c(r') \psi(r'), r \in D_M \qquad (3.22)$$

The first equation gives the total field in the object domain D_{obj} and is called the state equation. The second equation gives the measured scattered field in the measurement domain D_M and is known as the observation equation. There is no restriction to the shape or dimension of D_{obj} or D_M. The only condition to be satisfied is that D_{obj} should be large enough to include all possible object locations. It is usually considered to be a square or a rectangle for the ease of computations. The measurement domain should be outside the investigation domain. A typical measurement setup is shown in figure 3.2. The use of the moment method can transform the integral relations to matrix relations [6].
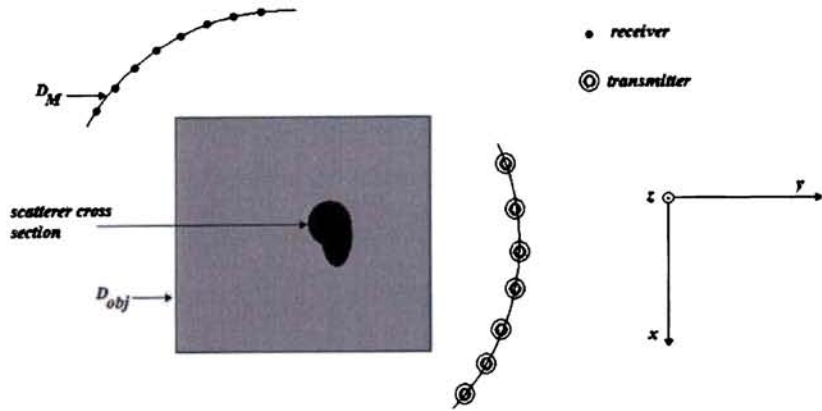
Figure 3.2
Typical measurement setup

By choosing pulse basis functions and point matching, the object domain maybe divided into N elementary square shaped cells. In each of the cells, the total electric field and complex permittivity are assumed to be constant. The relation between the values of the scattered field at the measurement domain (which is assumed to have N_r measurement points for a particular transmitter antenna) and the values of the total field in the N elementary cells is

$$\psi^s_{\,v}(r_m) = \sum_{j=1}^{N} g(r_m, r_j) c(r_j) \psi_v(r_j), \, m = 1, 2, ... N_r \qquad (3.23)$$

while the total electric field in the N cells is the solution of the

$$\psi_v^{inc}(r_n) = \sum_{j=1}^{N}[\delta_{nj} - g(r_n, r_j)c(r_j)]\psi_v(r_j), n = 1, 2, \ldots N \qquad (3.24)$$

where v represents the view in a multi incidence configuration and the object is successively illuminated from different angles by different incident fields. This is done to collect a larger amount of measured scattered field data, which will aid in reconstruction of better profiles of the scatterer. ψ_v^s represents the measured scattered field for the view v, ψ_v and ψ_v^{inc} represent the total and incident electric fields in the investigation (object) domain and $\delta_{nj} = \{1, n \neq j \\ = \{0, n = j$. The contrast vector $c(r)$ and the total field vector $\psi_v(r)$ are lexicographically arranged as in figure 3.3.

1	2	3		N1-2	N1-1	N1
N1+1	N1+2	N1+3		–	2N1-1	2N1
–	–	–		–	–	–
–	–	–		–	–	–
–	–	–		–	–	–
–	–	–		–	–	–
–	–	–		–	–	–
N-N1+1	N-N1+2	N-N1+3		N-2	N-1	N

Figure 3.2
Lexicographical ordering of a 2-D array into a vector
The array is of dimension $N1$ by $N2$ and the ordered
vector will be of dimension
$N = N1 \times N2$.

The equations (3.23) and (3.24) maybe respectively rewritten in the form of matrix equations

$$[\psi^s_v] = [Gr_{v,om}][C][\psi_v] \qquad (3.25)$$

$$[\psi_v^{inc}] = [I - Gr_{oo}C][\psi_v] \qquad (3.26)$$

Here $[\psi^s_v]$ is the measured scattered field vector of dimension N_r and $[Gr_{v,om}]$ is the integrated Greens function matrix of dimension $N_r \, x \, N$ that relates a point in the investigation domain to a point in the measurement domain, for the view v . $[Gr_{oo}]$ is the integrated Greens function Matrix when both points are in the investigation domain. $[C]$ is a diagonal Matrix of dimension N by N such that $C(i,i) = c(i), i = 1,2...N$. $[\psi_v]$ and $[\psi_v^{inc}]$ are total and incident field vectors respectively, formed by lexicographically arranging the electric field values in the investigation domain. The singularity of the Greens function matrix $[Gr_{oo}]$ when both points coincide is integrated by considering the cell to be disk shaped instead of a square.

The analytical expression employed for the integration at the singularities, which is when the argument of the Greens function is zero, is given by [7]

$$\frac{j}{4} \int_0^{2\pi} \int_0^a H_0^2(k_b\rho)\rho'd\rho'd\phi' = \frac{j}{2k_b^2}[\pi k_b a H_1^2(k_b a) - 2j] \; . \quad (3.27)$$

where the radius of the cell a is chosen equal to the square side of the cell divided by $\sqrt{3}$ since the integrals over a square and a circle of any polynomial function of order 3 are then exactly related [8].

Another case is when the object lies in an inaccessible medium and the measurement is done in another medium, as done in the inverse profiling of buried objects. The development of imaging techniques for investigation of physically inaccessible objects is of much importance in areas such as oil exploration, seismic imaging, non destructive evaluation, buried object detection etc. In most of these cases, reliable information about the physical properties of the inaccessible target is desired in addition to detection of the target. All these problems may be classified as electromagnetic inverse problems when the characterization of the unknown target is computed by considering electromagnetic illumination and employing the values of the scattered electromagnetic field. Here the forward problem is formulated employing the domain integral equations, where

$$\psi(r) = \psi^{inc}(r) + \int_{D_{obj}} c(r')g_{m_2 m_2}(r,r')\psi(r')dr', r \in D_{obj} \qquad (3.28)$$

is the state equation and

$$\psi^s(r) = \int_{D_{obj}} c(r')g_{m_1 m_2}(r,r')\psi(r')dr', r \in D_M \qquad (3.29)$$

is the observation equation, where the object whose profile is to be formed is located in the inaccessible medium with permittivity ε_{m_2} (for example, soil), and the measurements are made in the medium with permittivity ε_{m_1} (usually air). The investigation domain lies entirely in the inaccessible medium. When the investigation domain is selected as a rectangle (which is the usual case, for the ease of

computations), and when the scatterer is a 2-D dielectric scatterer whose axis is oriented in the z- direction and illuminated by a TM electromagnetic source in the z- direction (i.e. the cross section of the scatterer lying in the x-y plane), the expression for the Greens functions $g_{m_2 m_2}$ and $g_{m_1 m_2}$ are

$$g_{m_2 m_2}(r,r') = \frac{j}{4\pi} \int_{-\infty}^{+\infty} dk_x k_{m_2 y}^{-1} [e^{jk_{m_2 y}|y-y'|} + R_{m_2 m_1} e^{-jk_{m_2 y}(y+y'-2h)}] e^{jk_x(x-x')}$$

(3.30)

where r and r' lies in D_{obj} and

$$g_{m_1 m_2}(r,r') = \frac{j}{4\pi} \int_{-\infty}^{-\infty} dk_x k_{m_2 y}^{-1} T_{m_2 m_1} e^{j[k_{m_1 y}(y_r-h)-k_{m_2 y}(h-y')]} e^{jk_x(x_r-x)}$$

(3.31)

where r lies in D_M and r' in D_{obj}. $k_{m_1 y, m_2 y} = \sqrt{k^2 \varepsilon_{m_1, m_2} - k_x^2}$ and $R_{m_2 m_1}$ and $T_{m_2 m_1}$ are reflection and transmission coefficients of a TM wave respectively, given by [9, 10]

$$R_{m_2 m_1} = \frac{k_{m_2 y} - k_{m_1 y}}{k_{m_2 y} + k_{m_1 y}} \ , \ T_{m_2 m_1} = 1 + R_{m_2 m_1}$$

(3.32)

In the above equations, the rectangular investigation domain is assumed to begin from a depth of h from the interface between media m_1 and m_2. The observation and state equations are discretized using pulse basis functions and point matching method of moments. The corresponding matrix representations for the state and observation equations for a transmitter view v maybe respectively written as

$$[\psi_v^{inc}] = [I - Gr_{m2m2}C][\psi_v] \qquad (3.33)$$

and

$$\psi^s_{\ v} = Gr_{v,m_1m_2}C\psi_v , \qquad (3.34)$$

where ψ_v , ψ_v^{inc} and c are the total electric field vector, the incident

field vector and the complex permittivity contrast vector respectively,

of dimension $N x 1$,all in lexicographical order, N being the number of

cells in D_{obj}. $Gr_{m_2m_2}$ and Gr_{v,m_1m_2} are the matrices of properly integrated

Greens functions of dimension $N x N$ and $N_r x N$ respectively where

N_r is the number of receivers in D_M for a particular view v. C is the

diagonal matrix of dimension $N x N$ whose entries are the elements of

the contrast vector c [11].

3.4 Inverse scattering techniques

The methods to solve the inverse problem of Electromagnetic

(RF) and Microwave imaging could be broadly classified as

deterministic and stochastic. They tackle the nonexistence of the

inverse scattering problem by redefining it as the minimization of a

cost functional. The deterministic algorithms seek to solve the inverse

scattering problem by linearizing it around a current estimate and then

seeking progressively better estimates of the solution. However, due to

the nonlinearity of the inverse scattering problem, there is a risk that

the solution gets trapped in a local minimum. The deterministic

algorithms include those that seek repeated exact field computations

for the forward problem, such as Born Iterative Method (BIM)

Distorted Born Iterative Method (DBIM) and Newton Kantarovich (NK) Method, and those that are gradient based where successive approximations of the configuration and the excited fields are obtained simultaneously [12]. However for reconstruction of objects buried in a half space or multi layered media, gradient based techniques can reconstruct only a single profile (either permittivity or conductivity), or the background has to be constrained as lossless [9]. The stochastic methods, though globally convergent, are extremely computation intensive, especially when the number of unknowns is high. In this work, the DBIM and NK techniques have been employed for the inverse scattering problem of electromagnetic imaging and are discussed next.

In the inverse scattering experiment of electromagnetic microwave imaging, only the measured scattered field vector is available for the inverse profiling of the scatterer, given by

$$\psi^s(r) = \psi(r) - \psi^{inc}(r), r \in D_M ,$$ (3.35)

where the scatterer lies entirely in D_{obj}. The observation equation cannot be directly solved for the cross sectional profile of the object $k^2(r)$, since the total electric field in D_{obj}, $\psi(r)$, is also unknown and is a function of $k^2(r)$ itself. Therefore the integral is a non linear functional of $k^2(r)$. Thus there is a non linear relationship between the scattered field and the scattering object. The physical reason of this non linearity can be attributed to multiple scattering effects within the scattering object. The multiple scattering, and hence

the non linearity of the inverse scattering problem, increases when the object contrast and size increases [13, 14].

The problem can be linearized by using the Born approximation as,

$$\psi^s(r) = \int_{D_{obj}} dr' g(r,r') c(r') \psi^{inc}(r'), r \in D_M \tag{3.36}$$

The above equation is now linear in c and can be solved for the object contrast. The error in the above equation can be shown to be of the order of c^2. However the Born approximation is poor when the scattered field is not weak when compared to the incident field. This occurs when the dielectric contrast of the scatterer with respect to the surrounding medium is large or when the scatterer is large compared to the wavelength.

One way to overcome this problem is to seek increasingly better estimates of $\psi(r)$. For this, the zeroth-order estimate to $c(r)$ is found first using the Born approximation. This estimate $c_0(r)$ is then used to calculate the zeroth-order estimate of the scattered field, $\psi^s_0(r)$. The estimated object contrast is then employed in the state equation, together with $\psi^{inc}(r)$ to obtain a better estimate of the total field $\psi(r)$ within the scatterer. The new total field is denoted as $\psi_1(r) = \psi^{inc}(r) + \psi^s_0(r)$. By so doing, a new approximation for the scattered field may be obtained, given by

$$\psi^s(r) = \int_{D_{obj}} dr' g(r,r') c(r') \psi_1(r'), r \in D_M \tag{3.37}$$

With $\psi_1(r)$ known, equation (3.37) is a linear integral equation in $c(r)$ and hence, can be solved as a linear inverse problem. This method yields a new object contrast, denoted by $c_1(r)$, which is then used to obtain a better estimate of $\psi(r)$ within the scatterer. This procedure is repeated until convergence is reached. This procedure is called the Born iterative method (BIM), for solving the inverse problem. This method improves over the simple Born approximation and allows scatterers of relatively large size or high contrast to be constructed [15].

While the Born iterative method is simple to implement, it may not be the best method to solve the nonlinear inverse-scattering problem because it does not offer second-order convergence. An improved method with second-order convergence is the distorted Born iterative method (DBIM).With DBIM, the background medium is not constrained to be homogeneous and is updated in each iteration[16]. This creates the added difficulty that the Green's function is not available in closed form and must be sought via a numerical method. However, DBIM usually converges faster than BIM and works better for objects with large contrast. This advantage is tempered by the more robust performance of BIM in the presence of noise. Nevertheless, a convergent solution can be achieved with DBIM.

The expression for the total field is now expressed as

$$\psi(r)=\psi^{inc,b}(r)+ {}_{D_{obj}}\!\int dr'\,g_b\left(r,r'\right)[k^2(r')-k_b^2]\psi\left(r'\right) \qquad (3.38)$$

where $\psi^{inc,b}(r)$ is the incident field when the background $k_b(r)$ is not constrained to be homogeneous. It is to be noted that

$$\psi^{inc,b}(r) = \psi^{inc}(r) + \omega^2 \mu \int dr' g_0(r,r') \varepsilon_b(r') \psi^{inc,b}(r') \qquad (3.39)$$

where $g_0(r,r')$ is the Greens function with the background assumed to be homogeneous. The scattered field due to the difference between $k^2(r)$ and $k_b^2(r)$ in the object domain is denoted by $\psi^{s,b}(r)$ and is given by

$$\psi^{s,b}(r) = \int_{D_{obj}} dr' g_b(r,r') c(r') \psi(r'), r \in D_M \qquad (3.40)$$

where,

$$\psi^{s,b}(r) = \psi(r) - \psi^{inc,b}(r) \qquad (3.41)$$

Once ε_b is assumed known, $\psi^{inc,b}(r)$ is calculated by solving (3.39). If the total field is measured at the receivers, then $\psi^{s,b}(r)$ is obtained at the receivers via (3.41). Essentially, the left-hand side of (3.41) is known at the receivers via measurement and solving (3.39) for $\psi^{inc,b}(r)$.

The goal of the inverse problem is to solve for $c(r)$ from which $\varepsilon(r)$, the cross sectional complex permittivity distribution of the 2-D dielectric scatterer, can be found. However, from (3.40), it is clear that this is a nonlinear inverse-scattering problem because $\psi(r)$ is also a functional of $c(r)$, as is clear from (3.38). But if $\varepsilon(r)$ is close to $\varepsilon_b(r)$, then $\psi^{s,b}(r) \ll \psi^{inc,b}(r)$ as is evident from (3.38).

Therefore $\psi(r)$ is approximated with $\psi^{inc,b}(r)$ in (3.40) and linearized equation is

$$\psi^{s,b}(r) = \int_{D_{obj}} dr' g_b(r,r') c(r') \psi^{inc,b}(r'), r \in D_M \qquad (3.42)$$

This approximation is called the Distorted Born approximation or the Distorted–wave Born approximation. If $c(r)$ is small, it can be easily shown that the error in this approximation is of order c^2 (i.e., second order) [17].

The linearized integral equation can be numerically solved to obtain $c(r)$, the cross sectional contrast of the scatterer with respect to the background. However, the profile thus obtained is not accurate because of the distorted Born approximation. This approximate $c(r)$ can be used to improve on the approximated object cross sectional profile $\varepsilon(r)$. Then $\varepsilon(r)$ can be used as the new $\varepsilon_b(r)$. With this new $\varepsilon_b(r)$, the $\psi^{s,b}(r)$, $\psi^{inc,b}(r)$ and $g_b(r,r')$ in (3.42) are recalculated and updated. Next, a new $c(r)$ is obtained and the process is repeated until convergence is attained. Since the error in (3.42) is of second order, this method has second-order convergence. This method of solving the inverse-scattering problem is called the distorted Born iterative method. It is to be noted that in the DBIM, the left side of equation (3.41) is updated in every iteration as $\psi^{inc,b}(r)$ is recalculated in each iteration step. Therefore $\psi^{s,b}(r)$ becomes smaller as $k_b^2(r)$ approaches $k^2(r)$ as the iteration step increases. If the measurement data is contaminated with noise, so that

$$\tilde{\psi}(r) = \psi(r) + n(r) \tag{3.43}$$

where $n(r)$ is the noise, then

$$\tilde{\psi}^{s,b}(r) = \psi(r) - \psi^{inc,b}(r) + n(r) \tag{3.44}$$

is the updated scattered field in each iteration step. Thus as the iteration step improves on $\psi^{inc,b}(r)$ so that it is closer to $\psi(r)$, $\tilde{\psi}^{s,b}(r)$ is swamped by the noise $n(r)$. Thus precautionary steps should be taken to prevent the iteration steps from diverging, when the scattered field data is corrupted by large measurement noise.

Thus the difference between DBIM and BIM is that in DBIM, the Greens function that propagates the field from a point in the object, r' to a point in the measurement domain r, is also updated at each step, in addition to the total field. The error estimate for the DBIM is of the second order, while that of the BIM is of the first order. So the DBIM will converge faster than BIM, and will converge to the global solution in cases where BIM does not.

The state and observation equations are discretized using pulse basis function and point matching method of moments. For a transmitter view v, the observation equation may also be written as,

$$[\psi^s_v] = [Gr_{v,om}][\psi_v][c], \tag{3.45}$$

where $[\psi_v]$ is an $N \times N$ diagonal matrix such that

66

$$\psi_v(i,i) = \psi_v(i), i = 1, 2, \ldots N.$$ (3.46)

Here $[\psi_v]$ and $[c]$ are lexicographically ordered vectors of dimension N. Collecting the measured scattered field from all the transmitter views, we can write

$$[\psi^s] = [P][c]$$ (3.47)

where $[P] = \begin{bmatrix} P_1 \\ P_2 \\ . \\ . \\ P_i \\ . \\ . \\ P_{M_t} \end{bmatrix}$ and $[P_i] = [Gr_{i,om}][\psi_i].$

$[P_i]$ is of dimension $N_r \times N$. If we denote the total number of measurement points in the measurement domain D_M as M, where $M = N_t N_r$, N_t being the number of transmitter antennas, $[P]$ is of dimension $M \times N$.

The solution of (3.47) for $[c]$ is not advised since the matrix $[P]$ is ill-conditioned and might not have a unique inverse. There are two main reasons for this ill-conditioning.

1. $[P]$ is an $M \times N$ matrix. It is possible for $M < N$,if the number of measurement data points is less than the number of pixels used to approximate the object function, then, the range space of $[P]$ would have a smaller dimension than the domain, implying that the inverse does not exist.

2.   The inverse problem is faced with fundamental scattering physics that contributes to its nonuniqueness. $[P]$ maps the object function $[c]$, to the measurement data, ψ^s. Many high spatial frequency components of $\varepsilon(r)$ are not mapped to ψ^s because these components generate evanescent waves that do not reach the receiver location. Therefore, these fine-grained details are lost in the inversion process.

A technique to overcome this problem is to use the method of regularization to solve the equation [18]. In this method, a functional is defined as

$$I = \left\| \psi^s - P.c \right\|^2 + \alpha \left\| c \right\|^2 . \qquad (3.48)$$

In the above expression, the first term is the error between the measurement data and that predicted by the linearized model. The second term is the norm of the contrast vector multiplied by a constant, α , the Tikhonov regularization parameter. An optimal solution for $c(r)$ is sought by minimizing the cost functional. The regularization procedure is employed since the electromagnetic inverse scattering problem is ill-posed in the Hadamard sense [19]. The Tikhonov regularization parameter is a tuning parameter, chosen to weigh the relative importance of the first term and the second term. In

this manner, the optimal solution will minimize the error between the measurement data and norm of $c(r)$. Because of this the values of $c(r)$ obtained will be bounded. If α is chosen too small, the numerical stability of the solution is compromised. However, if α is too large, useful information about the solution maybe filtered out. Therefore the regularization parameter should be carefully selected.

The cost functional maybe expanded as

$$I = ((\psi^s)^* - c^* P^*)(\psi^s - Pc) + \alpha c^* c \tag{3.49}$$

where * indicates the conjugated transpose. Taking the first variation of I with respect to the first variation in c and then setting it to zero, the following equation is obtained,

$$[P^* P + \alpha I]c = P^* \psi^s \tag{3.50}$$

where I is an Identity matrix of dimension $N \times N$. The contrast vector maybe thus be found out as

$$c = [P^* P + \alpha I]^{-1} P^* \psi^s. \tag{3.51}$$

The Newton Kantarovich (NK) Procedure is discussed next. The procedure allows for the easy insertion of a priori information that can be used to remove unrealistic solutions [20]. The NK and DBIM procedures have been shown to be computationally equivalent [8, 12, 17]. From the observation and state equations, considering small variations of the field, the equations become

$$[\Delta\psi_v^s] = [Gr_{v,om}][\Delta(C\psi_v)] \qquad (3.52)$$

and

$$[\Delta\psi_v] = [Gr_{oo}][\Delta(C\psi_v)] \qquad (3.53)$$

Expressing the quantity $\Delta(C\psi_v)$ as

$$\Delta(C\psi_v) = \Delta C\psi_v + C\Delta\psi_v \qquad (3.54)$$

Introducing (3.53) into (3.54), we get

$$\Delta(C\psi_v) = [I - CGr_{oo}]^{-1}[\psi_v][\Delta c] \qquad (3.55)$$

Since $[Gr_{oo}]$ is a symmetric matrix, we have

$$[I - CGr_{oo}]^{-1} = [[I - Gr_{oo}C]^{-1}]* \qquad (3.56)$$

This will simplify the calculations as $[I - Gr_{oo}C]^{-1}$ has already been calculated in the state equation. Substituting (3.55) in (3.52) and employing the equation (3.56), the variation of the scattered field in the measurement domain maybe expressed as

$$[\Delta\psi_v] = [Gr_{v,om}][[I - Gr_{oo}C]^{-1}]*[\psi_v][\Delta c] \qquad (3.57)$$

Collecting the quantity $[\Delta\psi_v]$ for every transmitter view, leads to the following relation,

$$[\Delta\psi^s] = [D][\Delta c] \qquad (3.58)$$

where

$$D = \begin{bmatrix} D_1 \\ D_2 \\ . \\ . \\ D_i \\ . \\ . \\ D_{Nt} \end{bmatrix},$$ (3.59)

and

$$[D_i] = [Gr_{i,om}][[I - Gr_{oo}C]^{-1}]*[\psi_i].$$ (3.60)

Here $[D_i]$ is of dimension $N_r \times N$ and $[D]$ of dimension $M \times N$ where $M = N_t N_r$. The above equation is solved iteratively for $[\Delta c]$ using the following relation,

$$\Delta c_k = [D*D + \alpha I]^{-1} D * \Delta \psi_k.$$ (3.61)

In the above equation, the Tikhonov regularization procedure is employed since the inverse scattering problem is ill-posed. By introducing this relationship into an iterative procedure (Here k indicates the iteration number), the initial non linear relation of the inverse scattering problem can be transformed into a sequence of linear ones. Hence, starting at an *a priori* initial contrast c_0, succession of intermediate c_k are generated by minimizing the difference between the computed scattered field according to the observation equation and the measured scattered field. The iterative process is summarized as follows,

1. Computation of the total internal field by inverting the state equation

2. Estimation of the scattered field at the receiver locations

3. Computation of the error between the scattered field computed in step 2 and the measured scattered field, $\Delta \psi_k$

4. Estimation of the error in contrast c_k by solving (3.61).

5. Updating the contrast function $c_{k-1} = c_k + \Delta c_k$

6. Go to step 1 as long as $\Delta \psi_k$ is larger than an acceptable error.

The linearized matrix equations maybe solved for the object contrast (in the case of Newton Kantorovich procedure, the update to the object contrast) using Singular Value Decomposition Technique [21]. As example, consider equation (3.47). Here the matrix $[P*P]$ is ill conditioned because of the multiple scattering. Since $[P*P]$ is Hermitian [2], we can decompose it as

$$[P*P] = S.\lambda.S' \qquad (3.62)$$

where S is a unitary matrix (i.e. $S' = S^{-1}$) and λ is a diagonal matrix containing the eigen values of $[P*P]$. However because of the ill-conditioning of $[P*P]$, it has eigen values too small or zero.

Therefore in

$$[P*P]^{-1} = S.\lambda^{-1}.S' , \qquad (3.63)$$

λ^{-1} is unbounded. When a regularization procedure is employed, instead of seeking the inverse of $[P*P]$, the inverse of $[P*P+\alpha I]$ is sought. The Tikhonov Regularization parameter therefore will pad the zero eigen values of $[P*P]$ with a non-zero value. It is to be noted that numerical instability of the inverse process is related to the large condition number of $[P*P]$. To decrease the condition number, it is necessary to filter out the high frequency components which are affected by the measurement noise, via the regularization procedure. On the other hand, a strong regularization process may remove useful components and decrease the spatial resolution because of the low pass filtering effect. As a consequence, the regularization factor is to be fixed in order to accommodate a convenient spatial resolution-stability compromise. In this work, an empirical formula for the regularization parameter is employed [8]

$$\alpha = \beta \frac{Trace[P*P]}{N} \frac{\|F(c_k)-\psi_s\|^2}{\|\psi_s\|^2}. \tag{3.64}$$

Here $F(c_k)$ is the computed scattered field with the current estimate of the contrast c_k. $\dfrac{\|F(c_k)-\psi_s\|^2}{\|\psi_s\|^2}$ is the normalized relative residual error $Err(\psi^s)$ and β is a constant that is determined empirically. The value of β is initially chosen and is updated in each iteration according to

$$\beta_+ = \begin{cases} \beta_c, if\ Err(\psi^s{}_c)-Err(\psi^s{}_-) < -0.1Err(\psi^s{}_c) \\ \dfrac{1}{2}\beta_c, if -0.1Err(\psi^s{}_c) \le Err(\psi^s{}_c)-Err(\psi^s{}_-) \le 0.1Err(\psi^s{}_c) \\ 2\beta_c, if\ Err(\psi^s{}_c)-Err(\psi^s{}_-) > 0.1Err(\psi^s{}_c) \end{cases}. \tag{3.65}$$

In the above expression, β_+ is the next update and β_c is the current value. $Err(\psi^s_c)$ and $Err(\psi^s_-)$ are the current and previous normalized residuals respectively. The constraint is thus weakened when the process converges too slowly or when the error increases slightly, which will aid the process to escape from getting trapped in a local minimum. Even so, an iterative deterministic procedure may fail to reach a convergent solution because of the non linearity and ill posed-ness of the inverse scattering problem. The ill-posedness is even more severe when scattered field measurements are possible only from a limited number of transmitter views, as in the case of imaging of buried objects.

References

1. Fredholm, I. *"Su rune classe d'equations fonctionalles"* Acta Math. 27: 365-390, 1903).

2. Chew W.C, *Waves and fields in inhomogeneous media*, New York, IEEE Press, 1995.

3. Umashankar K., Taflove A., *Computational Electromagnetics*, Norwood, Artech House Inc., 1993

4. Slaney M, Azimi M, Kak A.C, Larsen L E, "Microwave imaging with first order diffraction tomography", *Medical applications of microwave imaging*, pp 184-211, IEEE Press New York, 1986)

5. Born, M. and E. Wolf. 1980. *Principles of Optics.* 6th edition. New York: Pergamon Press. First edition 1959.

6. Booton Richard C. Junior, *Computational methods for Electromagnetics and Microwaves,* Wiley Interscience, New York, 1992.

7. Richmond, J. H, "Scattering by a dielectric cylinder of arbitrary cross section shape", *IEEE Transactions on Antennas and Propagation*, Vol. AP-13, pp 334-341, 1965.

8. Franchois A. and C. Pichot, "Microwave Imaging-complex permittivity reconstruction with a Levenberg-Marquardt Method", *IEEE Transactions on Antennas and Propagation*, Vol. 45, no.2, pp 203-215, February 1997.

9. Cui, T. J., W. C. Chew, A. A. Aydiner and S. Chen, "Inverse Scattering of Two- Dimensional Dielectric objects buried in Lossy Earth using the Distorted Born Iterative Method", *IEEE Transactions on Geoscience and Remote Sensing*, Vol. 39, No.2, pp 339-346, February 2001

10. Cui, T. J., Y. Qin, G. L. Wang and W. C. Chew, " Low Frequency detection of two-dimensional buried objects using high-order extended Born approximation", *Inverse Problems*, 20, S41-S62, 2004.

11. Baussard. A, E. L. Miller, D. Lesselier, "Adaptive Multiscale Reconstruction of Buried Objects", *Inverse Problems*, 20, S1-S15, 2004.

12. Tijhuis, A. G., K. Belkebir, A. C. S. Litman and B. P. de Hon, " Theoretical and Computational Aspects of 2-D Inverse Profiling", *IEEE Transactions on Geoscience and Remote Sensing*, Vol. 39, No. 6, pp 1316-1329,June 2001.

13. Belkebir, K., R. E. Kleinman and C. Pichot, " Microwave Imaging- Location and Shape reconstruction from Multifrequency Scattering Data", *IEEE Transactions on Microwave Theory and Techniques*, Vol. 45, No. 4, pp 469-476, April 1997.

14. Chew, W.C. and J. H. Lin, "A Frequency Hopping Approach for Microwave Imaging of Large Inhomogeneous Bodies", IEEE Microwave and Guided Wave Letters, Vol. 5, No. 12, pp 439-441, December 1995.

15. Wang, Y. M. and W. C. Chew, "An iterative solution of two-dimensional electromagnetic inverse scattering problem", *International Journal of Imaging Systems Technology*, Vol. 1, No. 1, pp 100-108, 1989.

16. Chew, W. C. and Y. M. Wang, "Reconstruction of Two-Dimensional Permittivity Distribution Using the Distorted Born Iterative Method", *IEEE Transactions on Medical Imaging*, Vol. 9, No. 2, pp 218-225, June 1990.

17. Teflove, A., *Advances in Compuational Electrodynamics*, Boston, London, Artech House, 1998.

18. Tikhonov, A. N. and V. Y. Arsenin, *Solution of ill-posed problems*, Washington D. C., V. H. Winston and Sons, 1977.

19. Hadamard, J., *Lectures on Cauchy's problem in linear partial differential equations,* New Haven, C.T, Yale University Press, 1923.

20. Joachimowitz, N., C. Pichot and J. P. Hugonin, "Inverse Scattering: An Iterative Numerical Method for Electromagnetic Imaging", IEEE Transactions on Antennas and Propagation, Vol. 39, No. 12, pp 1742-1751, December 1991.

21. Press, W. H., S. A. Teukolsky, W. T. Vellering and B. P. Flannery, *Numerical Recipes in C*, Cambridge University Press, 1992.

CHAPTER 4

Multi-scaled frequency hopping

4.1 Introduction

A large class of image processing problems such as deblurring, high resolution rendering, image recovery, image segmentation, motion analysis and tomography require the solution of inverse problems. Often, the numerical solution to inverse problems is beset with several computational issues, particularly when the problem is highly non-linear as in the case of Microwave/RF imaging. The non-linearity and ill-posedness of the inverse scattering problem of microwave imaging is attributed to multiple scattering, which increases with object size and contrast [1]. The algorithms employed for this inverse scattering problem maybe broadly classified into deterministic or stochastic. All of them tackle the nonexistence of the inverse scattering problem by redefining it as the minimization of a cost functional [2-5]. However, due to the nonlinearity of the inverse scattering problem, there is a risk that the solution gets trapped in a local minimum. The stochastic methods [2] [6, 7], though globally convergent, are extremely computation intensive, especially when the number of unknowns is high. One way to minimize the risk of local minima is to use prior knowledge about the scatterer, so that the nonlinear problem is linearized about a different background [8]. However such prior knowledge is not always available. A technique that has been suggested to improve the convergence of

this inverse scattering problem is to collect multi-frequency data instead of monochromatic data for the inversion [9-13]. The inverse problem is solved at a lower frequency where it is more linear and thus less prone to local minima, and this solution is used as an initial estimate for inversion at a higher frequency. The final solution will be much less prone to local minima than in the monochromatic case of the highest frequency alone. The convergence of the solution at the higher frequencies is determined by the initial estimate provided by the iterations at the low frequencies.

To solve the inverse scattering problem of electromagnetic imaging, most algorithms work by performing all computations using a fixed discretization grid. While progress has been made in reducing the computational complexity of the fixed grid methods [14-18], computational cost is still a big concern. More importantly fixed grid methods employ optimization techniques that perform a local search of the cost function, and are therefore more susceptible to being trapped in local minima that can result in poorer quality reconstructions.

Multi resolution techniques have been widely investigated to reduce computational burden of inverse problems and to ensure their converging globally. Simple multi resolution approaches such as initializing fine resolution iterations with coarse resolution have been shown to be effective in many imaging problems [19-23]. Multi resolution methods have been employed in the inverse scattering problem of microwave imaging, which considerably reduces the risk of the trial solution getting trapped in a local minimum with respect to the deterministic algorithm employed [24, 25]. However, since the solution to the inverse electromagnetic scattering problem is found by minimizing

a cost functional, it is possible that local minima may again be reintroduced, even though the solution is less likely to be trapped there compared to fixed grid methods.

The approach employed in this work is to combine frequency hopping with a multi-scale method. At each frequency hop, the inverse problem is solved at a coarse resolution. This solution is used as an initial estimate for the next finer scale and so on until the inverse problem is solved at the finest scale for the frequency employed. The final solution for this frequency is used as the initial estimate for the next higher frequency hop. The process is repeated until the solution is found for the finest scale in the highest frequency employed. The method employed for inverse profiling is the Newton Kantorovich algorithm [5,8], but the strategy is independent of the deterministic optimization method employed. The strategy has been tested on synthetic data and the Marseille experimental data [26] and the results are promising.

4.2 Problem statement and solution

A cylindrical object of arbitrary cross section surrounded by a homogenous exterior medium of known complex permittivity $\in_{ext}$, under TM harmonic excitation is located in a rectangular imaging domain I. Usually water or saline solution has been employed as the medium for microwave medical imaging for enhancing the coupling of electromagnetic energy. Recently, sodium meta silicate gel, which is significantly less lossy than water or saline in the ISM band, has been proposed as a suitable coupling medium for microwave medical imaging [27]. A cylindrical geometry for the imaging system is

employed, with M line sources equispaced on a circle in the measurement domain. At a time one of the antennas will be emitting and the others will be receiving. The scattered field is measured for different views. A time convention of $e^{j\omega t}$ is employed. The integral equations for modeling the forward and inverse scattering are reproduced here.

$$\psi(r)=\psi^{inc}(r)+ {}_{D_{obj}}\!\!\int dr'g(r,r')c(r')\psi(r'), r \in D_{obj} \qquad (4.1)$$

$$\psi^{s}(r)= {}_{D_{obj}}\!\!\int dr'g(r,r')c(r')\psi(r'), r \in D_{M} \qquad (4.2)$$

Nonexistence of the inverse solution is coped by redefining the solution as a minimizer of the least square error with respect to data. In practice, one looks for a spatially discretized vector $c(r)$, the lexicographically ordered representation of the two dimensional image contrast. This alleviates non uniqueness to a good extent. Thus it is evident that the stability of the solution will be better when the discretization cell size is not too small [8]. Hence, non uniqueness is less prominent at a coarse resolution. However, the use of a cost functional may again introduce local minima. The integral equations are discretized using the Richmond's procedure [28]. The imaging region is discretized into N cells of dimension corresponding to the particular scale. The coupled equations (4.1) and (4.2) are solved for the current estimate of c. A regularization procedure is employed since the matrix employed in the inversion is ill conditioned [29.] An empirical formula for the regularization parameter has been employed [5,8] as per equation (3.65). The inverse problem is first solved at a coarse spatial sampling

rate where it is more stable. This solution is chosen as the initial estimate for solving the problem at progressively finer sampling rates. The final convergent solution is used as the initial estimate for the next frequency hop. The process is continued until a convergent solution is found for the highest frequency hop. The entire procedure employed is illustrated in the following flow chart.
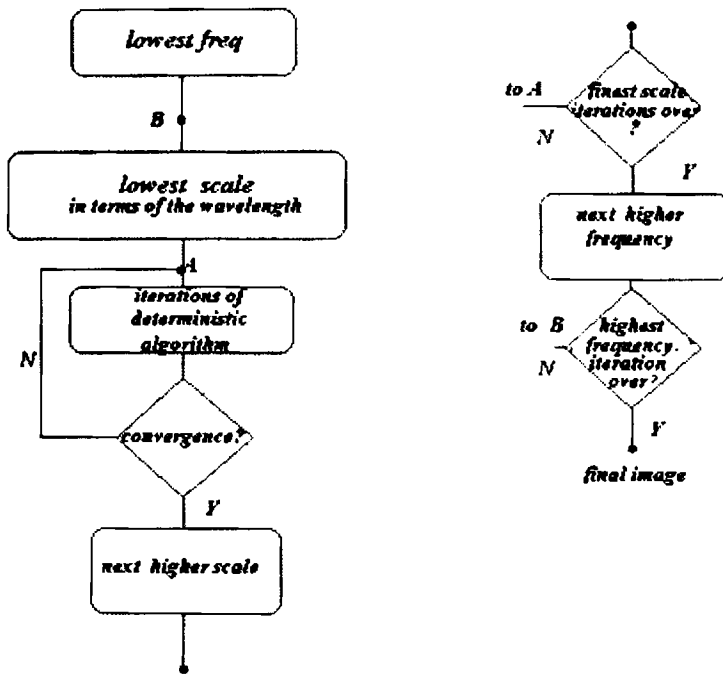
Figure 4.1
Flow chart illustrating the multiscale frequency
hopping strategy

4.3 Results and Discussion

The strategy was tested on synthetic data as well as experimental data provided by the Centre Commun de Ressourses Micro-ondes (CCRM) of Marseille France. The coupled equations (4.1) and (4.2) were used to generate synthetic broadband data for the inversion. The following frequencies have been employed for the incident field: 1GHz, 2GHz and 4GHz. The problem is solved at a coarse resolution of $\frac{\lambda}{5}$ at 1 GHz and then at finer resolutions of $\frac{\lambda}{10}$ and $\frac{\lambda}{20}$ as per the multiscale optimization scheme. Thereafter, it is solved at resolutions $\frac{\lambda}{10}$ and $\frac{\lambda}{20}$ at 2GHz and 4GHz. For frequency hopping without multiscaling, the inverse scattering problem is solved at the highest resolution of $\frac{\lambda}{20}$ at every frequency. In the frequency hopping technique, the solution from the lower frequency measurements is used as the initial estimate for solving the problem at a higher frequency. The stability of the solution is better when the discretization of the inverse scattering problem is coarse. This when employed as the initial estimate for solving the problem at a smaller discretization cell size, will give a more stable solution. Thus the multiscaling approach reduces the risk of the solution from the lower frequency measurements getting trapped in a local minimum, with respect to the deterministic optimization method employed.

At each stage, the iterations are stopped when the residual, the error between measured and computed scattered fields, is below a predetermined tolerance level of 2×10^{-2}. The proposed scheme shows

an improvement over frequency hopping for some of the test object configurations, as illustrated in the examples in figures.

In the first example the results of the strategy when tested on the CCRM experimental data are shown. Here the scatterer configuration consists of two dielectric cylinders of diameter 3 cm spaced apart by 9 cm. The scatterer is illuminated by TM polarized EM wave. For the reconstructions, the scattered field values at 1, 2 and 4 GHz were considered. The incident field is modelled by an infinite line source. The set of images in figure 1 shows the results obtained by employing frequency hopping alone. The iterations at each step are terminated when the normalized residual error $Err(\psi^s)$ reduces below 2×10^{-2}. The results in figure 2 show the reconstructions when the proposed multiscale frequency hopping strategy was employed. Comparing the final convergent images in figure 1 and figure 2, it is observed that the two dielectric scatterers are better localized with the proposed strategy. It is also seen that the number of computational steps required for the normalized residual to decrease below the set value is lesser. The final convergent image was obtained after 20 iterations of the Newton Kantarovich procedure at 1GHz where the imaging region is discretized into a 32 x 32 grid, 10 iterations at 2 GHz where the imaging region is discretized into a 64 x 64 grid and 8 iterations at 4 GHz where the imaging region is discretized into a 128 x 128 grid. For the multiscaled frequency hopping strategy, for the frequency 1 GHz, the number of iterations at $\dfrac{\lambda}{5}$ is 18, those at $\dfrac{\lambda}{10}$ is 16 and at $\dfrac{\lambda}{10}$ the number of iterations is 16. At 2 GHz, the number of iterations at $\dfrac{\lambda}{10}$ is 10 and at $\dfrac{\lambda}{20}$ the number of iterations is 9. Likewise

at 4 GHz, the Newton Kantarovich procedure converges in 6 iterations

at $\frac{\lambda}{10}$ and in 6 iterations at $\frac{\lambda}{20}$. The number of computations per

iteration is of the order of N^3 when the Singular Value Decomposition

procedure is adopted to solve the Matrix formulations for equations

4.1 and 4.2. For the frequency hopping scheme, at 1 GHz, the order of

computations is $O(20 \times (32 \times 32)^3) = O(2.147e10)$, whereas for the

proposed strategy, this is

$O(18 \times (8 \times 8)^3 + 16 \times (16 \times 16)^3 + 16 \times (32 \times 32)^3) = O(1.7453e10)$. The

corresponding values at 2 GHz are $O(6.8719e11)$ and

$O(6.2814e11)$ respectively. Similarly the corresponding values at 4

GHz are $O(3.5184e13)$ and $O(2.6801e13)$ respectively. Comparing

the above values, it is observed that the computations are reduced at

every frequency hop with the proposed strategy.

The synthetic data for inversion were generated by using the

same configuration for the imaging setup as were employed for the

CCRM experimental data. The figure 3 shows a much stronger

scatterer than in the previous example, which resembles the human

arm [27]. It is observed that the reconstructions with the proposed

strategy are better than the frequency hopping scheme in

reconstructing the features of the scatterer, as shown by final

convergent images in the figures 4 and 5. The cylinders are better

localized in the MSFH scheme compared to the frequency hopping

scheme. This is because the multiscaling strategy at the lower

frequencies succeeded in providing a better initial estimate for the

iterations at the higher frequencies for this object, than when the

solution was computed at the finest scales alone.
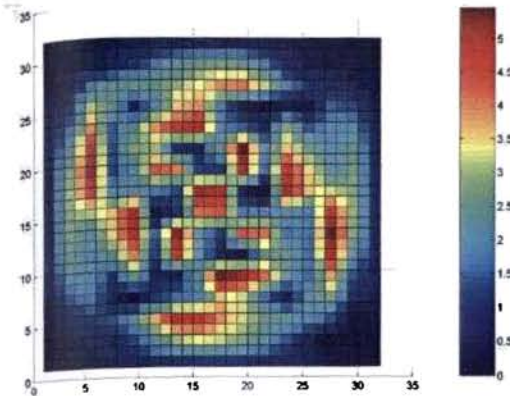
Figure 1.a
The reconstruction after the first Newton Kantarovich iteration at 1 GHz
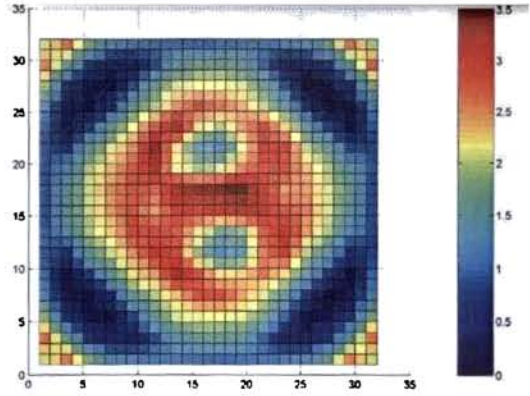
Figure 1.b
The final convergent image with the Newton Kantarovich iteration at 1 GHz
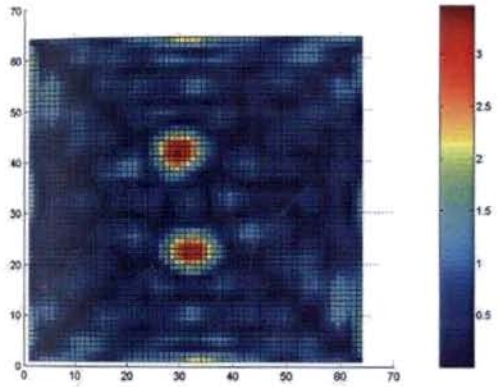
Figure 1.c
The reconstruction after the third Newton Kantarovich iteration at 2 GHz
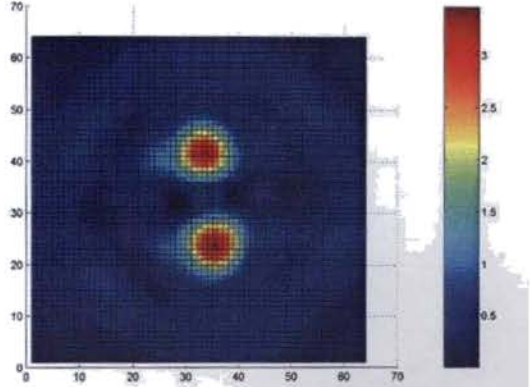
Figure 1.d
The final convergent image with the Newton Kantarovich iteration at 2 GHz
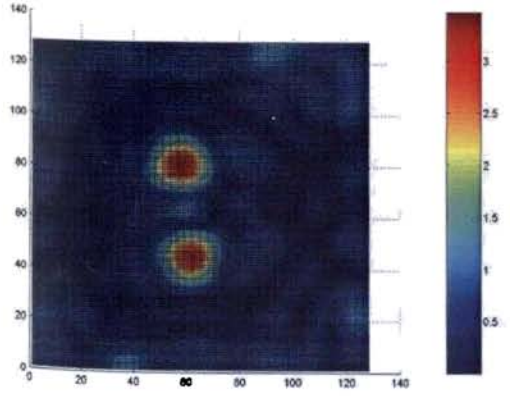
Figure 1.e
The reconstruction after the fourth Newton Kantarovich iteration at 4 GHz
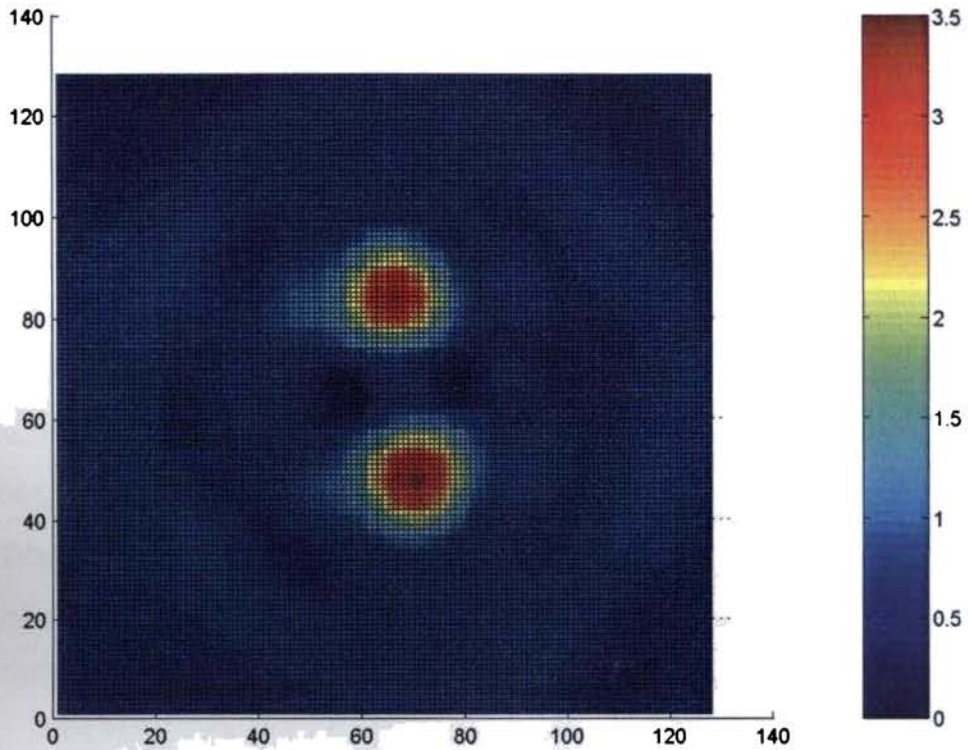
Figure 1.e
The final convergent image at the eight
iteration of the Newton Kantarovich
procedure at 4 GHz
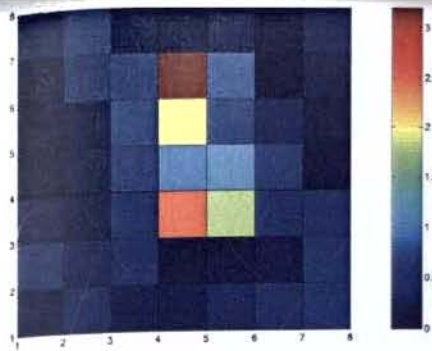
Figure 2.a

The final convergent image at $\frac{\lambda}{5}$ at the 18th NK iteration at 1 GHz
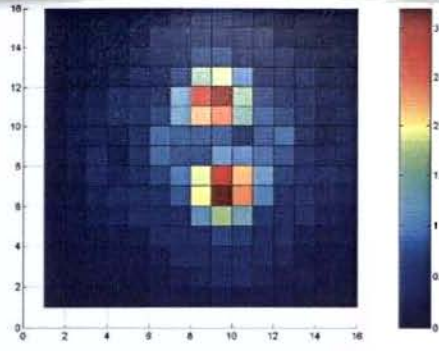
Figure 2.b

The final convergent image at $\frac{\lambda}{10}$ at the 16th NK iteration at 1 GHz
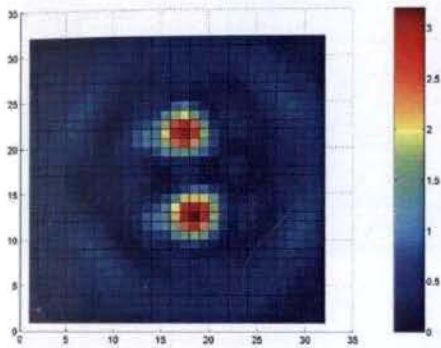
Figure 2.c

The final convergent image at $\frac{\lambda}{20}$ at the 16th NK iteration at 1 GHz
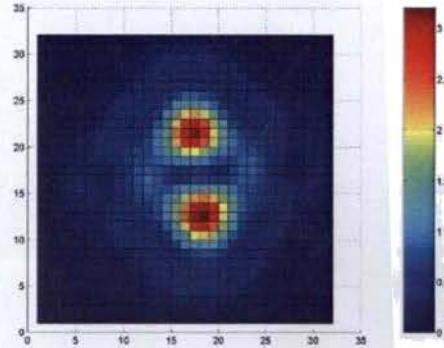
Figure 2.d

The final convergent image at $\frac{\lambda}{10}$ at the 10th NK iteration at 2 GHz
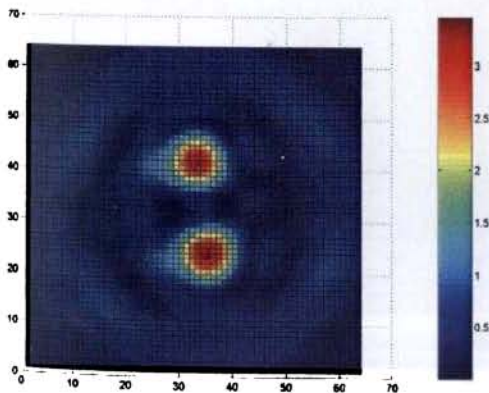
Figure 2.e

The final convergent image at $\frac{\lambda}{20}$ at the 9th
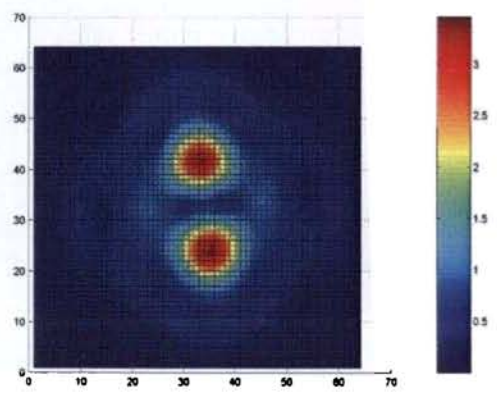
Figure 2.f

The final convergent image at $\frac{\lambda}{10}$ at the 6th
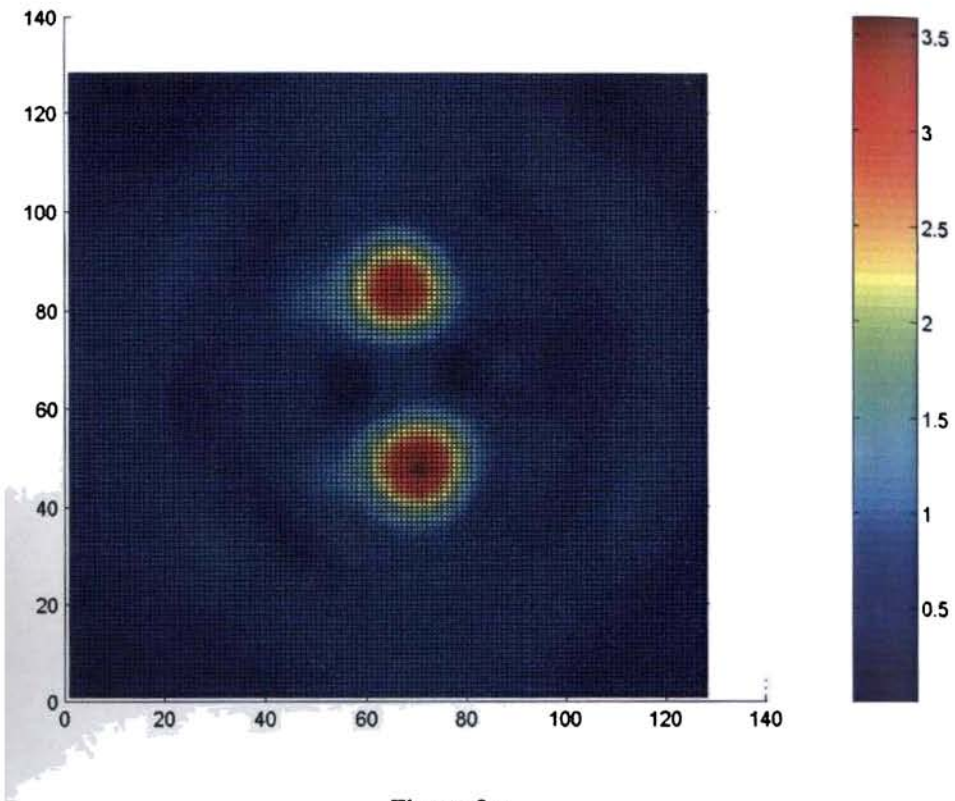
Figure 2.g

The final convergent image at $\dfrac{\lambda}{20}$ at the 6th NK iteration at 4 GHz. The total number of computations has been reduced for the relative error to reduce below the specified tolerance. The reconstructed image is found to be slightly better with the proposed scheme, compared to figure 1.e.
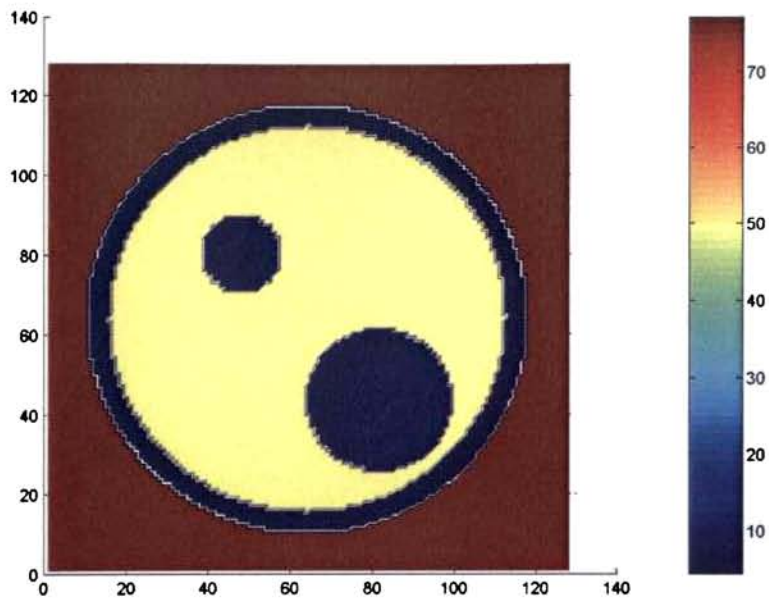
Figure 3.a
Real part of the complex permittivity profile of the hand like scatterer
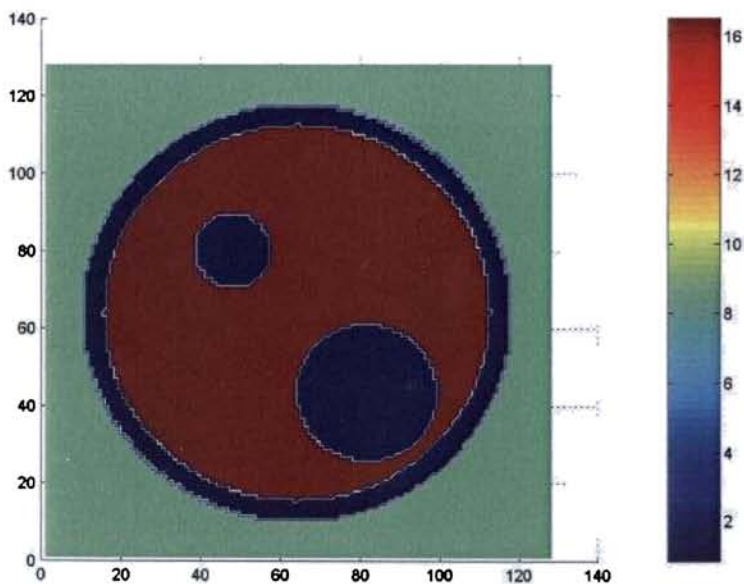
Figure 3.b
Imaginary part of the complex permittivity profile of the hand like scatterer
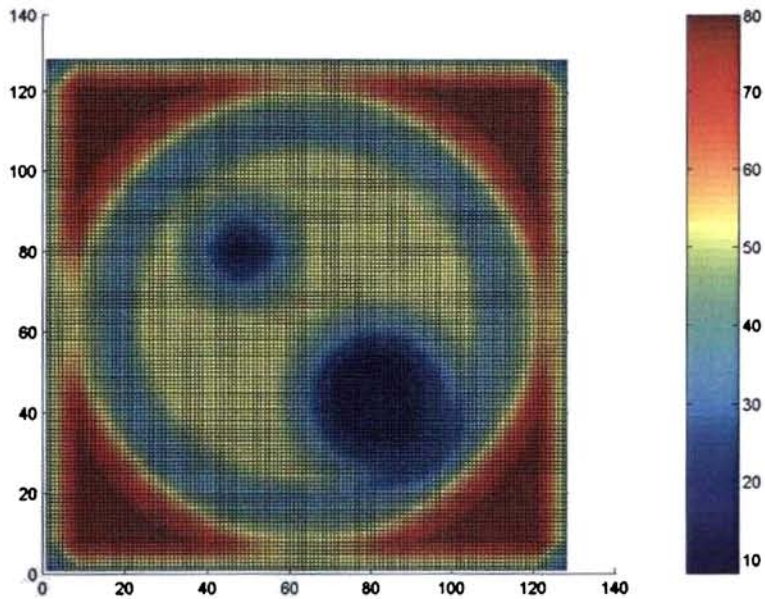
Figure 4.a
Reconstructed real part of the complex permittivity profile of the scatterer using the frequency hopping scheme at the highest scale
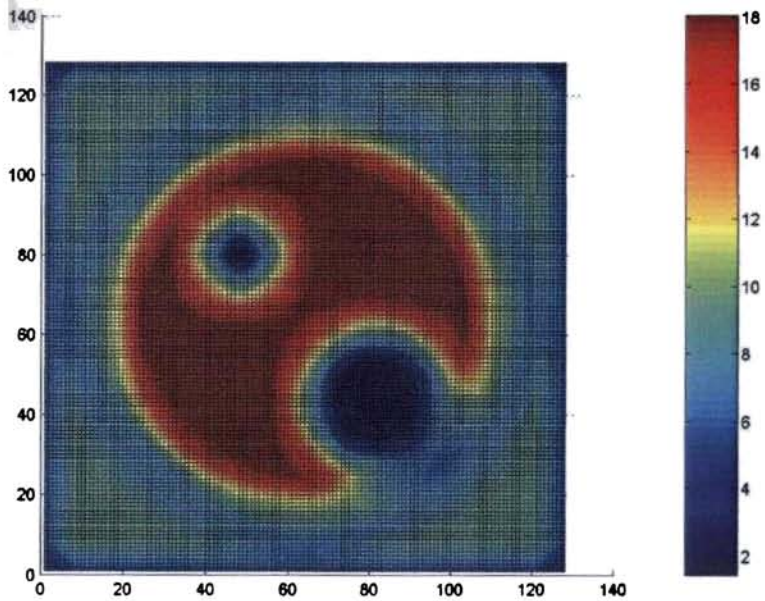
Figure 4.b
Reconstructed imaginary part of the complex permittivity profile of the scatterer using the frequency hopping scheme at the highest scale
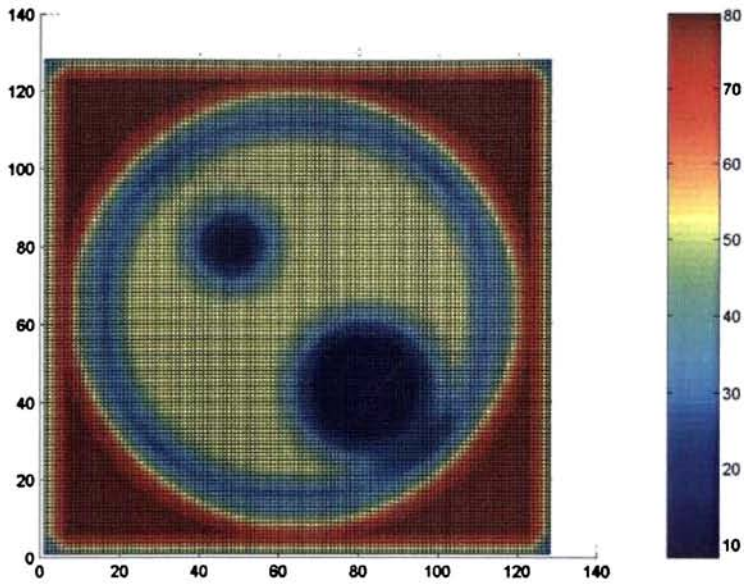
Figure 5.a
Reconstructed real part of the complex permittivity profile of the scatterer using the proposed scheme. The features of the scatterer are better reconstructed compared to figure 4.a
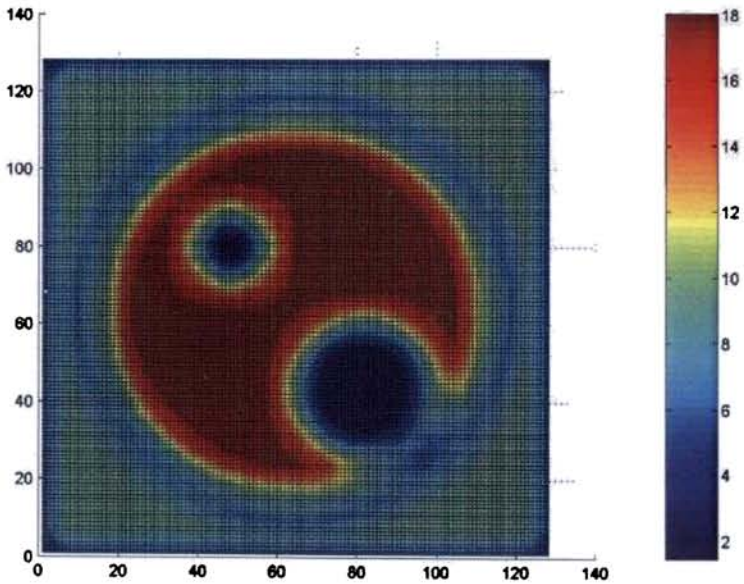
Figure 5.b
Reconstructed imaginary part of the complex permittivity profile of the scatterer using the proposed scheme. The features of the scatterer are better reconstructed compared to figure 4.b. The reconstruction artifacts have also been

eierences

1. Bolomey, J.C. and C. Pichot, "Microwave tomography, from theory to practical imaging systems", *International Journal of Imaging systems Technology*, Vol.2, 1990, pp144-156.

2. Garnero, L., A. Franchois, J. P. Hugonin, C. Pichot and N. Joachimowicz, "Microwave Imaging, Complex permittivity reconstruction by simulated annealing", *IEEE Trans. Microwave Theory Tech.*, Vol. 39, pp 1801 – 1807, Nov. 1991.

3. Moghaddam, M. and W.C. Chew, "Non linear two-dimensional velocity profile inversion in the time domain", *IEEE Transcations on Geoscience and Remote Sensing*, Vol. GE-30, 1992, pp 147-156

4. Chew, W.C., and Y. M. Wang, "Reconstruction of two-dimensional permittivity distribution using the distorted Born iterative method", *IEEE Trans. Med. Imag.*, vol. 9, pp 218 – 225, June1990.

5. Joachimowicz, N., C. Pichot and J. P. Hugonin, "Inverse Scattering: An Iterative Numerical Method for Electromagnetic Imaging", *IEEE Trans. Antennas Propagat.*, vol. 39, no. 12, pp 1742 – 1751, Dec. 1991

6. Pastorina, M., A. Massa and S. Caorsi, "A Microwave inverse scattering technique for image reconstruction based on a genetic algorithm", *IEEE Trans. Meas. Instrum.*, Vol. 49, pp 573 – 578, June 2000.

7. Chen, X., D. Liang and J. Huang, "Microwave imaging 3-D buried objects using parallel genetic algorithm combined with FDTD technique", *Journal of Electromagnetic waves and applications,* Vol. 20, No. 13, December 2006

8. Franchois, A. and C. Pichot, "Microwave Imaging – Complex permittivity reconstruction with a Levenberg – Marquardt method", *IEEE Trans. Antennas Propagat.*, vol. 45, no. 2, pp 203 – 215, Feb. 1997.

9. Chew, W.C. and J. C. Lin, "A Frequency Hopping approach for microwave imaging of large inhomogeneous bodies", *IEEE Microwave and Guided wave letters*, vol. 5, no.12, pp 439 – 441, Dec 1995.

10. Belkebir, K., R. E. Kleinman and C. Pichot, "Microwave imaging – Location and Shape Reconstruction from Multifrequency Scattering Data", *IEEE Trans. Microwave Theory Tech.*, vol. 45, no.4, pp 469 - 475, April 1997.

11. Crocco, L., "Inverse scattering with real data: detecting and imaging homogeneous dielectric objects", *Inverse Problems*, 17, 1573-1583, 2001.

12. Semenchik, V., V. Pahomov and S. Kurilo, "Multifrequency Microwave Imaging", *Proceedings of the Fifth International Kharkov Symposium on Physica and Engineering of Microwaves, Millimeter and Sub-millimeter waves*, Vol. 1, pp 193-195, 2004.

13. Kim, J. H. and Ra, Jung-Woong, "Multifrequency microwave imaging of a lossy dielectric cylinder in a lossy medium", *Microwave and Optical technology letters*, Vol. 10, issue 1, pp 26-31, 1995.

14. Lin, J. H. and W.C. Chew, "Three dimensional microwave imaging with local shape function method with CGFFT", *IEEE Antennas and Symposium AP-S Digest*, Vol. 3, Issue 21-26, pp 2148-2151, July 1996.

15. Lu, C.C. and X.G. Zhong., "Image reconstruction of two dimensional objects inside dielectric walls", *Microwave and Optical technology letters*, Vol. 36, Issue 2, Pages 91-95, December 2002.

16. Abubakar, A. and P. M van den Berg, "The contrast inversion method for location and shape reconstruction", *Inverse Problems*, Vol. 18, pp 495-510, 2002.

17. Mia, J., W. C. Chew, C.C. Lu, and J. Song, "Image reconstruction from TE scattering data using equation of strong permittivity fluctuation" , *IEEE Transactions on Antennas and Propagation*, Vol. 48, Issue 6, pp 860-867, June 2000.

18. Harada H., M. Tanaka and T. Tanaka, "Image reconstruction of a three dimensional object using gradient based optimization", *Microwave and Optical technology letters*, Vol. 31, No.6, pp 332-336, December 2001

19. Ranganath, M.V., A. P. Dhavan and N. Mullani, "A Multigrid expectation maximisation algorithm for positron emission tomography", *IEEE Transactions on Medical Imaging*, Vol. 7, No.4, pp 273-278, Dec 1988.

20. Pan. T. and A. E. Yagle, "Numerical study of multigrid implementations of some iterative image reconstruction algorithms", *IEEE Transactions on Medical Imaging*, Vol. 10, No.4, pp 572-588, Dec 1991.

21. Milstein, A.B., S. Oh, J. S. Reynolds, K .J. Webb, C. A. Bouman and R. P. Millane, "Three dimensional optical diffusion tomography using experimental data", *Optical letters*, Vol. 27, pp 95-97, January 2002.

22. Oh, S., A.B Milstein, R. P. Millane, C. A. Bouman and K .J. Webb, "Source detector calibration in three dimensional

Bayesian optical diffusion tomography", *Journal of Optical Society America*, Vol.19, no.10, pp 1983-1993, October 2002.

23. Sauer, K. and C. A. Bouman, "A local update strategy for iterative reconstruction from projections", *IEEE Transactions on Signal Processing*, Vol. 41, no. 2, pp 534-548, February 1993.

24. Tanaka, M., K. Yano, H. Yoshida and A. Kusunoki, "Multigrid optimization method applied to electromagnetic inverse scatteing problem", *IEICE Transactions on Electronics*, E90-C(2), pp 320-326, 2007.

25. Caorsi, S., M. Donelli, D. Franceschini and A. Massa, A New methodology based on an Iterative Multiscaling for Microwave Imaging, IEEE Trans. Microwave Theory Tech., vol. 51, no. 4, April 2003.

26. Belkebir, K. and M. Saillard, "Special section: Testing inversion algorithms against experimental data", Inverse Problems Vol.17, pp1565–1571, 2001.

27. V. Hamsakutty, A. Lonappan, V. Thomas, G. Bindu, J. Jacob, J. Yohannan and K. T. Mathew, Coupling medium for microwave medical imaging applications, IEE Electronic Letters, vol. 39, no. 21, Oct. 2003.

28. J. H. Richmond, Scattering by a dielectric cylinder of Arbitrary Cross Section Shape, IEEE Trans. Antennas Propagat., vol. AP -13, pp 334 – 341, May 1965.

29. A. N. Tikhonov and V. Y. Arsenine, Solutions of Ill Posed Problems, Washington, DC: Winston, 1977

Degree of Symmetry Formulation

5.1 Introduction

Several methods, both stochastic and deterministic have been developed to solve the inverse scattering problem of electromagnetic imaging. Typically, all these methods solve a large-scale, non-linear optimization problem by generating values for every pixel covering the investigation domain. The electromagnetic inverse scattering problem is ill posed in the Hadamard sense and is also highly non linear. Due to its non linearity, there are multiple solutions to the inverse scattering problem and therefore the solutions are liable to get trapped in local minima[1].

The investigation domain has to be chosen sufficiently large to include all possible locations of the scatterer whose cross sectional profile is to be inverted from the measured scattered field data [2 - 4]. When the investigation domain is large, the number of unknowns of the inverse scattering problem increases and an iterative procedure for solving the inverse problem may fail to reach a convergent solution and could get stuck in a local minimum, in addition to increasing the computation time. The algorithms employed for the electromagnetic inverse scattering problem generate values also for those regions in the investigation domain that might not contain any useful information about the object [4]. Therefore if a localization of the object could be done in the investigation domain prior to the inverse scattering, the

available information about the scatterer known via the measured scattered field can now be employed for the optimization of fewer numbers of cells in the investigation domain, which will help in the global convergence of the solution

For a 2-D Dielectric scatterer of circular cross section, with the complex permittivity distribution symmetric with respect to the centre of the cross section, a custom defined Degree of Symmetry formulation is employed here to localize the scatterer in the investigation domain, prior to the inverse scattering. This a priori information about the scatterer is valid for structures such as dielectric posts and pipe lines. The degree of symmetry computed for each transmitter position is a measure of the symmetry of the scattered field vector in the measurement domain for each transmitter view. The degrees of symmetries thus computed for a scatterer together forms a Degree of Symmetry vector.

It is seen that the Degree of Symmetry vectors exhibit unique features for the geometric properties of the scatterer. This makes it possible to localize the object in the investigation domain. This will reduce the number of unknowns of the inverse scattering problem, thereby aiding the global convergence of the solution.

The Degree of Symmetry formulation was also applied to the practical case of limited angle tomography, when scattered field measurements around the object are not possible, as in the case of buried objects. The development of imaging techniques for investigation of physically inaccessible objects is of much importance

in areas such as oil exploration, seismic imaging, non destructive evaluation, buried object detection etc. In most of these cases, reliable information about the physical properties of the inaccessible target is desired in addition to detection of the target. All these problems may be classified as electromagnetic inverse problems when the characterization of the unknown target is computed by considering electromagnetic illumination and employing the values of the scattered electromagnetic field. The ill posedness of the inverse scattering problem is more severe here, due to the availability of only aspect limited data. Two dimensional models have been employed to model electromagnetic scattering from buried dielectric pipelines [4-8]. When TM polarization of the EM wave is employed to illuminate the scatterer, the scattering problem reduces to a scalar one [9]. The reduction in the investigation domain reduces the degrees of freedom of the inverse scattering problem. This improves the convergence of the solution and also results in a reduction in computation time of the inverse scattering methodology employed.

5.2 Formulation of the Problem

The problem is formulated first when the scatterer and the measurement setup lies in the same background medium. When measurements of the scattered field maybe done around the object, a circular geometry is assumed for the measurement setup in the simulations as shown in figure 5.1.
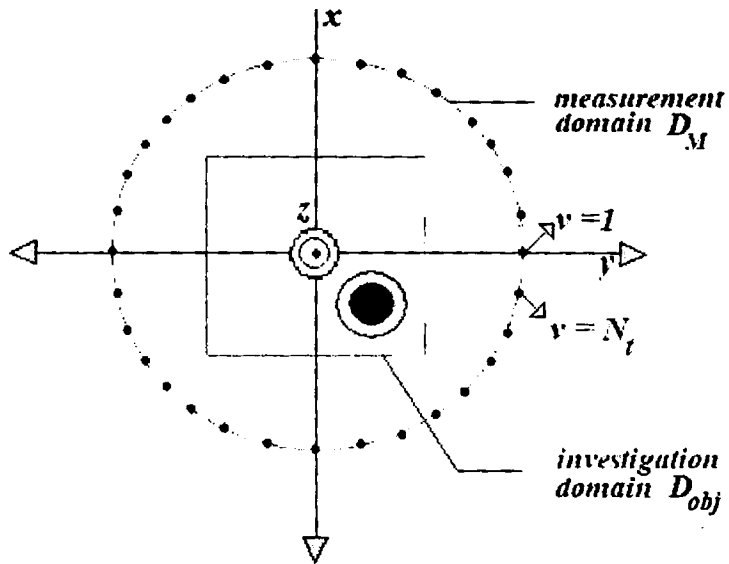
Figure 5.1
Measurement setup for electromagnetic inverse scattering experiment
Circular geometry is employed for the setup

A 2-D dielectric scatterer of circular cross section and complex permittivity distribution symmetric with respect to the centre of the cross section is located in an investigation domain D_{obj}, which is usually a square or a rectangle. The maximum diameter possible for the unknown circular object to be imaged is also assumed to be known. This a priori is valid for structures such as dielectric posts and pipe lines. However, since the location of the object to be imaged is not known, the investigation region has to be chosen sufficiently large. The background and the object are non magnetic. To simplify the implementation, TM polarization of the incident field is considered. For generating synthetic scattered data for inversion, the incident fields for the different transmitter view are generated using infinite line source expressions with N_t three dimensional line sources (two

dimensional point sources) equi-spaced on a circle in the measurement domain. The incident field for a transmitter view v is given by the electric field expression for a line source,

$$\psi_v^{inc}(r_T, r) = \frac{j}{4} H_0^2(k_b(r_T - r)) \tag{5.1}$$

where $r_T = (x_T, y_T)$ is the transmitter antenna coordinate and $r = (x, y)$ [10]. A time convention of $e^{j\omega t}$ is assumed. At a given time one of the antennas will be emitting and the others will be receiving. i.e., the number of receivers per view is $N_t - 1$. The scattered field is measured for different views. The measurement domain is outside the investigation domain. The circular geometry is selected for the following reasons:

a) Scattered information is collected all around the object for each incidence [11].

b) It helps in the computation of the degree of symmetry for the different transmitter positions, as will be shown in the following discussion.

5.3 Degree of Symmetry Formulation for localizing the scatterer

Synthetic scattered field for inversion is generated via the coupled Matrix equations (3.25) and (3.26). The degree of symmetry ($D.O.S$) for a transmitter position v is defined as (assuming even number of receivers $N_t - 1$ per view)

$$D.O.S(v) = abs\left[\sum_{k=1}^{(N_t-1)/2}\left\|(\psi_v^s(k)-\psi_v^s(N_t-k))\right\|^2\right], v=1,2...N_t \qquad (5.2)$$

and

$$D.O.S(v) = abs\left[\sum_{k=1}^{(N_t/2-1)}\left\|(\psi_v^s(k)-\psi_v^s(N_t-k))\right\|^2\right], v=1,2,...N_t \qquad (5.3)$$

when there are odd numbers of receivers per view, i.e., N_t-1 is odd.

Thus the *D.O.S* for a transmitter position is a function of the Euclidean distance between the first half and the spatially reflected second half of the measured scattered field vector, and the transmitter v is at the centre of the measurement points employed for computing the degree of symmetry value. The *D.O.S* value will be equal to zero when the two halves are exactly similar and maximum when they are most dissimilar.

When circular geometry of measurement is employed and if the dielectric cylinder is circularly symmetric and off centered, the measured scattered field vector ψ_v^s exhibits symmetry with respect to its centre, only for the views v_1 and v_2 that are diametrically opposite, as shown in figure 5.2.
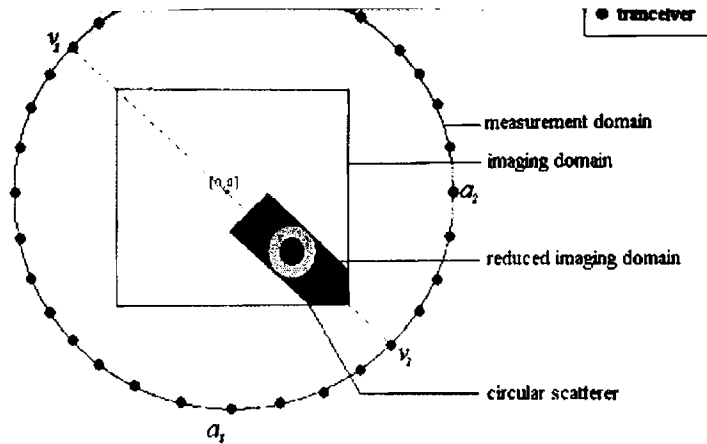
Figure 5.2

v_1 and v_2 are the maximum symmetric views, while a_1 and a_2 are the maximum asymmetric views.

The symmetry plots also exhibit two maxima, a_1 and a_2 which correspond to the transmitter positions where the symmetry of the measured scattered field vector is least. The plot of *D.O.S* with respect to v, exhibits two significant minima, at v_1 and v_2, and two significant maxima at a_1 and a_2 as shown in the example in figure 5.3.

This means that the object centre is located in a line joining the views v_1 and v_2. It is clear that a_1 and a_2 will be symmetrically located with respect to both v_1 and v_2. When the centre of the circularly symmetric scatterer is much closer to v_2 than to v_1, a_1 and a_2 will be closer to v_2 than to v_1.
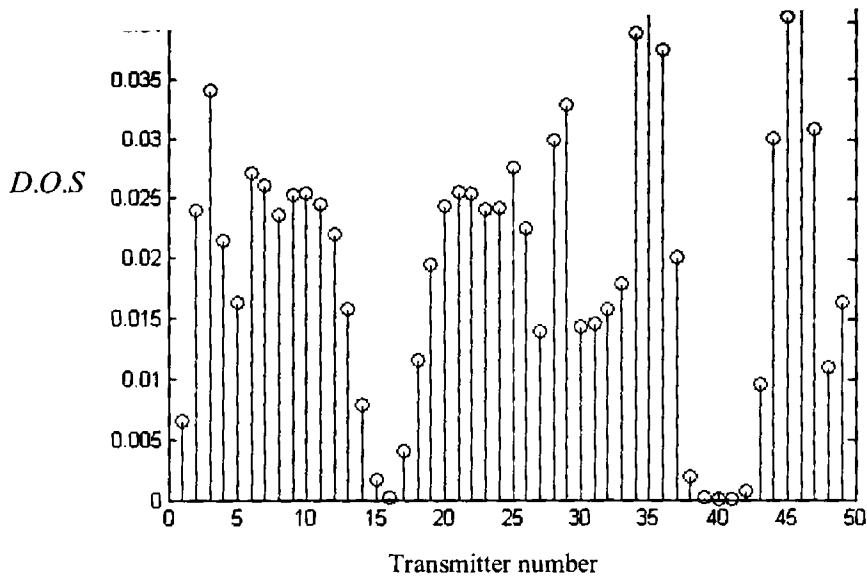
Figure 5.3
The degree of symmetry values are plotted for various transmitter positions. The minimum values indicate the maximum symmetric positions and the maximum values indicate the maximum asymmetric positions. In the above example, there are 49 line sources in D_M. The centre of the cylinder lies in the line connecting transmitter 16 and 40.

This is explained as follows: the scattered field at a measurement point depends on the distance to the scatterer via the Greens function, and the field inside the object which is a function of the object contrast and the incident field. When the transmitter is at position v_1 or v_2, the field inside the object is symmetric about the line joining v_1 and v_2. Since the receivers are symmetrically located with respect to the scatterer, the measured scattered field vector will be symmetric about its centre. However when the transmitter position is moved to either side of v_2 or v_1, the distances from the adjacent symmetrically located receivers on either side of the transmitter, to the circularly symmetric scatterer are different. This difference is more

pronounced when the transmitter position is moved away from v_2, than when the transmitter position is moved away from v_1.

Also the incident field at the position of the scatterer will exhibit a marked difference in symmetry about the line joining v_1 and v_2, the maximum symmetry direction, when the transmitter position is moved away from v_2 than v_1. This is because the field is inversely related to the distance. The distance from the transmitter to the position of the scatterer exhibits a larger variation when the transmitter is moved away from position v_2 than when moved away from position v_1 along the measurement domain. Therefore the asymmetric points in the symmetry plots will be closer to v_2 than v_1, when the scatterer is much closer to v_2 than v_1. The values of $D.O.S$ at a_1 and a_2 will be much larger when the scatterer is farther from the centre of the investigation domain than when it is closer. Also when the scatterer is close to the centre of the investigation domain, the maximum asymmetry positions a_1 and a_2 will be almost equidistant from the symmetry positions v_1 and v_2. However if the object centre and the centre of the investigation domain coincide, the measured scattered field vector for all the views will be symmetric with respect to its centre and hence the degree of symmetry values for all the views will be very small. Since the maximum diameter possible for the unknown object is assumed to be known, a reduced image may be defined at the centre of the investigation domain in this case.

Thus by measuring the maximum value of $D.O.S$ and the distance between the maxima, and also noting the direction of

symmetry of the scattered field, it is possible to localize the 2-D circularly symmetric dielectric scatterer in the investigation domain. Thus a new reduced investigation domain $I_r \supset I$ may be defined. This is illustrated in the following numerical example. Since a reduced investigation region is employed, the number of degrees of freedom is reduced and there is a larger data redundancy from which better reconstructions may be obtained. The computation time per iteration for the direct solution of the scattering integral equations is $O(N^3)$, N being the number of cells into which the investigation domain is reduced. This is now reduced to $O(N_r^3)$ where N_r is the number of pixels in the reduced imaging domain.

5.4 Simulations and Discussions

Some typical symmetry plots are considered in figure 5.4. Here, 49 line sources are equi-spaced in the measurement domain for generating the synthetic scattered field data using the coupled state and observation equations. The incident field frequency employed for the simulations is 3 GHz. The transmitter 1 is at the zero degree position with the antennas numbered in the ascending order in the anticlockwise direction as shown in figure 5.1. For the forward problem, the investigation domain is discretized at a fine resolution of $\frac{\lambda}{20}$, i.e., each cell is a $0.5\,cm\,x\,0.5\,cm$ square. This is done because the forward problem needs to be solved accurately [12]. The cross sectional profiles for the dielectric scatterer considered are a homogenous profile and a profile consisting of two concentric circles,

108

which are usually the practical cases considered for the dielectric pipeline.

The synthetic scattered field in the measurement domain for inversion is generated by employing the following parameters for the object profiles:

- The diameter is varied in the range between 6 and 11 sampling intervals.

- The relative permittivity of the scatterer is varied in the range [1:16].

- The offset of the centre of the cylinder cross section from the centre of D_{obj} is varied in steps of one sampling interval.

In practice the scattered field data is corrupted by measurement noise. Therefore random white Gaussian noise is added to the synthetic scattered data to generate the measurement data for inversion. The Signal to Noise Ratio is defined as

$$\frac{S}{N} = 10\log_{10}\frac{\left\|\psi^{s}\right\|^{2}}{\left\|n\right\|^{2}}\, dB \tag{5.4}$$

The symmetry plots have been generated from noisy measurement data with an SNR of 10 dB. The symmetry positions are 19 and 44, which are the diagonal transmitter views, with the transmitter view 1 at the 0 degree position. The distances between the asymmetry positions through 19 and through 44 along the measurement circle are not as different in figure 5.4 a, as in figure 5.4 b. The peak values at the asymmetry positions are much smaller in

figure 5.4 a than in figure 5.4 b, indicating that the cylindrical scatterer is very close to the origin in the first example and farther away from the origin and closer to the transmitter position 44 in the second case . In the case of figure 5.4 c, the degree of symmetry values for the entire transmitter positions are very small, indicating that the object centre and the centre of the imaging domain coincide.

One way to choose the reduced imaging domains in the three cases in figure 5.4 is indicated in figure 5.5. The reduced regions in figures 5.5 a and 5.5 b are chosen as overlapping by the maximum radius of the scatterer. This is to avoid the possibility of the scatterer not being fully located in either of the reduced regions. The dimensions of the reduced investigation strip are dictated by the maximum possible diameter of the circular scatterer. It is to be noted that the reduced regions are always oriented in the v_1 to v_2 direction. As an example consider the circular dielectric scatterer of circular cross section located in the investigation domain as shown in figure 5.6. The figure 5.7 shows the reconstructed image when the entire imaging region is employed. The Newton Kantorovich (NK) Procedure is stopped after the tenth iteration as the relative residual error $Err(\psi^s)$ is seen to increase afterwards. It is obvious that the NK procedure has not converged.
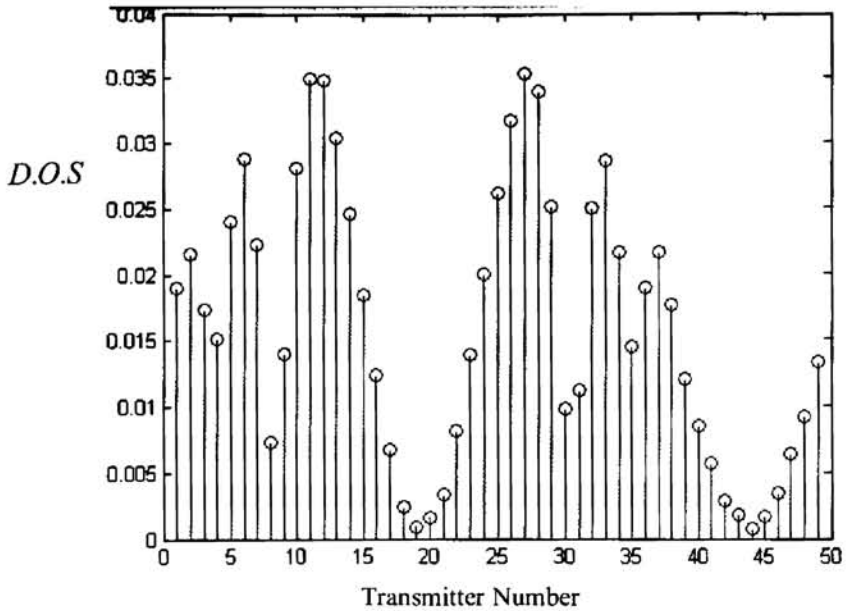
Figure 5.4 a

The centre of the cylinder cross section lie in the line joining the diagonal transmitters 19 and 44 and is close to the centre of the investigation domain.
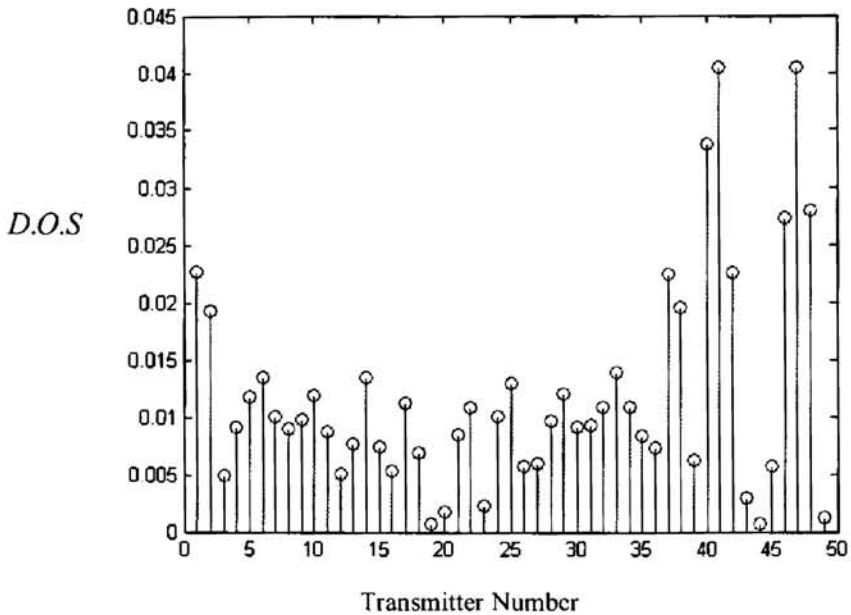
Figure 5.4 b

The centre of the cylinder cross section lie in the line joining the diagonal transmitters 19 and 44 and is close to the transmitter 44

Transmitter Number
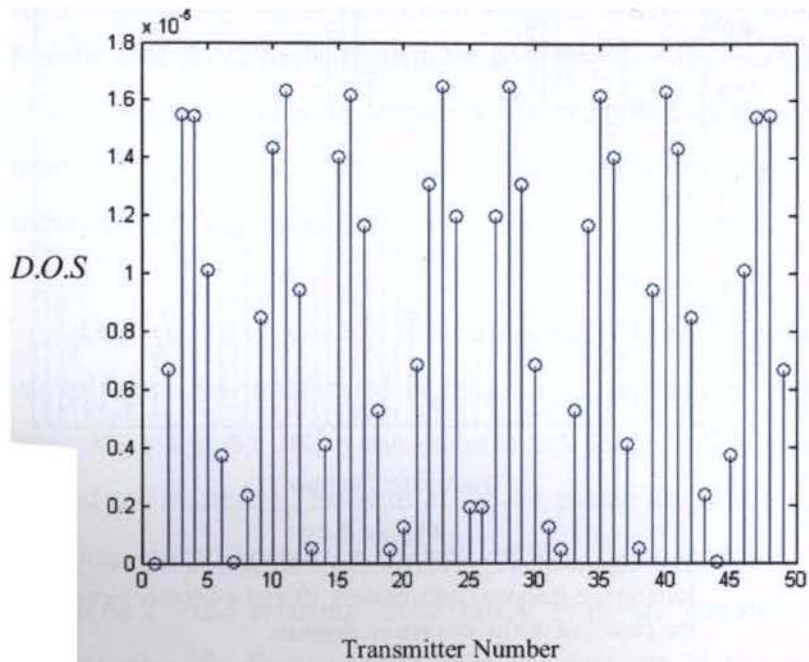
Figure 5.4 c

The centre of the cylinder cross section coincides with the centre of the imaging domain, as indicated by the extremely low *D.O.S* values
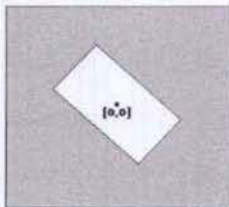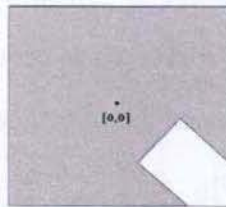
Figure 5.5 a **Figure 5.5 b** **Figure 5.5 c**
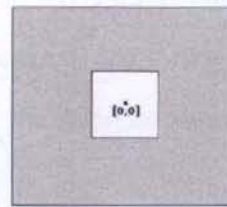
a. reduced imaging region for the symmetry plots in figure 5.4 a
b. reduced imaging region for the symmetry plots in figure 5.4 b
c. reduced imaging region for the symmetry plots in figure 5.4 c
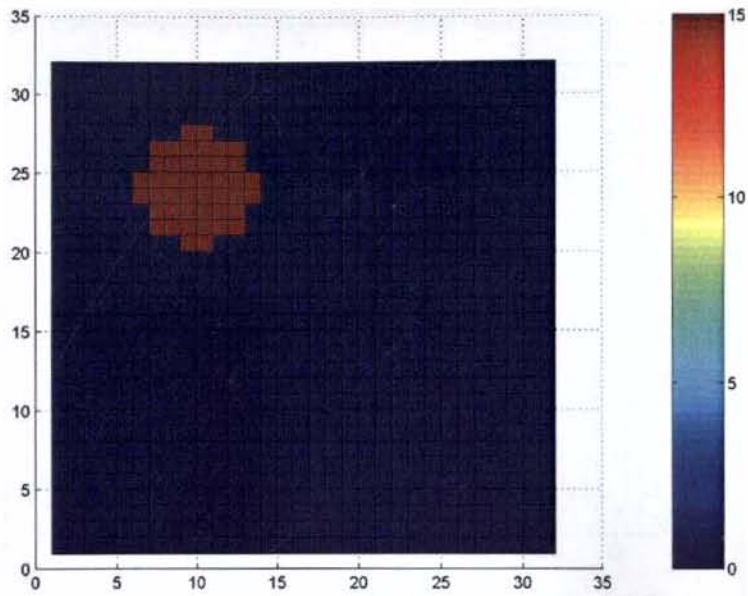
Figure 5.6
The actual profile of a two dimensional
circularly symmetric scatterer
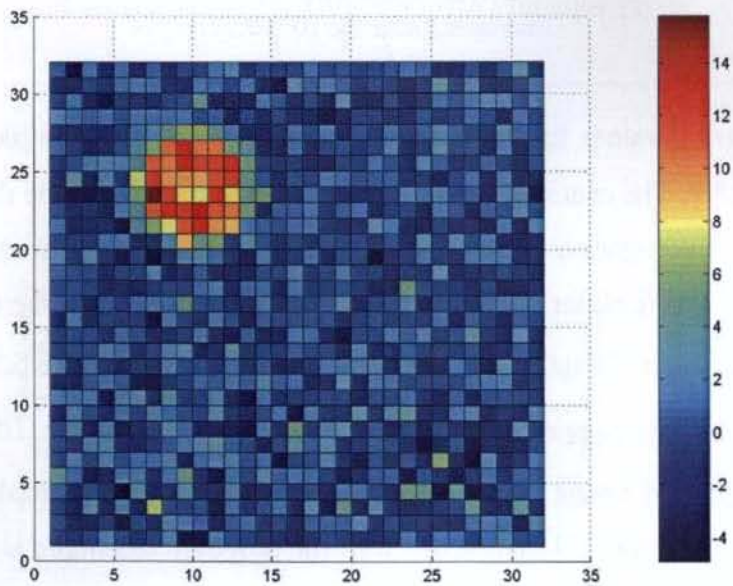
Figure 5.7
The reconstructed permittivity profile using the
Newton Kantorovich Procedure . The entire
investigation domain is employed
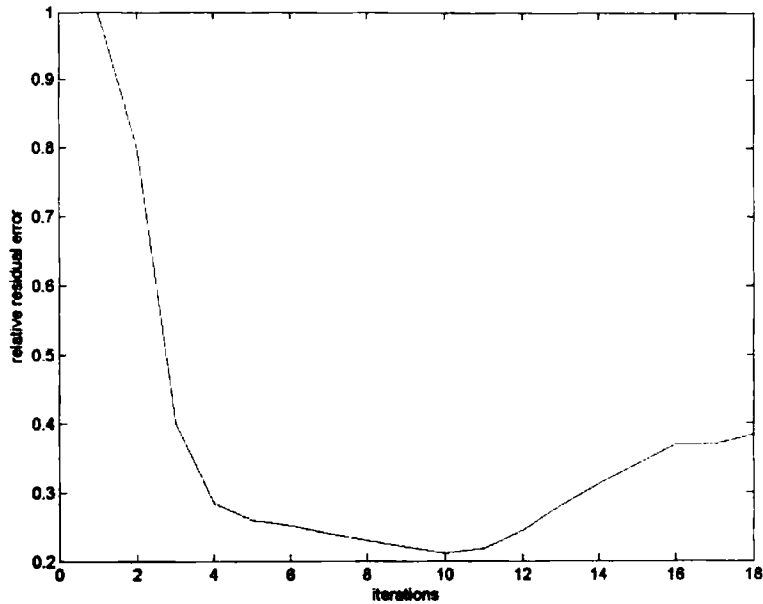
Figure 5.8
The Relative Residual error starts
increasing after the 10th iteration

The *D.O.S* values for the different transmitter positions are plotted in
figure 5.9. The centre of the scatterer cross section lies on the diagonal
of the investigation domain, i.e., the line joining the transmitters 19
and 44, and is closer to the transmitter 19. The variation of the relative
residual error $Err(\psi^s)$ with the iterations is shown in figure 5.10. The
iterations are stopped when $Err(\psi^s)$ reduces below 2.0×10^{-2}. The
reconstructed image when the reduced imaging region is employed is
shown in figure 5.11. The result with the proposed technique is seen to
be much better, in addition to the reduction in the computational time
per iteration from $O(N^3)$ to $O(N_r^3)$.

Transmitter Number
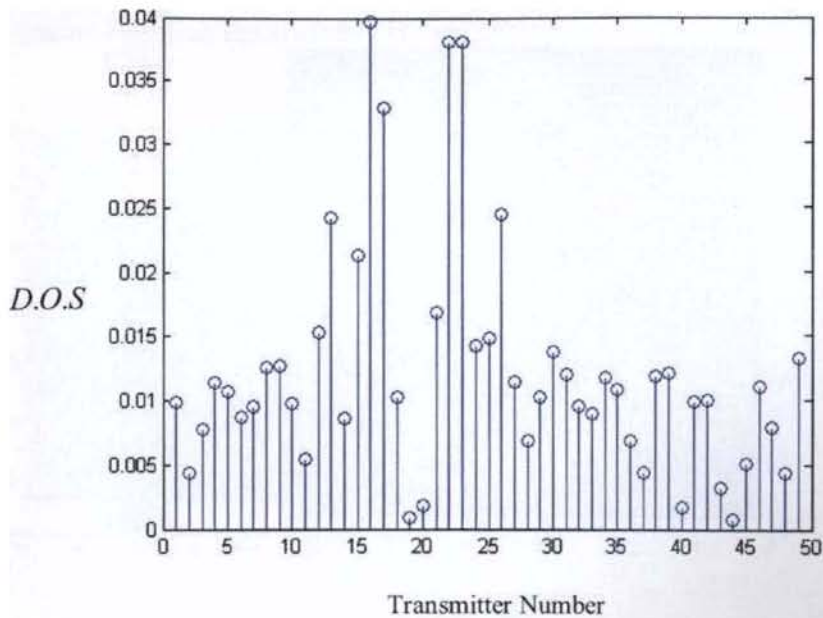
Figure 5.9

The $D.O.S$ values for the different transmitter positions for the scatterer in figure 5.6. The centre of the scatterer lies on the leading diagonal and is closer to the transmitter 19.
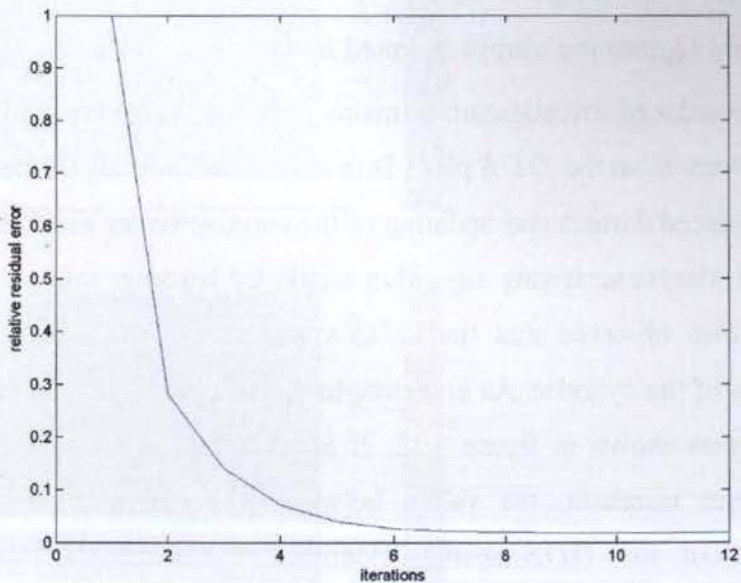
Figure 5.10

The iterations are stopped when $R.R.E$ reduces below the selected threshold, in the 10th iteration
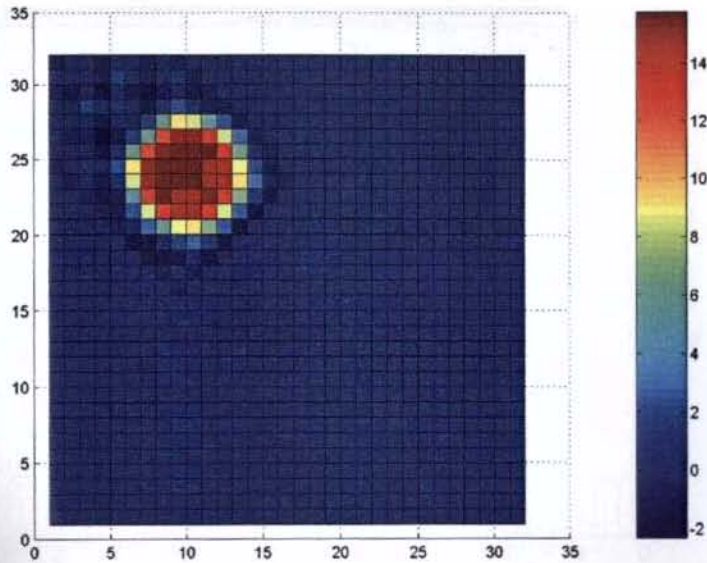
Figure 5.11
The reconstructed image when the reduced
investigation region is employed.

However the strategy has the disadvantage in that the reduced imaging domain is no longer a square or rectangle. In addition, since the reduced regions are always oriented in the v_1 to v_2 direction, the shapes of the reduced investigation domains will depend on the direction of symmetry from the $D.O.S$ plot. Due to this, the ordering of the cells in the reduced domain and updating of the contrast vector in all iterations of the inverse scattering algorithm employed becomes more involved. It is also observed that the $D.O.S$ vector is also influenced by the radius of the cylinder. As an example consider the $D.O.S$ plots for the scatterers shown in figure 5.12. It is seen that as the radius of the scatterer increases, the valley between the maximum asymmetric points of the $D.O.S$ vector widens. This means that a further localization of the investigation domain can be achieved if the radius information can be extracted in addition to the offset from the centre of D_{obj}. Therefore the problem was reeast as a pattern classification

problem, where the classes indicated the reduced investigation domains in which the scatterer is located.
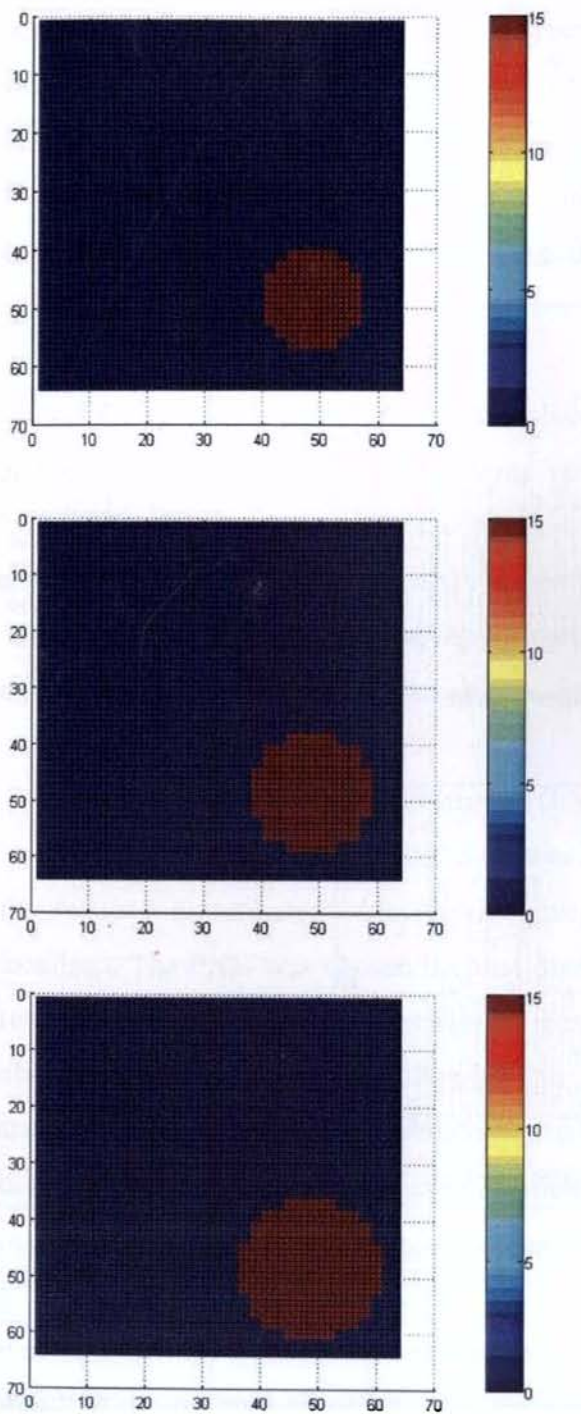
Figure 5.12 a
Permittivity profiles of three scatterers of increasing radii located in the investigation domain

D.O.S

Transmitter Number

D.O.S

Transmitter Number
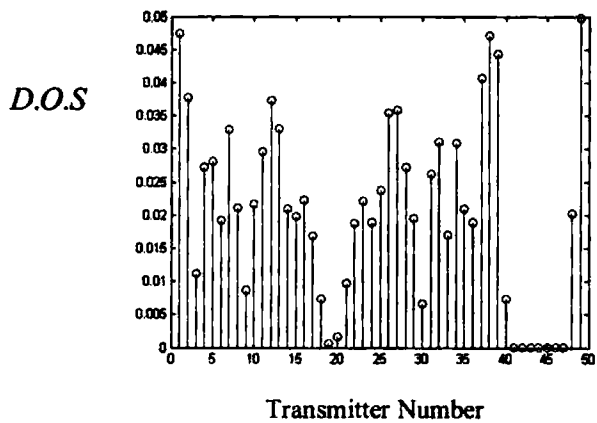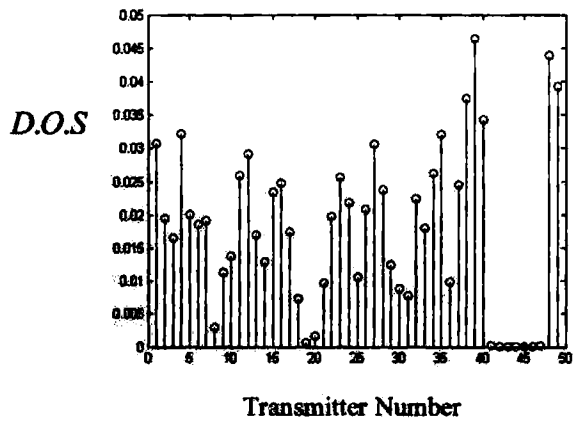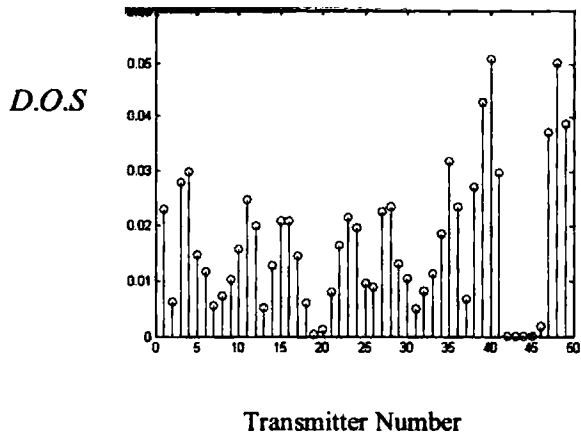
Figure 5.12 b
The valley between the maximum asymmetric points of the *D.O.S* plots widens with increasing radius

D.O.S

Transmitter Number

For this purpose, a neural network based classifier was employed. Neural networks offer an advantage in that they can work as a black box system capable of solving the physical problem without directly considering the physical relationship between the input and the output values of the problem itself [13]. Neural Networks have been employed for the solution of electromagnetic inverse problems [14, 15]. However Neural Networks are used here to localize the scatterer in the investigation domain as a preprocessing step prior to the inverse scattering.

The primary requirement of the classifier here is fast training and easy retrainability. The paradigms such as Back Propagation Neural Networks are characterized by slow training times. They are also not easily retrained. i.e., when a new training pattern is to be incorporated into the training set, the network will have to be retrained again with the updated set of training data, from the start [16].

The Probabilistic Neural Network (PNN) paradigm was chosen to classify the training set of *D.O.S* vectors into classes that indicate the reduced investigation domains in which the cylinder could be localized. The PNN was chosen because of its rapid training and easy retraining ability. The PNN provides a general solution for pattern classification problems by following an approach developed in statistics, called Bayesian classifiers [17]. It also gives an evidence estimate based on which the classification decision is made. The network paradigm also uses Parzen Estimators, which were developed to construct the probability density functions required by Bayes' theory. The PNN is guaranteed to converge to the Bayesian classifier, which is the optimal classifier, with enough training data. It is also

robust in the presence of noise and generalizes well. The architecture
of the PNN is shown in figure 5.13.
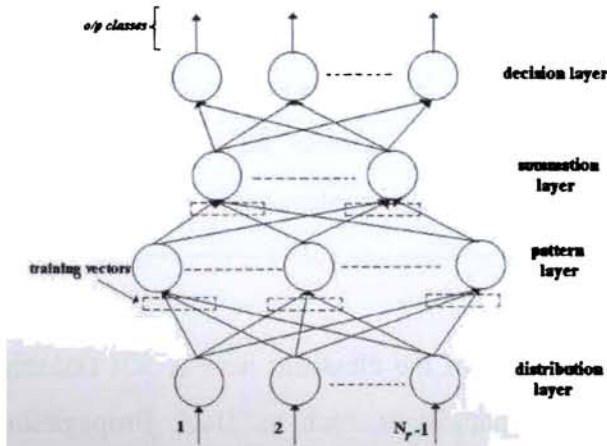
Figure 5.13
PNN architecture
The input test $D.O.S$ vector is classified into one
of the target output classes that indicate the
localized investigation domain

The network has four layers: an input distribution layer, a
pattern layer, a summation layer and an output decision layer. The
distribution layer has as many elements as there are separable
parameters needed to describe the objects to be classified. Pattern layer
organizes the training set such that each input vector is represented by
an individual processing element. The pattern layer weight matrix is
set to the transpose of the matrix formed from the input training set, in
this case, the training set of $D.O.S$ vectors. The pattern layer transfer
function is the Gaussian Probability function centred at each training
case. When the standard deviation of the Gaussian function is
approaching zero, the PNN approximates a nearest neighbor classifier

and when it approaches infinity, the classifier is limited to functions that are linearly separable. Some intermediate value of the spread is usually employed. For the simulations a spread value of 0.1 was employed.

The training set is minimized by considering only diagonal displacements along the leading diagonal of the centre of the circular symmetric scatterer from the centre of the imaging domain. Each output target class indicates the offset from the centre and the range of radii the unknown circularly symmetric scatterer belongs to. The weight matrix of the summation layer is derived from the target classes.

Since the training data consists of scatterers that are displaced only along the main diagonal, the test degree of symmetry vector is circularly shifted in the anticlockwise direction by n elements, so that the two minima of the degree of symmetry are aligned with the views v_1 and v_2 of the main diagonal. The PNN classifies the test degree of symmetry vector into one of the target classes that indicates the offset and range of radii the circularly symmetric scatterer belongs to. The reduced investigation domains are indicated by the output classes. The reduced domains are chosen to be overlapping by the maximum radius of the scatterer in them so as to avoid the possibility of the scatterer not being fully located in either of the reduced regions. For the radius of the scatterers chosen as mentioned earlier, the reduced investigation domains are chosen as squares of dimensions $14x14, 18x18$ and $24x24$ cells containing circular scatterers of outer radii in the range $3-5, 6-8$ and $9-11$ cells respectively.

An example is shown in Figure 5.14. The synthetic data is generated from the profile shown in Figure 5.14 a. The degree of symmetry for the scatterer is shown in Figure 5.14 b.
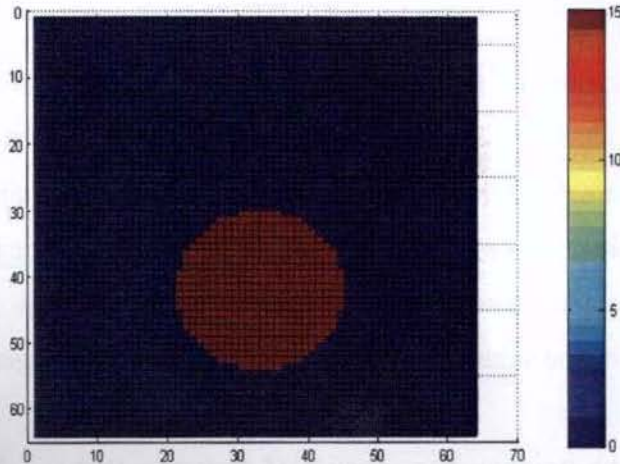
Figure 5.14 a
The actual profile of the scatterer employed to generate synthetic scattered data
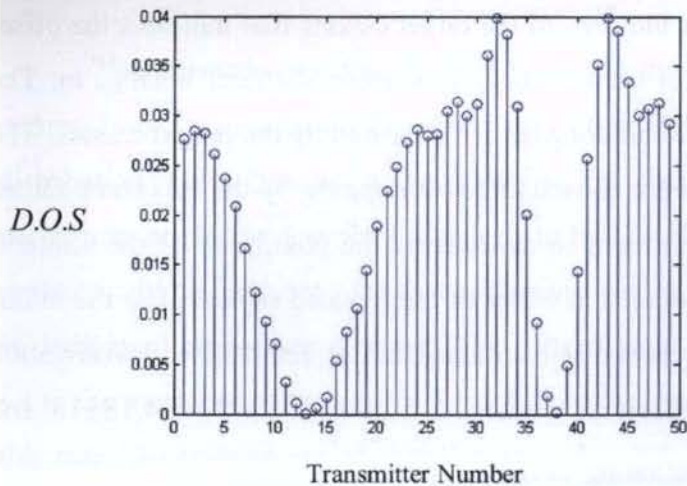
Figure 5.14 b
The computed *D.O.S* vector for the above profile

Since the training data consists of scatterers that are displaced only along the main diagonal, the test degree of symmetry vector is circularly shifted in the anticlockwise direction by n elements, so that the two minima of the degree of symmetry are aligned with the views v_1 and v_2 of the main diagonal. The rotated *D.O.S* is shown in figure 5.14 c.

Transmitter Number
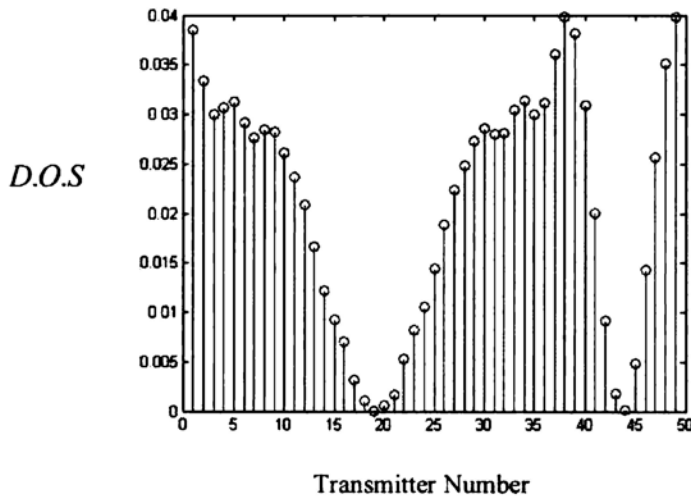
Figure 5.14 c
The *D.O.S* vector is circularly shifted
so that it is oriented in the direction of
the main diagonal.

The reconstructed image in the 10th iteration of the Newton Kantorovich procedure, considering the entire investigation domain, is shown in figure 5.14 d. The relative residual error $Err(\psi^s)$ varies with the iterations as shown in figure 5.14 e.
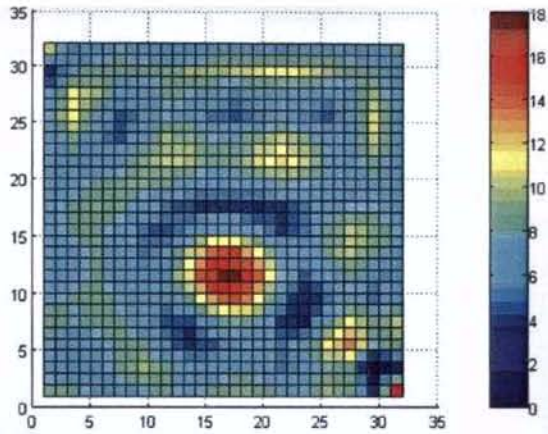
Figure 5.14 d
The reconstructed image considering the entire
investigation domain after the 10th iteration of the
NK procedure
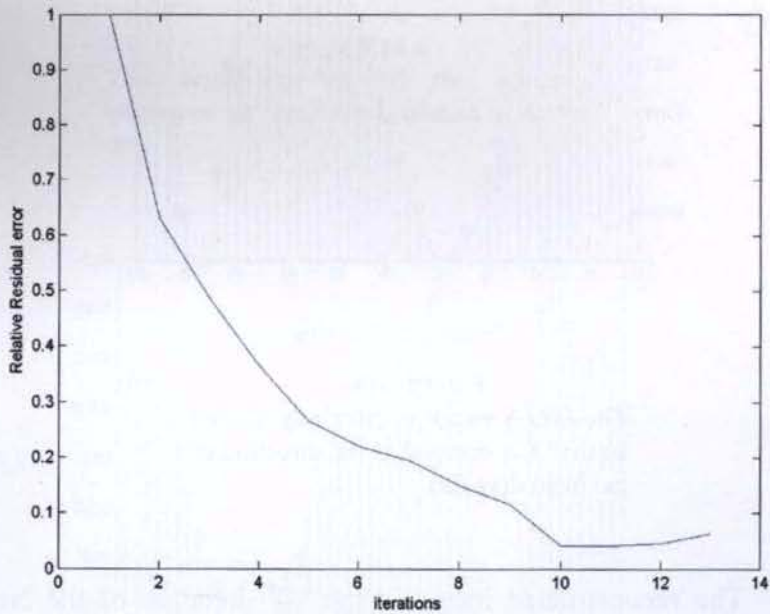
Figure 5.14 e
$Err(\psi^s)$ is found to increase after the 10th iteration
Therefore the NK procedure is stopped after the 10th
iteration.

The PNN classifier classified the circularly shifted *D.O.S* vector in
figure 5.14 c into a reduced target domain of 18 x 18 cells where the

scatterer is located. The final reconstructed image is rotated in the clockwise direction about the centre of the investigation domain by $\dfrac{360^0 . n}{N_t}$ .The reconstructed image is rotated back in the clockwise direction by when the reduced investigation domain is considered is shown in the figure 5.14f. The NK procedure converges in the 10th iteration indicated by the plot of $Err(\psi^s)$ vs. iterations as shown in figure 5.14 g
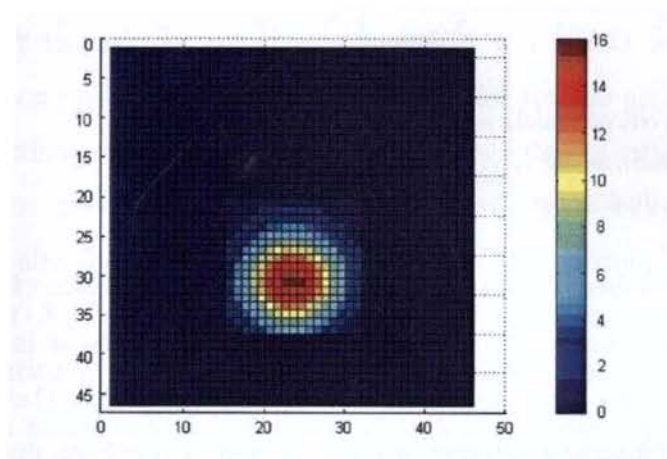
Figure 5.14 f
. The reconstructed image considering a reduced investigation domain of 18 x 18 cells
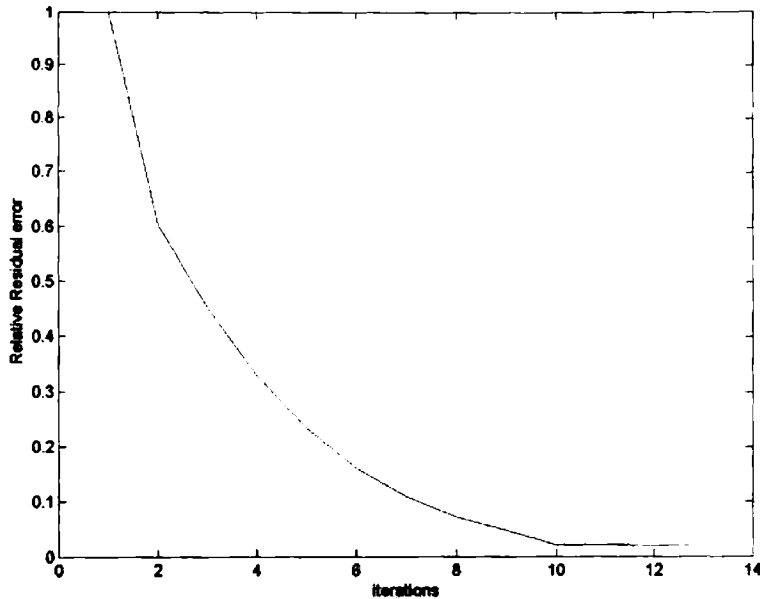
Figure 5.14 g
The NK procedure is stopped after the tenth
iteration as the $Err(\psi^s)$ decreases below the
specified threshold of 2.0×10^{-6}

The *D.O.S* formulation for circular scatterers was successfully applied to the case when only aspect limited data is available as in the case of inverse profiling of buried dielectric cylinders. The ill posedness of the inverse scattering problem is more severe here, due to the availability of only aspect limited data [5, 6].

Many algorithms have been designed to tackle the electromagnetic inverse scattering problem of imaging buried scatterers. For the detection of buried targets and landmines, a simple model has been proposed by using the Ground penetrating radar (GPR) technique, without accounting for the air-earth interface [18, 19]. To build up more accurate models, a half space problem must be considered to represent the air-earth interface. Several methods that include the modified gradient approach [20, 21], Born iteration and constrained

optimization [5], Distorted Born Iterative method [6] and high-order extended Born approximations [7] have been investigated for the buried object problem.

The cross sectional profiles considered for the cylinder are a homogenous profile and a cross sectional profile of two concentric circles, which are the practical cases for a buried pipeline. The investigation domain is illuminated with TM polarized electromagnetic radiation so that the scattering problem reduces to a scalar one. Scattered data can be measured only in a limited angle, as the imaging domain is inaccessible. The following situation is investigated: the pipeline is buried in wet soil in which case a half space problem is considered to account for the air-soil interface. A localization of the dielectric pipeline in the investigation domain is done prior to the cross sectional profiling, which will reduce the number of unknowns. For this, the custom defined scalar *D.O.S* parameter is computed for every transmitter view. Thus for a particular object configuration, the *D.O.S* vector, which comprises of the scalar values computed for each transmitter view maybe formed. The PNN is trained with the degree of symmetry vectors computed for a training set of object configurations, which classifies the degree of symmetry vector of the unknown scatterer presented to it into one of the classes that indicate the localized region in the investigation domain, prior to the inverse scattering.

5.5 Formulation of the buried pipeline scattering problem

The investigation domain D_{obj} is chosen to be a square or rectangle that possibly contains the buried dielectric pipeline. This should be large enough to include all possible locations of the buried pipeline. The axis of the pipeline is oriented in the z direction so that the cross section lies in the $x - y$ plane. Both media and the scatterer are assumed linear, isotropic, non magnetic and penetrable.

When the transmitters and receivers are mounted at the same height, the Greens functions $g_{m_2 m_2}$ and $g_{m_1 m_2}$ maybe simplified as [6]

$$g_{m_2 m_2} = \frac{j}{4}[H_0^2(k_{m_2}|r - r'|) - H_0^2(k_{m_2} r_I)] + \frac{j}{4\pi} g_1(r,r') \qquad (5.5)$$

and

$$g_{m_1 m_2} = \frac{j}{4\pi} g_2(r_R, r), \qquad (5.6)$$

The transmitters are ideal time harmonic electric current line sources, set parallel to the z-axis (TM polarized), and mounted at a height y_0 from the origin in the measurement domain D_M. The incident field is given by

$$\psi_v^{inc}(r_T, r) = jk\eta_0 I g_{m_2 m_1}(r, r_T) \qquad (5.7)$$

where,

$$g_1(r,r') = \int\limits_{-\infty}^{+\infty} dk_x g_0(k_x) e^{jk_{m_2y}(2h-y-y')} e^{jk_x(x-x')} \qquad (5.8)$$

and

$$g_2(r_0,r) = \int\limits_{-\infty}^{+\infty} dk_x g_0(k_x) e^{j[k_{m_1y}(y_0-h)+k_{m_2y}(h-y)]} e^{jk_x(x-x')} \qquad (5.9)$$

Here $g_0(k_x) = \dfrac{2}{(k_{m_{2y}} + k_{m_{1y}})}$ and $r_l = \sqrt{(x-x')^2 + (y+y'-2h)^2}$. r_R and

r_T are the receiver and transmitter coordinates respectively. The y - axis passes through the central transmitter. The receivers are also ideal and the number of receivers is one more than that of the transmitters, as there will be a receiver antenna on either side of a transmitter antenna. The measurement setup is assumed movable in the x direction. The scattering problem is scalar, and only the z component of the scattered field is needed.

The geometry of the problem is as shown in figure 5.15, where the homogenous half spaces, air and wet soil, are separated by a planar interface.
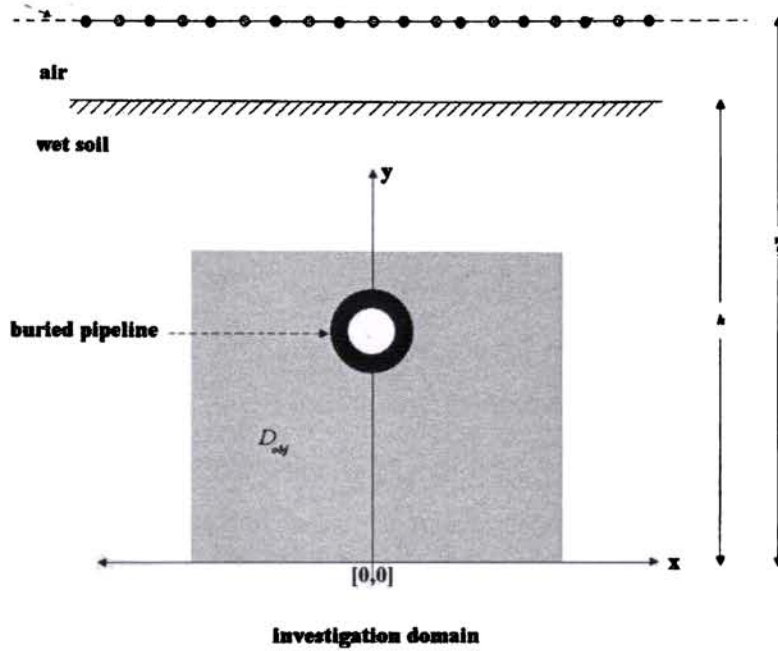
Figure 5.15
The measurement setup for imaging the buried pipeline Transmitters and receivers are ideal line sources mounted at the same height above the air-soil interface

5.6 Degree of Symmetry Formulation for localizing the buried pipeline

The degree of symmetry ($D.O.S$), for the transmitter view v is defined as (assuming even number of receivers N_r per view)

$$D.O.S(v) = abs\left(\sum_{k=1}^{N_r/2} \left\| \psi_v^s(k) - \psi_v^s(N_r + 1 - k) \right\|^2 \right), v = 1, 2, 3 \ldots \ldots N_r - 1$$

(5.10)

In equation 5.10, the degree of symmetry for any given transmitter view v is computed with all the measured scattered values employed for the calculation, with the central transmitter numbered as $\frac{N_r}{2}$. Thus the $D.O.S$ for a transmitter position is a function of the Euclidean distance between the first half and the spatially reflected second half of the measured scattered field vector .The $D.O.S$ value will be equal to zero when the two halves are exactly similar and maximum when they are most dissimilar. The two halves of the exact measured scattered field vector are identical only for case of the central view $v = \frac{N_r}{2}$ and when the circularly symmetric pipeline cross section lies symmetric with respect to the measurement array with its centre on the y - axis as in figure 5.15. The measurement setup is moved in the x direction until the $D.O.S$ for the central transmitter is minimum, which is when the centre of the pipeline cross section coincides with the y -axis. For this purpose a modified degree of symmetry is computed for each transmitter position as follows:

for $v = 1 : \frac{N_r}{2}$,

$$\psi_{vL} = \psi_v^s(r), r = 1, 2, ... v$$

$$\psi_{vR} = \psi_v^s(r), r = 2v, 2v-1, 2v-2, ... v+1$$

for $v > \dfrac{N_r}{2}$,

$$\psi_{vL} = \psi_v^s(r), r = 2v - N_r + 1, \ldots v$$

$$\psi_{vR} = \psi_v^s(r), r = N_r, N_r - 1, N_r - 2, \ldots v + 1$$

$$D.O.S_{\text{mod}}(v) = \frac{1}{(size(\psi_{vL}))^2} abs(sum(\psi_{vL} - \psi_{vR})^2) \qquad (5.11)$$

Thus the lengths of the first half vector ψ_{vL} and the spatially reflected second half vector ψ_{vR} are equal for a given transmitter view v. In (5.10), the degree of symmetry for any given transmitter view v is computed with all the measured scattered values employed for the calculation, whereas in (5.11), the transmitter v is always at the centre of the measurement points employed for computing the modified degree of symmetry. If the buried 2-D cylindrical pipeline is located under a transmitter offset from the central transmitter as shown in figure 5.16 a, the $D.O.S_{\text{mod}}$ value will be equal to zero for that view as shown in figure 5.16 b. The measurement setup is now moved in the x direction such that the minimum value of $D.O.S_{\text{mod}}$ now coincides with the central transmitter $\dfrac{N_r}{2}$, which is when the centre of the pipeline cross section coincides with the y-axis as in figure 5.15. The new $D.O.S_{\text{mod}}$ vector is plotted in figure 5.16 c where the minimum value is for the central transmitter. The scalar $D.O.S$ values are then computed for each transmitter position, which together constitutes the $D.O.S$ vector. In this case, $D.O.S$ vector will be symmetric with respect to its centre, where it has its minimum value.
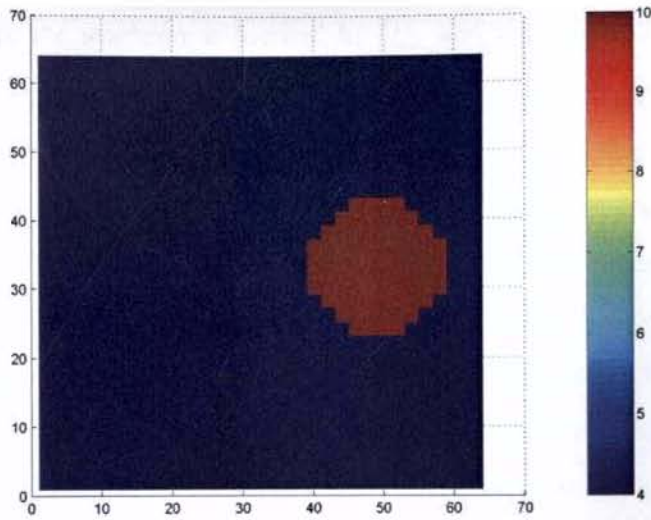
Figure 5.16 a
A 2-D dielectric pipeline with circular cross section is located with its centre displaced to the right of the centre of the investigation domain

10
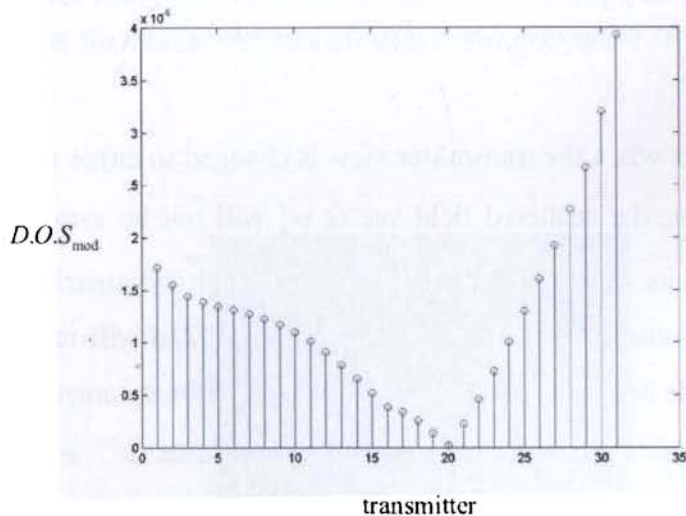
transmitter

Figure 5.16 b
The modified degree of symmetry $D.O.S_{mod}$ is plotted for the pipeline in figure 2. a. For the simulation 31 transmitters have been employed. The plot shows that the pipeline centre is located under the transmitter 20. The measurement setup is to be moved by 4 transmitter spacing to the right so that the minimum of $D.O.S_{mod}$ is now aligned with the central transmitter 16.
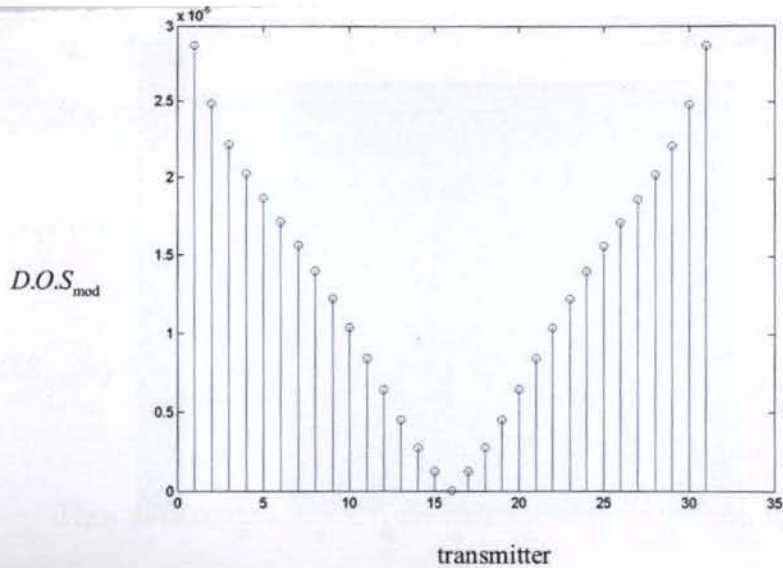
transmitter

Figure 5.16 c

The modified degree of symmetry $D.O.S_{mod}$ is plotted from the computed measured scattered field for the new position of the measurement array. The centre of the pipeline is now located under the central transmitter, as indicated by the minimum value of $D.O.S_{mod}$ coinciding with the central transmitter 16.

However when the transmitter view is changed to either side of the central view, the scattered field vector ψ_v^s will not be symmetric with respect to its centre as the receiver array is not symmetric with respect to the transmitter location. Therefore the $D.O.S$ will increase either side of the central view. There will be two views symmetrically located on either side of the central view where ψ_v^s is most asymmetric and hence the $D.O.S$ is maximum.

The measured scattered field vector is dependent on the distance of the receivers from the scatterer via the Greens function $G_{m_1 m_2}$ and the total field inside the object ψ_v which is a function of the object contrast c, the incident field ψ_v^{inc}. It is seen that

the geometric properties namely the inner and outer radii and the depth at which the scatterer is located in D_{obj} and the dielectric contrast of the scatterer influence the values and features of the $D.O.S$ vector. For example, consider the pipeline located at the top of the investigation domain, as shown in figure 5.17 a. The $D.O.S$ for this configuration is plotted in figure 5.17 b. The same pipeline is shown buried at a greater depth in figure 5.17 c and the corresponding $D.O.S$ is shown plotted in figure 5.17 d. In figure 5.17 e, the pipeline lies buried at the bottom of D and its $D.O.S$ is plotted in figure 5.17 f. It is observed from figure 5.17 that the $D.O.S$ values show a faster increase from the central minimum value to the maximum values on either side, when the object is located at a shallower depth in D_{obj}. The features of the $D.O.S$ vector maybe employed to localize the dielectric pipeline in D_{obj} as shown earlier, for which the PNN classifier is employed.
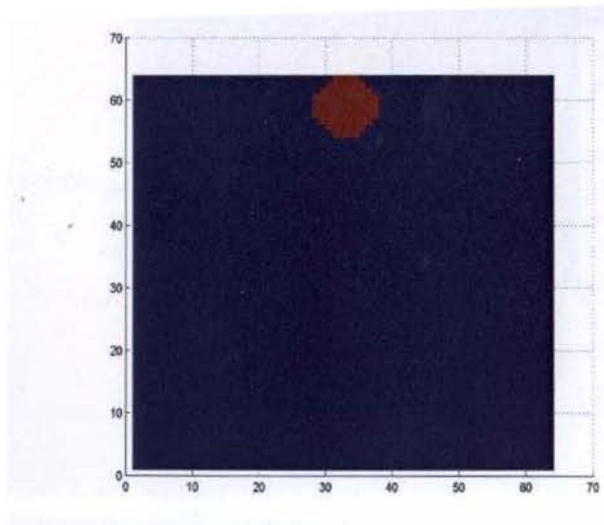
Figure 5.17 a
The pipeline is located at the top of the
investigation domain

transmitter
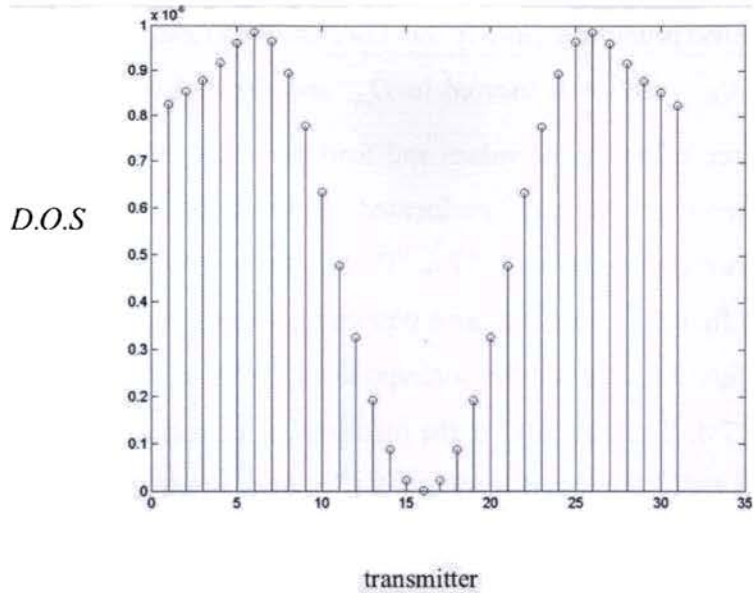
Figure 5.17 b
The $D.O.S$ plotted for the scatterer in figure 5.17 a
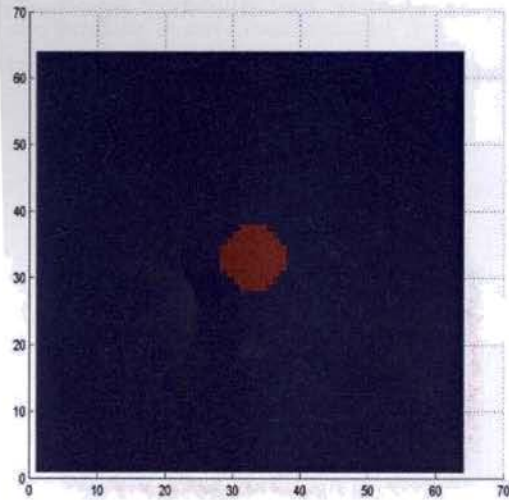
Figure 5.17 c
The same pipeline is located at a
greater depth in the investigation
domain
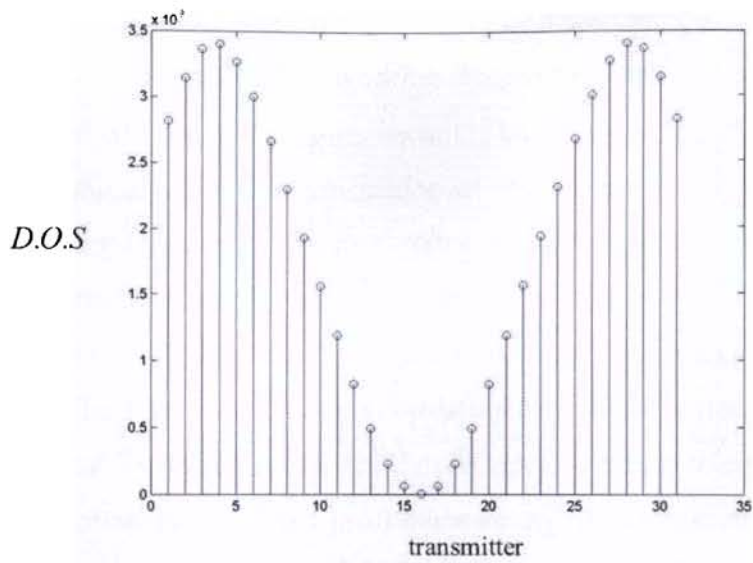
Figure 5.17 d
The $D.O.S$ plotted for the scatterer in figure 5.17 c. The maxima of the $D.O.S$ are spaced farther apart than in figure 5.17 b.
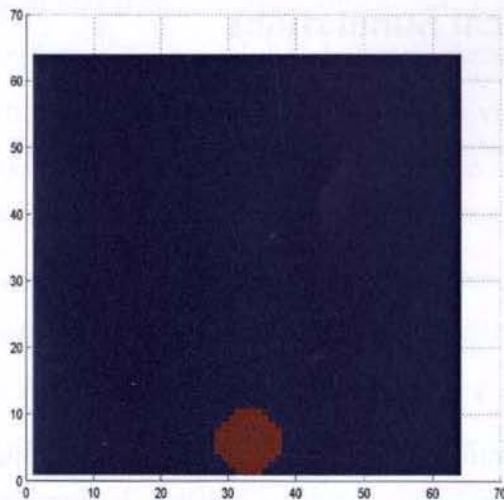
Figure 5.17 e
The pipeline is located at the bottom of the investigation domain

transmitter
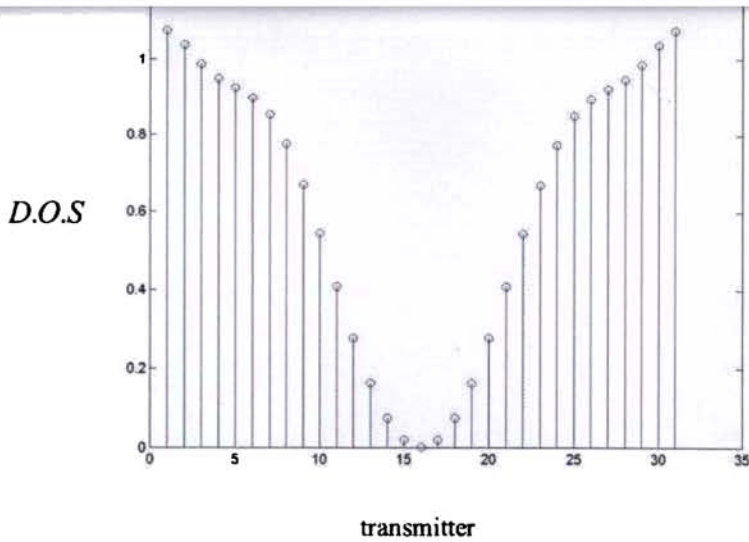
Figure 5.17 f
The *D.O.S* plotted for the scatterer in figure 5.17 e. The maxima of the *D.O.S* are spaced farther apart than in figure 5.17 d

5.7 Numerical Simulations

The upper region considered here is free space $\left(\varepsilon_u = 1, \sigma_u = 0\right)$ and the lower region is wet soil $\left(\varepsilon_s = 4, \sigma_s = 0.005\, s/m\right)$. The observation equation (3) and state equation (4) are employed for generating synthetic scattered field data in the measurement domain D_M, for various known circular object profiles buried in wet soil. For the simulation of the experiment, 31 transmitters have been employed in the measurement domain. For each transmitter view, 32 measurements are made at the receiving antenna positions as illustrated in figure 5.15. The investigation domain D_{obj} is chosen to be a square of 2 meters side. The top of the investigation domain is located at a depth of 2.25 meters from the air-soil interface. The measurement domain is located at a height of 0.75 meters from the air-

soil interface. The investigation domain is discretized into $64 \times 64 = 4096$ pixels. The working frequency employed is 100 MHz. Though a higher frequency would have improved the imaging resolution, the depth of penetration of the EM wave will reduce with increasing frequency. The measurement domain is 4 meters long with the transmitters equally spaced on the measurement line and receivers similarly arranged in between the transmitter positions as in figure 5.15. The measurement setup is assumed movable in the x direction. The cross sectional profiles for the dielectric scatterer considered are a homogenous profile and a profile consisting of two concentric circles, which are usually the practical cases considered for the dielectric pipeline. The measurement setup is moved in the x direction until the $D.O.S$ value for the central transmitter is minimum, which is when the centre of the pipeline cross section lies on the y-axis. The exact scattered fields in the measurement domain are generated with the following parameters of the cylindrical dielectric scatterer:

- For the homogenous profile, the diameter is varied in the range 15 centimeters to 45 centimeters. For the concentric circle cross section, the diameter of the outer cylinder is varied in the range 30 to sampling intervals to 45 sampling intervals, and the inner diameter between 5 sampling intervals and 10 sampling intervals.

- Two ranges of the relative permittivity of the dielectric pipeline are considered. A lossless scatterer is first considered having relative permittivity in the range 2 to 10. A lossy scatterer is also considered with the relative permittivity varied in the range 5 to 10 and conductivity in the range 0.001 to 0.010 S/m. The relative permittivity is varied in steps of 1 and the conductivity is varied in steps of 0.002 S/m.

- The depth at which the cylinder is located in D_{obj} is varied in steps of 2 sampling intervals.

The Distorted Born Iterative method (DBIM) is employed for the inverse scattering. The $D.O.S$ vectors for the various scatterer configurations are generated from the exact scattered data as per (5.10). A probabilistic neural network is trained with the training set of $D.O.S$ vectors. The training is virtually instantaneous and involves nothing more than reading in the training vectors and storing them as rows of the pattern layer matrix.

As an example consider the cylindrical dielectric scatterer $(\varepsilon = 10, \sigma = 0.01 s/m)$ of diameter 15 centimeters located at a depth of 0.5 meters from the top of the investigation domain, and the centre of the cross section offset to the right from the centre of the imaging domain by 38 centimeters as shown in figure 5.18 a. For the measured scattered field, an SNR of 30 dB is assumed. The $D.O.S_{mod}$ values computed from the measured scattered field are shown plotted in figure 5.18 b. The plot indicates that the pipeline is located under the transmitter 19. The measurement setup is moved by three transmitters spacing to the right so that the pipeline now lies under the central transmitter 16. The $D.O.S$, computed from the measured scattered field is plotted in figure5.18 c. The calculated $D.O.S$ vector is presented to the PNN, which classifies it into one of the target classes that indicate the location of the centre of the scatterer and its radius. The reconstructed permittivity and conductivity images, after the 20th DBIM iteration considering the entire imaging domain are shown in figure 5.19.
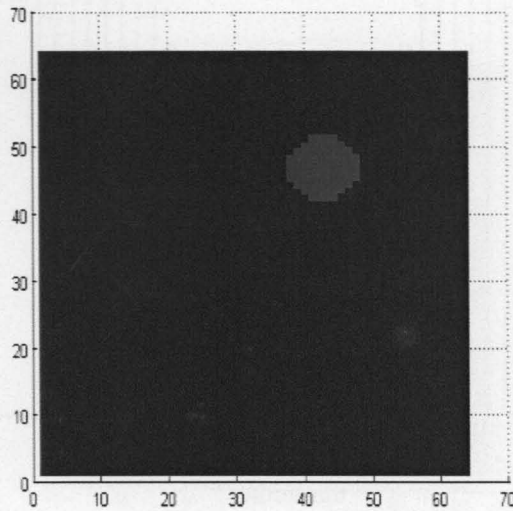
Figure 5.18 a
The actual cross sectional profile of the cylindrical dielectric pipeline
$(\varepsilon = 10, \sigma = 0.01 s/m)$
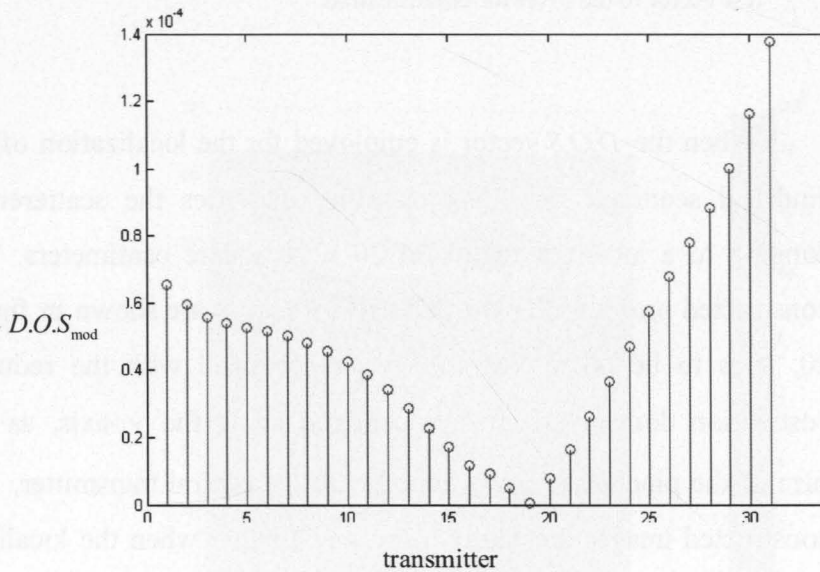
Figure 5.18 b

The $D.O.S_{mod}$ vector for the scatterer in figure 5.a is plotted above. It indicates that the measurement domain is to be moved to the right in the x-direction by three transmitter spacing so that the $D.O.S$ minimum will be aligned with the central transmitter 16.
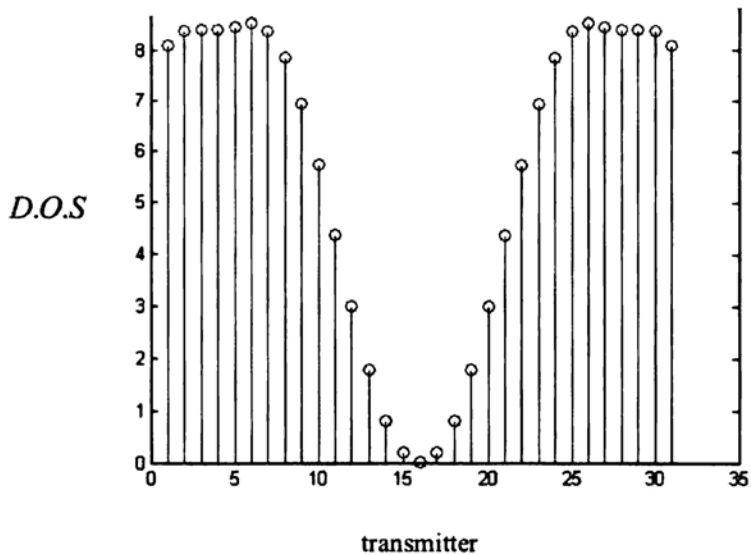
Figure 5.18 c
The *D.O.S* vector for the pipeline after the measurement array has been shifted by three units to the right. This is now presented as the test vector to the PNN for classification.

When the *D.O.S* vector is employed for the localization of the cylindrical scatterer, the PNN classifier classifies the scatterer as belonging to a localized region of 20 x 20 square centimeters. The reconstructed profiles after the 8th DBIM iteration are shown in figure 5.20. It is to be noted that the images obtained with the reduced investigation domain are always centered about the *y*-axis, as the centre of the pipeline is now aligned with the central transmitter. The reconstructed images are found to be much better when the localized imaging domain is employed than when the entire imaging domain is employed, in addition to reducing the computation time.
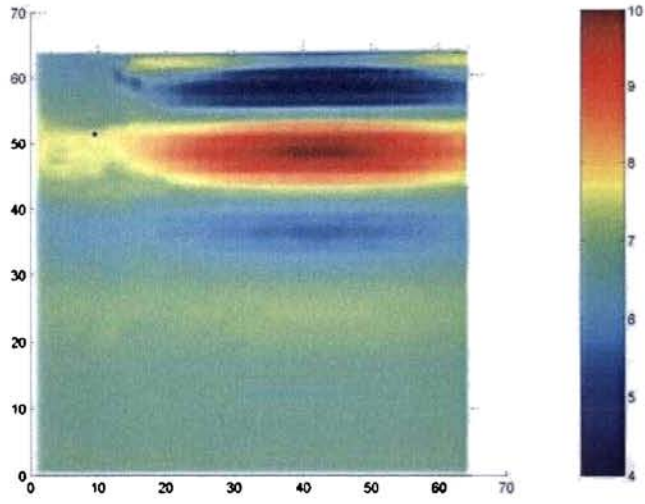
Figure 5.19 a
The reconstructed permittivity considering the entire investigation domain
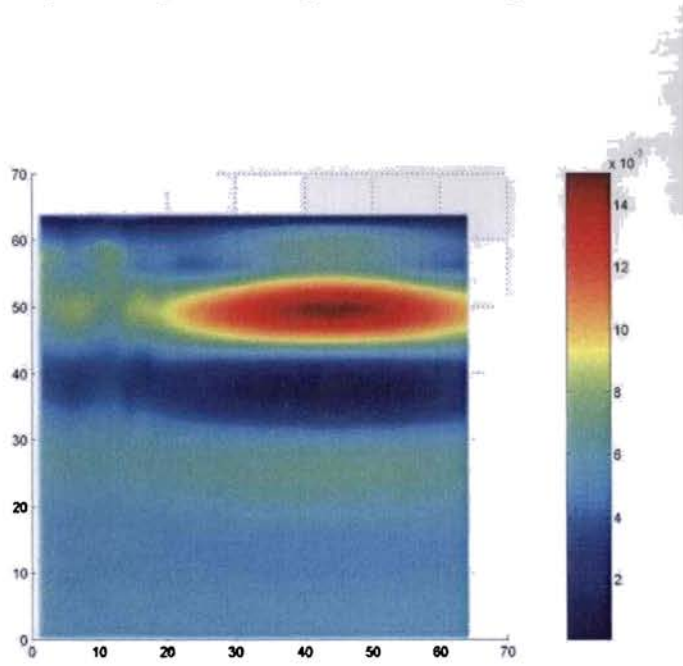
Figure 5.19 b
The reconstructed conductivity considering the entire investigation domain
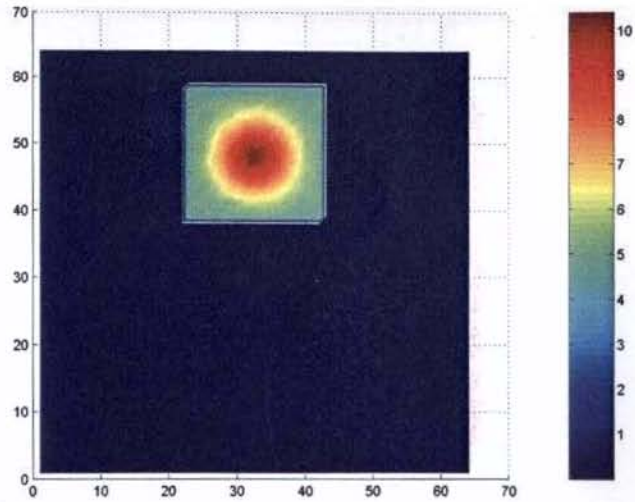
Figure 5.20 a
The reconstructed permittivity with a reduced investigation domain
The coordinate system has been shifted so that the centre of the pipeline cross section lies on the y-axis
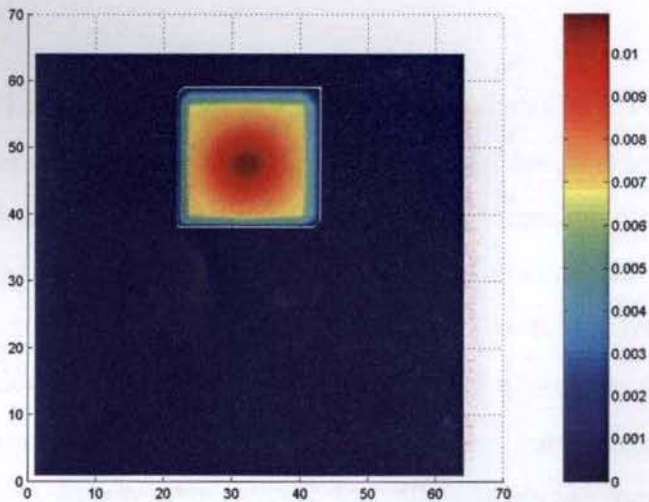
Figure 5.20 b
The reconstructed conductivity with a reduced investigation domain
The coordinate system has been shifted so that the centre of the pipeline cross section lies on the y-axis

References

1. Qing, A. and C. K. Lee, "Microwave Imaging of Parallel Perfectly Conducting Cylinders using Real Coded Genetic Algorithm coupled with Newton Kantarovich Method", *Progress in Electromagnetic Research, PIER* 28, pp 275-294, 2000.

2. Rekanos, I. T., M S. Efraimidou and T. D. Tsiboukis, "Microwave Imaging: Inversion of Scattered Near Field Measurements", *IEEE Transactions on Magnetics*, Vol. 37, No.5, pp 3294 – 3297, September 2001.

3. Guillermin, R., P. Lasaygues, J. P. Sessarego and A Wirgin, "Imaging an object buried in the sediment bottom of a deep sea by linearized inversion of synthetic and experimental scattered acoustic wavefields", *Inverse Problems*, 16, 1777-1797, 2000.

4. Baussard. A, E. L. Miller, D. Lesselier, "Adaptive Multiscale Reconstruction of Buried Objects", *Inverse Problems*, 20, S1-S15, 2004.

5. Chaturvedi. P. and R. G. Plumb, "Electromagnetic Imaging of Underground Targets using Constrained Optimization", *IEEE Transactions on Geoscience and Remote Sensing,* Vol. 33, No. 3, pp 551-561, May 1995.

6. Cui, T. J., W. C. Chew, A. A. Aydiner and S. Chen, "Inverse Scattering of Two- Dimensional Dielectric objects buried in Lossy Earth using the Distorted Born Iterative Method", *IEEE Transactions on Geoscience and Remote Sensing*, Vol. 39, No:2, pp 339-346, February 2001

7. Cui, T. J., Y. Qin, G. L. Wang and W. C. Chew, " Low Frequency detection of two-dimensional buried objects using high-order extended Born approximation", *Inverse Problems*, 20, S41-S62, 2004.

8. Ellis, G.A. and I. C. Peden, "An Analysis Technique for Buried Inhomogeneous Dielectric Objects in the presence of an Air-Earth Interface", *IEEE Transactions on Geoscience and Remote Sensing*, Vol. 33, No. 3, pp 535-540, May 1995.

9. Chew W.C., *Waves and fields in inhomogeneous media*, New York, IEEE Press, 1995.

10. Slaney M, Azimi M, Kak A.C, Larsen L E, "Microwave imaging with first order diffraction tomography", *Medical applications of microwave imaging*, pp 184-211, IEEE Press New York, 1986)

11. Franchois A. and C. Pichot, "Microwave Imaging-complex permittivity reconstruction with a Levenberg-Marquardt Method", *IEEE Transactions on Antennas and Propagation*, Vol. 45, no.2, pp 203-215, February 1997.

12. Tijhuis, A. G., K. Belkebir, A. C. S. Litman and B. P. de Hon, " Theoretical and Computational Aspects of 2-D Inverse Profiling", *IEEE Transactions on Geoscience and Remote Sensing*, Vol. 39, No. 6, pp 1316-1329,June 2001.

13. Wasserman, P. D., *Advanced Methods in Neural Computing*, Van Nostrand Reinhold, New York, 1993.

14. Caorsi, S. and P. Gamba, Electromagnetic detection of dielectric cylinders by a neural network approach, IEEE Trans. Geosci. Remote sensing, vol. 37, pp 820-827, March 1999.

15. Bermani, E., S. Caorsi and M. Rafetto, A microwave object recognition approach based on neural networks, IEEE instrumentation and measurement technology conference proceedings, pp 1582-1585, Venice, May 1999.

16. Bose, N. K. and P Liang, *Neural Network Fundamentals with Graphs, Algorithms and Applications*, Tata McGraw-Hill, New Delhi, 1996.

17. Specht, D. F., Probabilistic Neural Networks for Classification, Mapping or Associative Memory, Proceedings of the IEEE International Conference on Neural Networks, vol.1, pp. 525 – 532, IEEE Press, New York, 1988.

18. Witten, A. J., J.E. Molyneux, and J.E. Nyquist, Ground Penetrating Radar Tomography: Algorithm and case studies, IEEE Trans. Geosci. Remote sensing, vol. 32, pp 461-467, 1994.

19. Deming R. and A.J. Devaney, Diffraction tomography for multi-monostatic ground penetrating radar imaging, Inv. Problems, vol. 13, pp 29-45, 1997.

20. Souriau, L., B. Duchene, D. Lesselier, and R. Kleinman, Modified gradient approach to inverse scattering of binary objects in stratified media, Inv. Problems, vol. 12, pp 463-481, 1996.

21. Lambert, M., D. Lesselier and B. J. Kooij, The retrieval of a buried cylindrical obstacle by a constrained modified gradient method in the H-polarization case and for Maxwellian materials, Inv. Problems, vol. 14, pp 1265-1283, 1998.

CHAPTER 6

Experimental setup for monochromatic inverse scattering

6.1 Introduction

Experimental verification of the algorithms for the inverse scattering problem of microwave imaging can be found in literature. Karg described an experimental setup that employs multiple frequency illumination for microwave imaging [1].Larsen and Jacobi reported microwave scattering parameter imaging results on an isolated canine kidney [2]. Chang et al designed a tomographic microwave imaging system for nondestructive evaluation and object recognition of civil structures and materials [3]. Franchois et al described a 2.45 GHz planar microwave camera for qualitative imaging [4]. Semenov et al developed experimental prototypes for two dimensional and three dimensional microwave imaging for biological purposes [5, 6]. Belkebir et al described an experimental setup for the two dimensional microwave imaging problem of infinite cylinders illuminated by TM polarized incident field [7]. A 434 MHz circular complex permittivity scanner was employed for biomedical imaging experiments by Franchois and Tijhuis [8]. Meaney et al developed a laboratory-scale microwave imaging system for non-invasive temperature monitoring [9]. A microwave imaging system for experimental investigation of tumor detection in multilayer breast phantoms was proposed by Li et al [10]. Tomohisa et al proposed a reflection type system with a two way

antenna for microwave imaging [11]. The experimental data generated at the Ipswich test site of the Rome Laboratory, Hanscom Air Force Base have been used by some authors to verify the accuracy of the algorithms for the inverse scattering problem of microwave imaging [12-15].

6.2 Mechanical specifications of the apparatus for the inverse scattering experiment

An apparatus for monochromatic inverse scattering of two dimensional scatterers illuminated by TM polarized microwaves for experimental verification of the Degree of Symmetry ($D.O.S$) formulation is described here. The apparatus is as shown in figure 6.1.
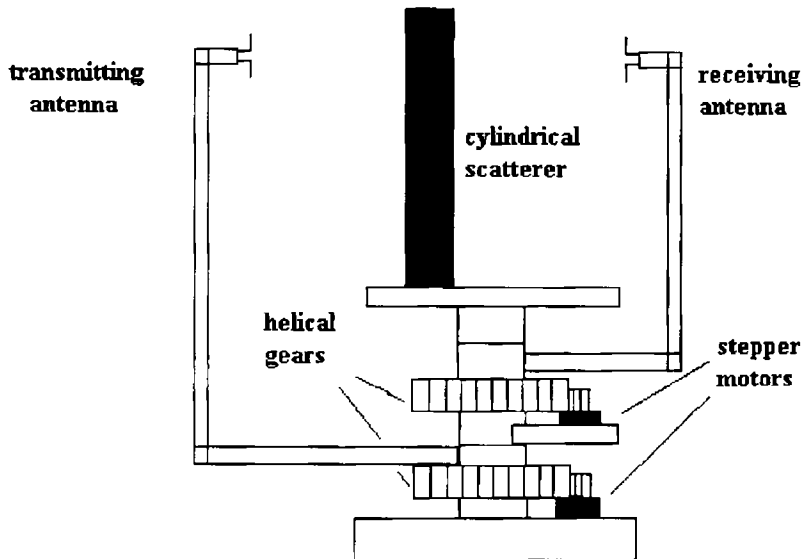
Figure 6.1
Schematic of the
measurement apparatus

The body of the apparatus was built almost exclusively of polymethyl methacrylate (PMMA), which is the synthetic polymer of methyl methacrylate [16]. It is highly transparent and goes under the trade names Plexiglass, Perspex, Acrylex, Lucite etc. Perspex is a nearly lossless material [17], [18]. The only metallic parts of the measurement setup were the bipolar stepper motors employed for rotating the transmitter and receiver antennas. Thus the scattering from the measurement setup was minimized. A circular geometry was employed for the apparatus since scattered information was collected all around the object for each incidence [19]. The transmitter and receiver antennas were rotated by means of 10 kg cm bipolar stepper motors operated in full step. The torque was improved by reducing the rotation speed by means of helical gears, which had a gear ration of 1:4. Helical gears were preferred to spur gears because of their ability to take more torque than spur gears and to operate smoothly [20]. The gears were fabricated on Perspex disks.

Dipole antennas were employed as transmitting and receiving antennas. The transmitting and receiving antennas were moved in a circular measurement domain. The radius of the transmitting and receiving measurement domains were 90 and 80 centimeters respectively. The transmitting and receiving antennas were stepped every 9 degrees. For every transmitter position the receiving antennas stepped through 360 degrees. The investigation domain was chosen as a square centrally located within the measurement domain. The plots of the reflection parameter s_{11} for the transmitting and receiving antennas with frequency were as shown in the figures 6.2 and 6.3. The frequency employed for imaging was 1.8 GHz, where the antennas have the maximum radiation.
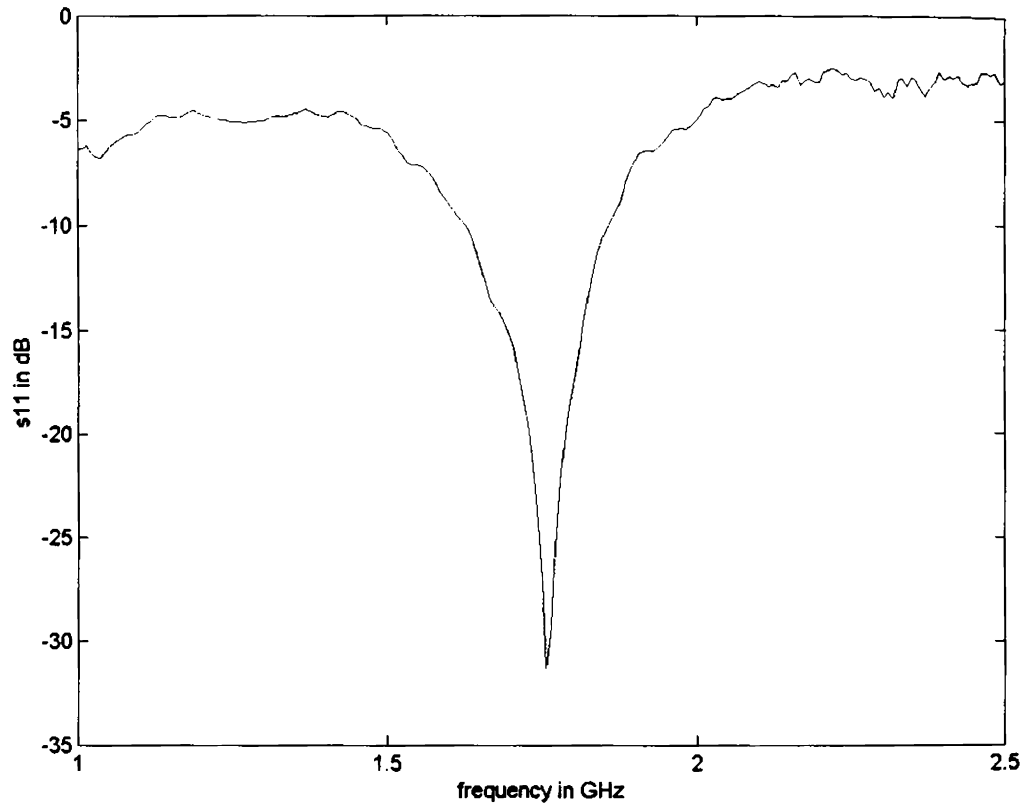
Figure 6.2
Plot of s_{11} with frequency for the
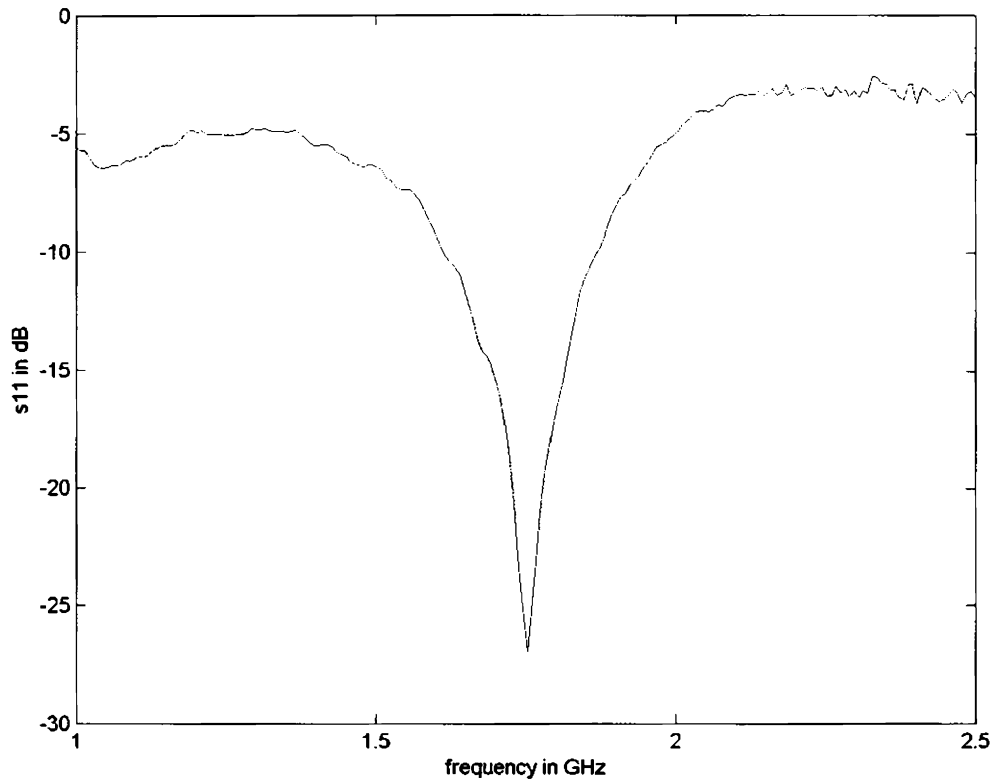transmitting antenna

Figure 6.3
Plot of s_{11} with frequency for the
receiving antenna

The incident field was modeled using the TM polarized infinite line
source expression of equation 5.1.The data acquisition was done
employing the Agilent 8714 ET network analyzer, interfaced to a
workstation via HPIB interface. The controlling of the stepper motor
movements and making of the measurements were done by using an

efficient program written in HP Basic. The measurements were made in the anechoic chamber facility at the Department of Electronics, CUSAT, so that spurious signals arising due to scattering from structures other than the object under investigation could be minimized. The measurement setup was as in figure 6.4
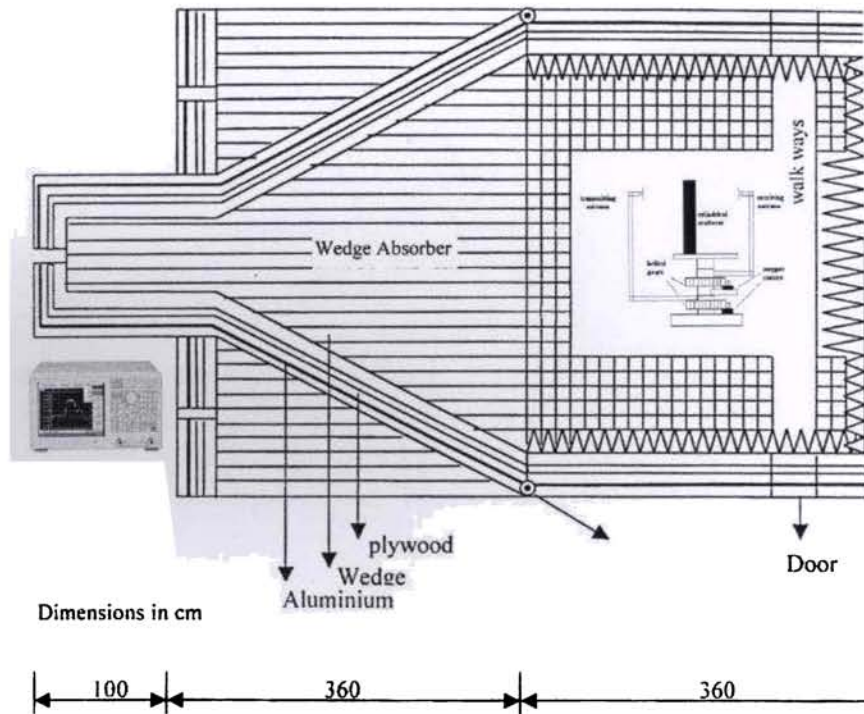
Figure 6.4
The measurement setup with the measurement apparatus in the anechoic chamber The measurements are made using the Agilent 8714 ET network analyzer.

The figure 6.5 shows a comparison between the computed scattered field and the measured scattered field in the measurement domain. The computation assumes a hollow dielectric cylinder of circular cross section with diameter 2 inches and relative permittivity $\varepsilon_r = 3$, centered in the investigation domain, whereas for the experiment, a hollow PVC

(which is nearly lossless and has a permittivity of roughly 3) cylinder of 2 inches diameter was placed at the centre of the investigation domain. The antenna gain was measured by comparing the on-axis measured incident field to the normalized incident field computed using the infinite line source expression.
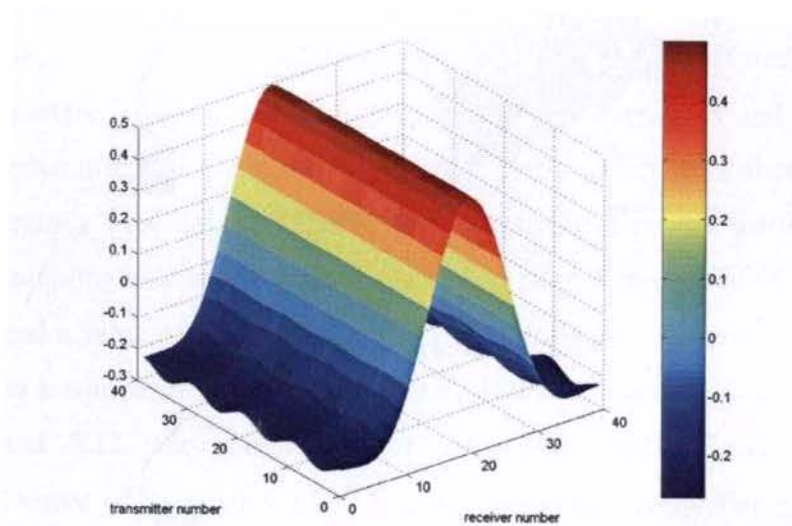
Figure 6.5 a
Real computed scattered field
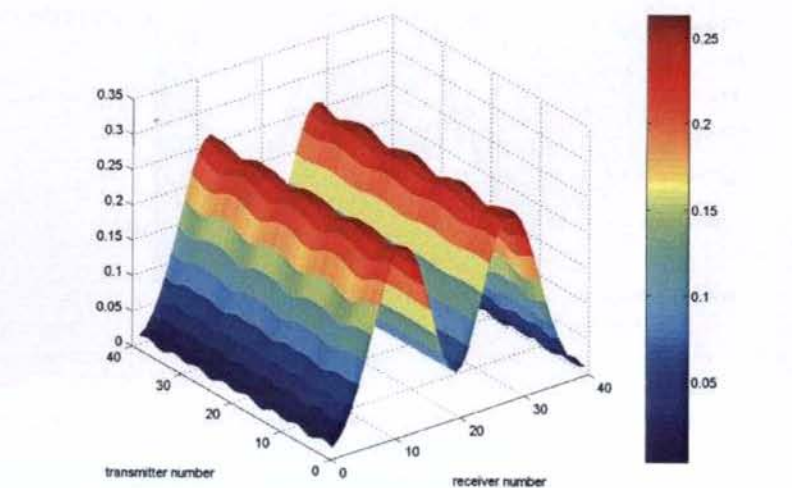
Figure 6.5 b
Imaginary computed scattered field
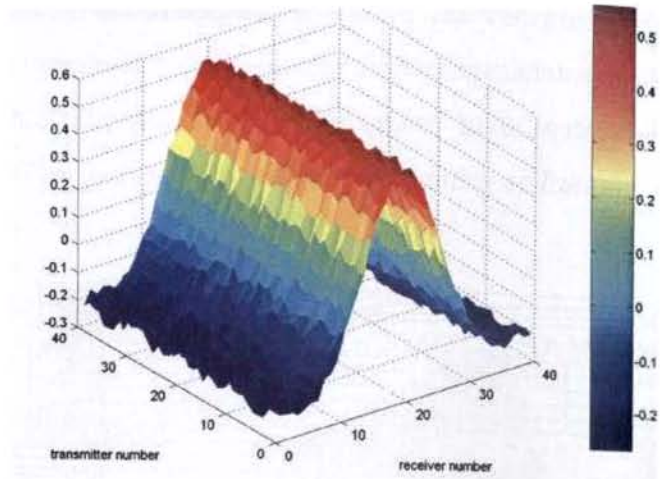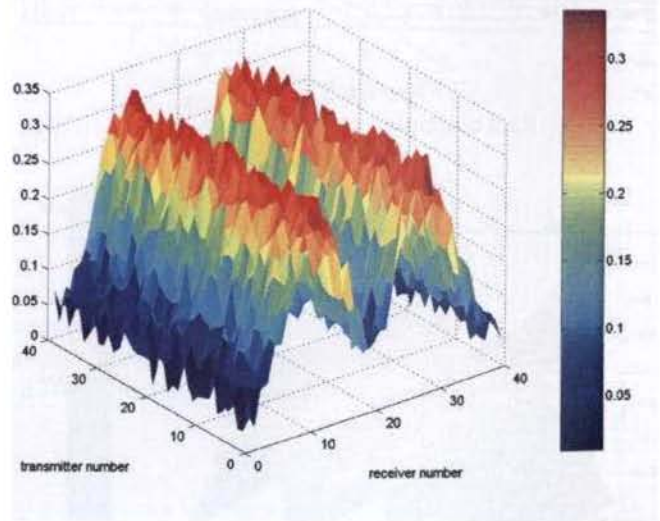
Figure 6.5 c
Real measured scattered field

Figure 6.5 d
Imaginary measured scattered field

6.3 Results and Discussions

The applicability of the Degree of Symmetry formulations for the practical case of Limited Angle Tomography was verified experimentally. Different dielectric scatterer configurations of circular cross section were employed for the experimental verification of the *D.O.S* formulations. Synthetic scattered data were generated with the scatterer configurations, employing the equations 3.25 and 3.26, for generating the Degree of Symmetry plots, which were then used to train a Probabilistic Neural Network to localize the scatterer. The sampling rate was 0.05λ which at the selected frequency of 1.8 GHz, had a value of 0.84 centimeters. The investigation domain was chosen as a square of side 125 pixels, i.e., 105 centimeters. Equations 5.11 and 5.12 were employed for calculating the *D.O.S* and Modified Degree of Symmetry $(D.O.S_{mod})$ Vectors respectively. For employing the *D.O.S* formulations, the transmitter and receiver antennas were rotated so that the minimum value of $D.O.S_{mod}$ coincided with the central transmitter, as illustrated in figure 6.6.
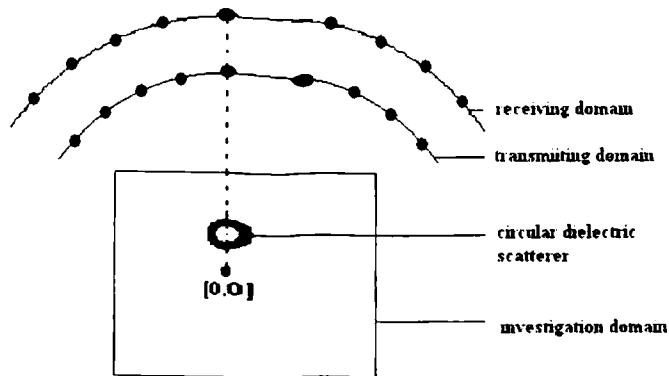

Figure 6.6
The scatterer cross section centre, centre of the investigation domain and the central transmitter and receiver are radially aligned.

Thus the scatterer cross section centre was now radially offset from the central transmitter. The Probabilistic Neural Network was trained with the *D.O.S* vectors computed from the synthetic scattered field. For generating the synthetic scattered field vectors, the scatterer radii were varied from 5 sampling intervals to 10 sampling intervals. The relative permittivity of the cylinder was varied in the range 1 to 10. The offset of the centre of the scatterer from the centre of the imaging domain was varied in steps of 1 sampling interval. The pattern layer weight matrix was derived from the *D.O.S* vectors, with a radial basis function centered at each training case. The weight matrix of the summation layer was derived from the target class. The reduced investigation domains were chosen as squares of dimension 32 x 32 pixels. The reduced domains were chosen to be overlapping by the maximum radius of the scatterer in them so that the possibility of the scatterer not being fully located in either of the reduced regions was avoided.

Hollow poly vinyl chloride pipes were chosen as the scatterers to be imaged. The experiments were repeated for the stronger scattering case of the poly vinyl chloride pipes filled with water. The incident field at the measurement domain was measured by performing the experiment without the scatterers in the investigation domain. The following results illustrate the advantages offered by the *D.O.S* formulations in reconstructing the scatterer cross section. Here a PVC pipe of 2 inch diameter was the object under test. 19 transmitter antenna positions were employed for the reconstructions, with the receiving antenna stepping through 19 measurement points for each transmitter position, as in figure 6.6. The figures 6.7 to 6.11 show the

reconstructions obtained by employing the DBIM procedure on the entire investigation domain.
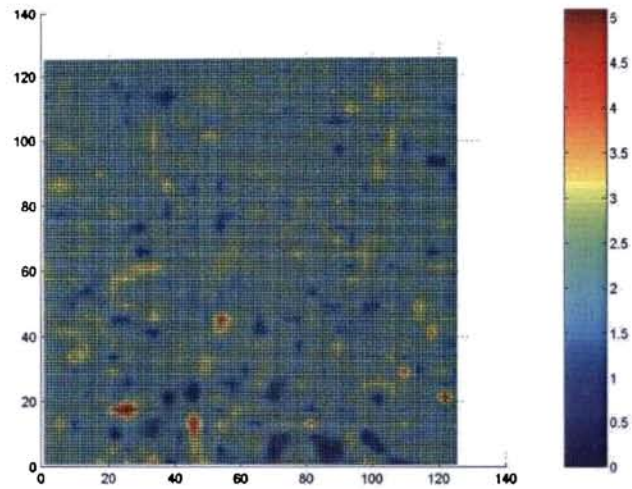

Figure 6.7
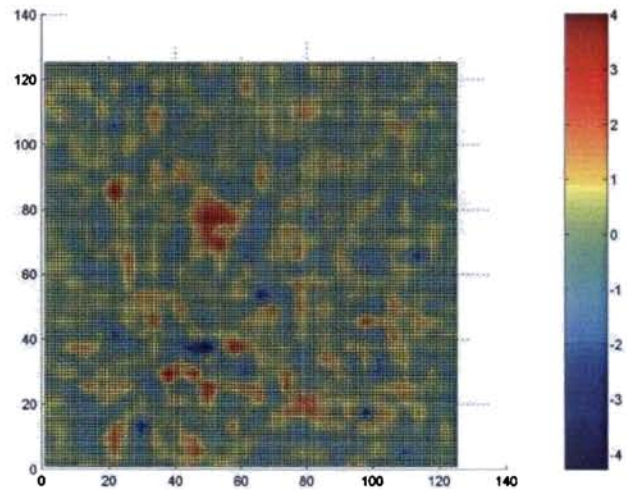First iteration of the DBIM Procedure on
the entire domain

Figure 6.8
10th iteration of the DBIM procedure on
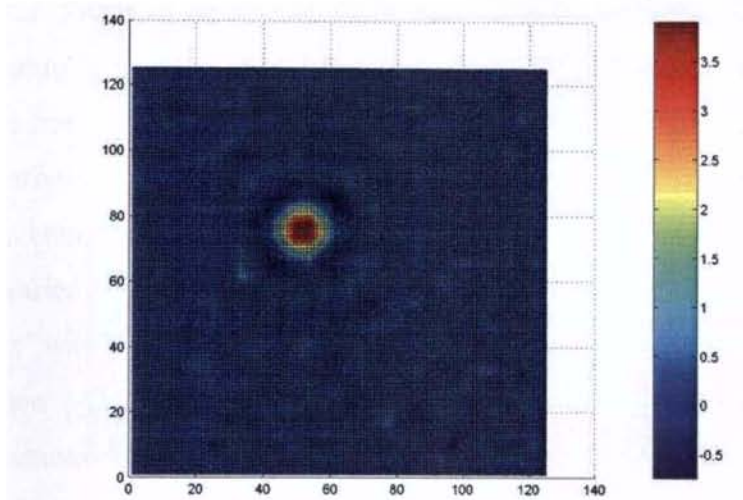the entire domain

Figure 6.9
30th iteration of the DBIM procedure on
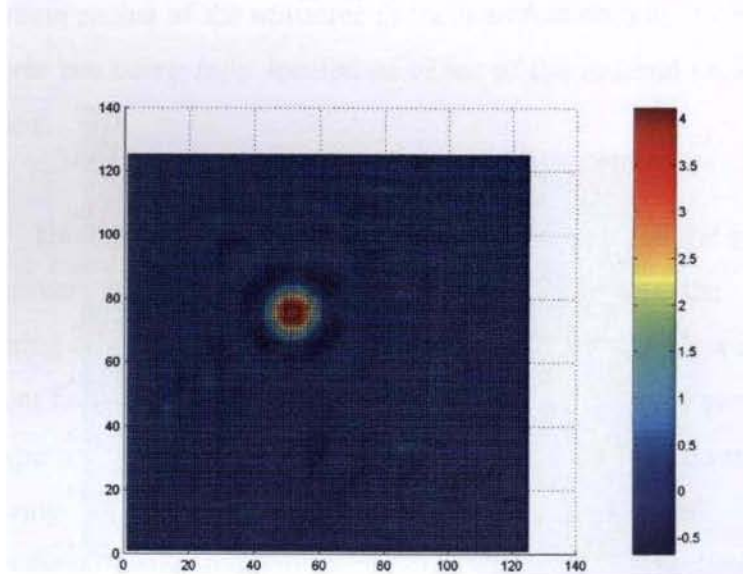the entire imaging domain

Figure 6.10
60th iteration of the DBIM Procedure on
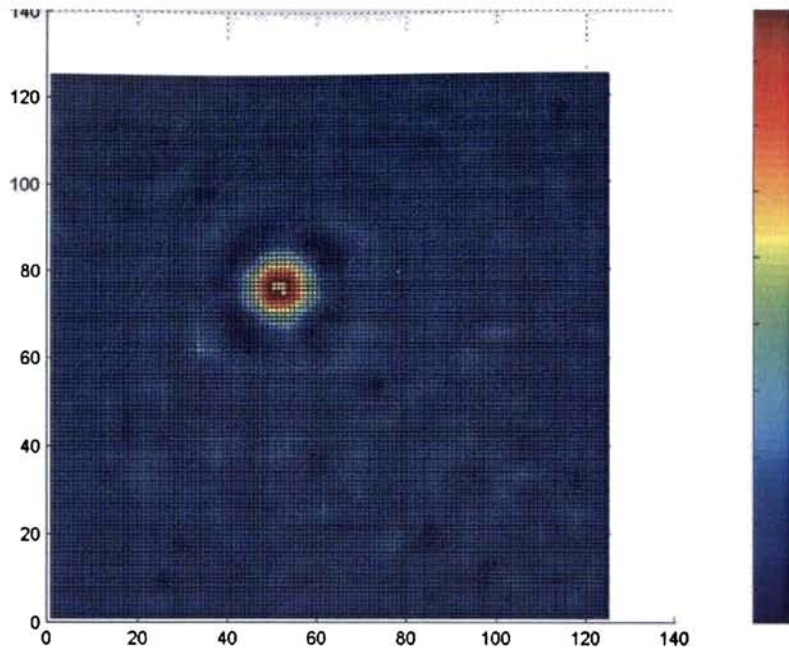the entire imaging domain

Figure 6.11
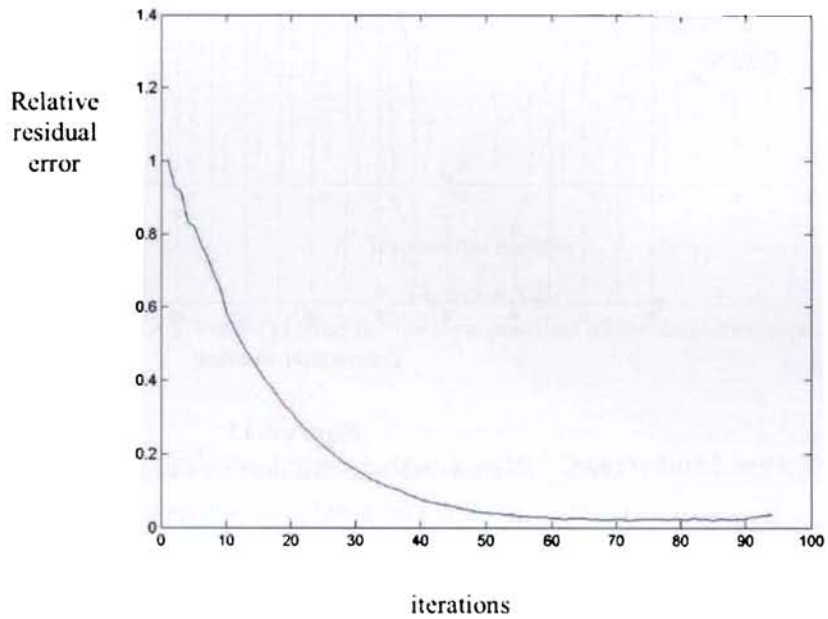Reconstructed image after 90 DBIM iterations on the entire domain

Figure 6.12
The relative residual error is seen to increase after the
90th iteration.

The DBIM iterations were sought to be terminated when the relative residual error $Err(\psi^s)$ fell below 0.02. However $Err(\psi^s)$ was seen to increase after the 90th iteration as shown in figure 6.12. Hence the iterations were terminated after the 90th DBIM step even though the termination criterion was not met. The reconstruction shows that the relative permittivity was poorly reconstructed, especially the value (of air) inside the hollow cylinder, as illustrated in figure 6.11.

The Modified Degree of Symmetry $D.O.S_{mod}$ vector for the scatterer were computed and are shown plotted in the figure 6.13.
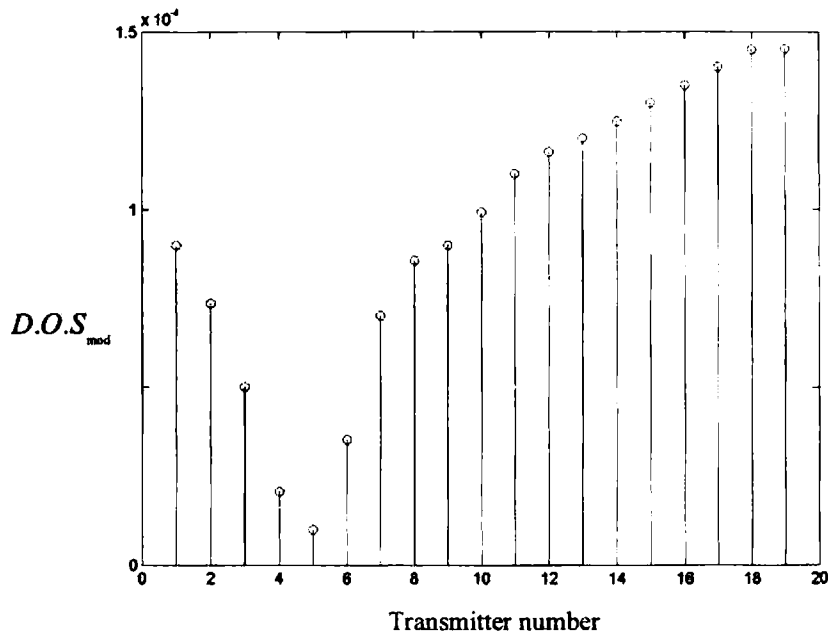

Figure 6.13

$D.O.S_{mod}$ Vector indicates that the measurement setup is to be moved to the left horizontally with respect to the dielectric pipe so that the scatterer, centre of the imaging domain and the central transmitter are radially aligned.

The $D.O.S_{mod}$ vector shows that the measurement setup is to be moved horizontally to the left with respect to the imaging domain, so that the dielectric pipeline and the centre of the imaging domain are radially aligned to the central transmitter. In the experiment, the scatterer was moved to the right so that it was aligned with the central transmitter. The $D.O.S$ vector was computed with the new position of the dielectric scatterer and is shown plotted in figure 6.14.
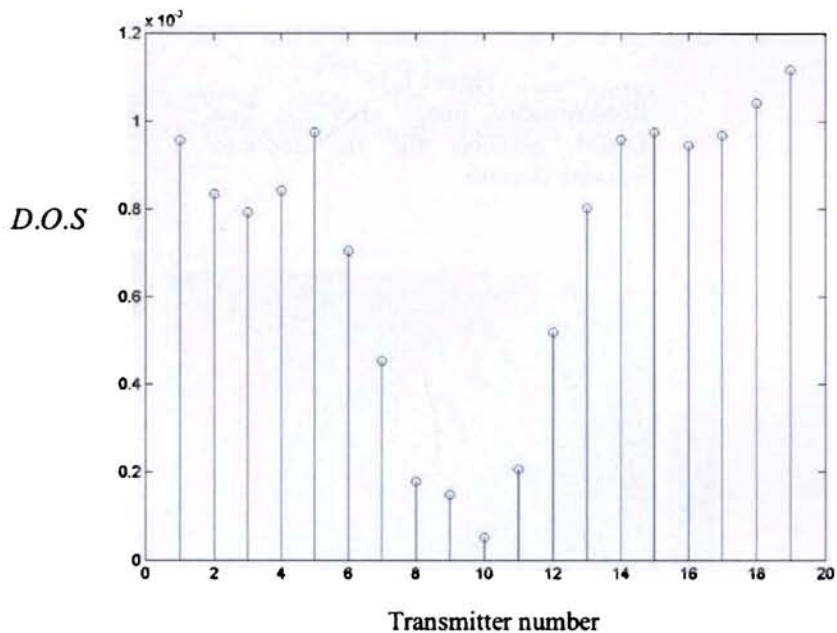

Figure 6.14
$D.O.S$ Vector plotted for the new position of the dielectric pipe.

The Probabilistic neural network which was trained with the simulated $D.O.S$ vectors classified the computed $D.O.S$ vector into a reduced imaging region of 32 x 32 pixels. The figures 6.15 to 6.19 show the results obtained by employing the reduced imaging domain.
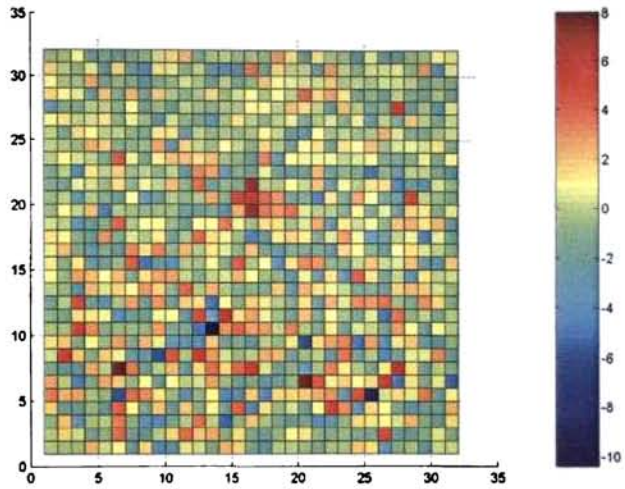
Figure 6.15
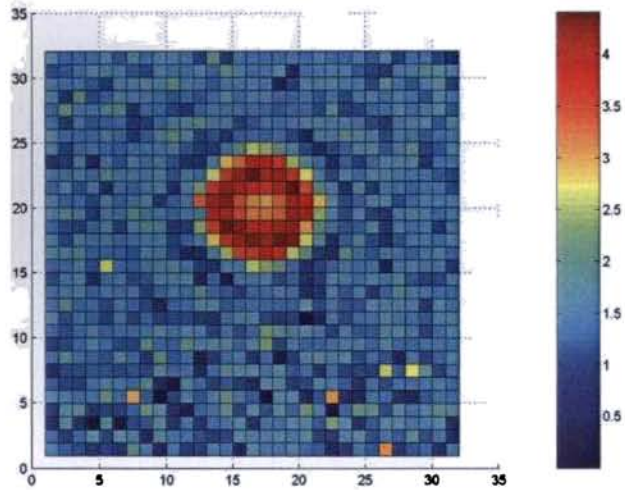Reconstructed image after the first DBIM iteration for the reduced imaging domain

Figure 6.16
Reconstructed image after the 10th DBIM iteration for the reduced imaging domain
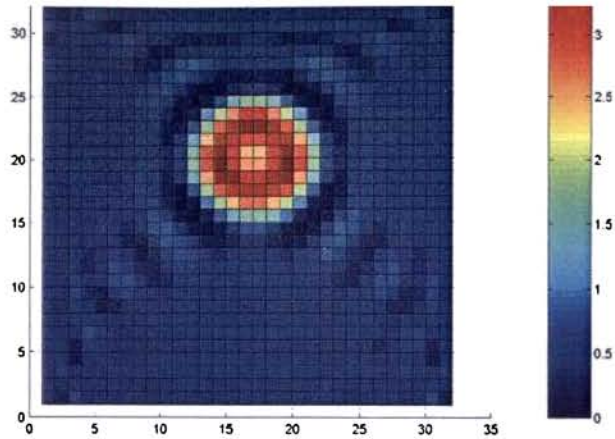
Figure 6.17
Reconstructed image after the 20th DBIM iteration for the reduced imaging domain

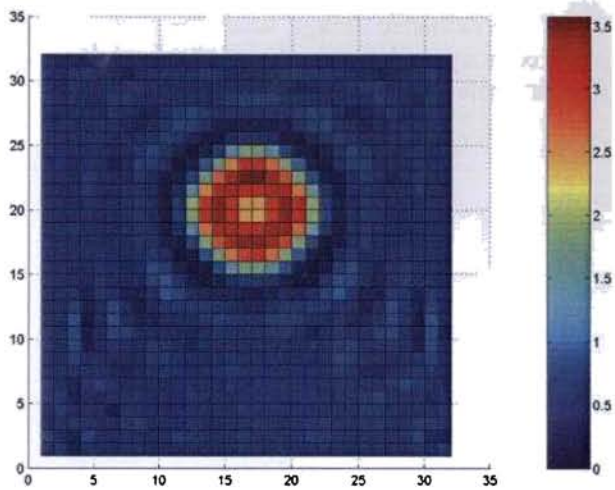**Figure 6.18**
Reconstructed image after the 25th DBIM iteration for the reduced imaging domain
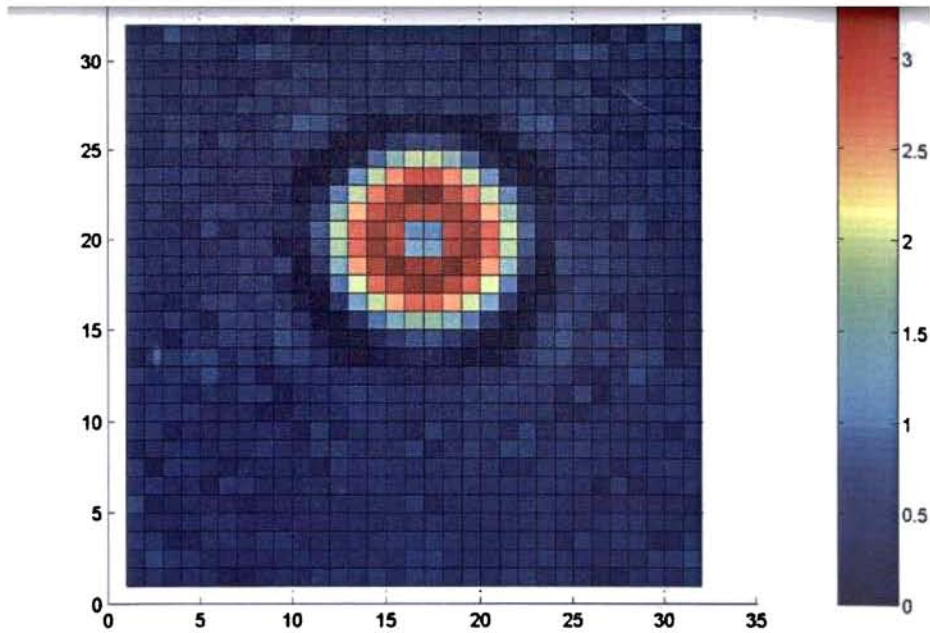
Figure 6.19
Final reconstructed image after the 32nd DBIM iteration for the reduced imaging domain. The relative permittivity (that of air) inside the dielectric cylinder has been reconstructed well.
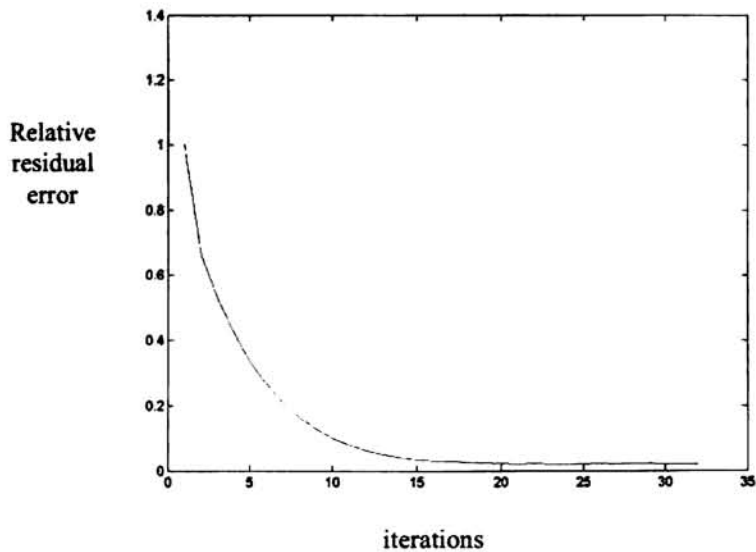

iterations

Figure 6.20
The relative residual error versus DBIM iterations

Figure 6.20 shows the variation of the relative residual error with the DBIM iterations. The termination criterion was met at the end of the 32nd iteration, where the DBIM procedure was stopped. The final reconstructed image is shown in the figure 6.19. The dielectric pipe was better localized and the permittivity values within the pipe reconstructed better, when compared to the result obtained with the entire domain in figure 6.11, thus illustrating the advantages of the *D.O.S* formulations. The DBIM procedure with the reduced domain converged much faster, when compared to the entire domain iterations.

The experiment was also repeated for the strong scattering case of the dielectric cylinder filled with water. The final real and imaginary parts obtained with the DBIM procedure on the entire domain figures 6.21a and 6.21b respectively.
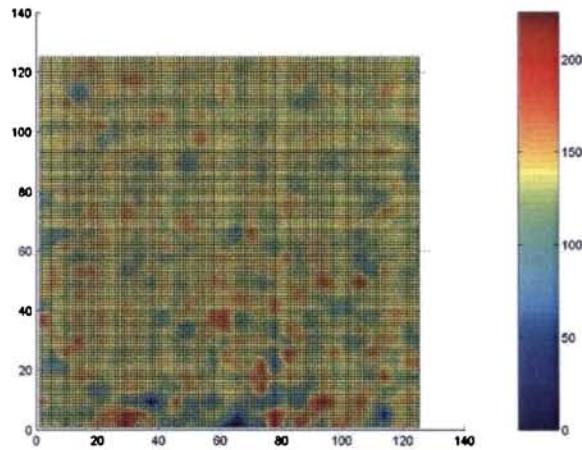
Figure 6.21 a
Reconstructed real part of the scatterer permittivity cross section at the 51st DBIM iteration.
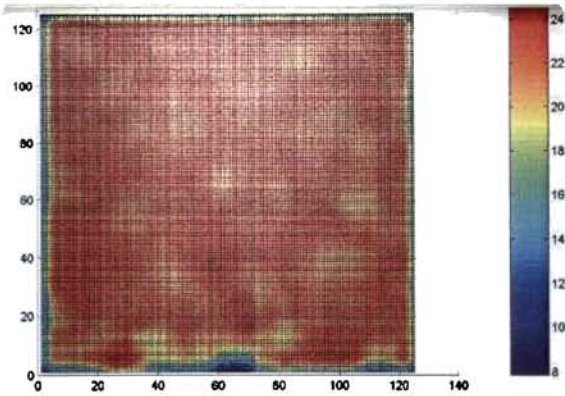
Figure 6.21 b
Reconstructed imaginary part of the
scatterer permittivity cross section at the
51st DBIM iteration

The DBIM iterations are stopped after the 51st iterations as the relative
residual error was found to increase as shown in figure 6.22. Evidently
the solution has been trapped in a local minimum.
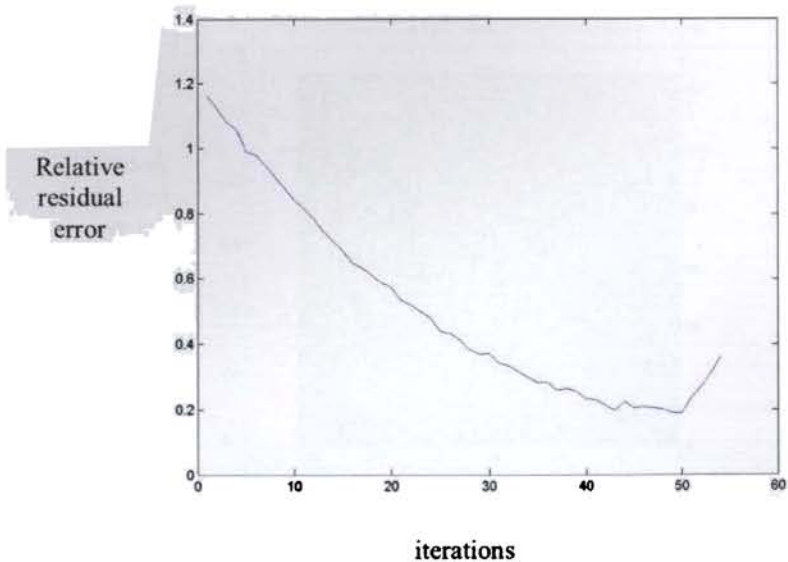
iterations

Figure 6.22
Relative residual error is found to
increase after the 51st iteration. The
DBIM procedure is terminated after the
51st iteration

The reconstructed images obtained with the reduced imaging domain employing the *D.O.S* formulations are shown in figure 6.23.
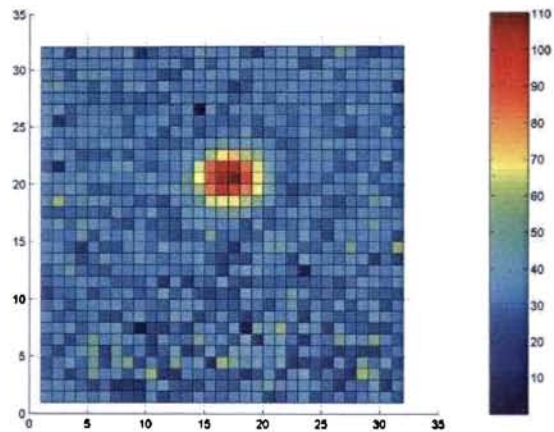
Figure 6.23a
The reconstructed real part of the permittivity profile of the scatterer cross section after the 50th iteration
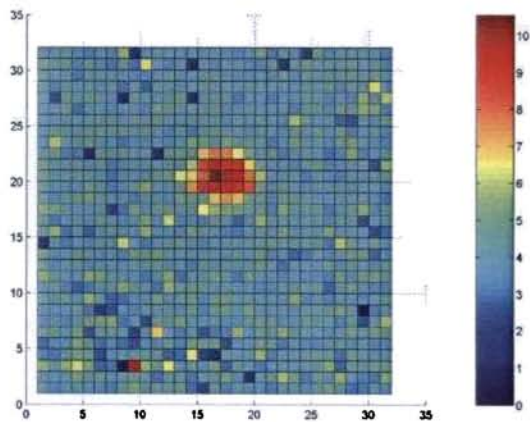
Figure 6.23b
The reconstructed imaginary part of the permittivity profile of the scatterer cross section after the 50th iteration
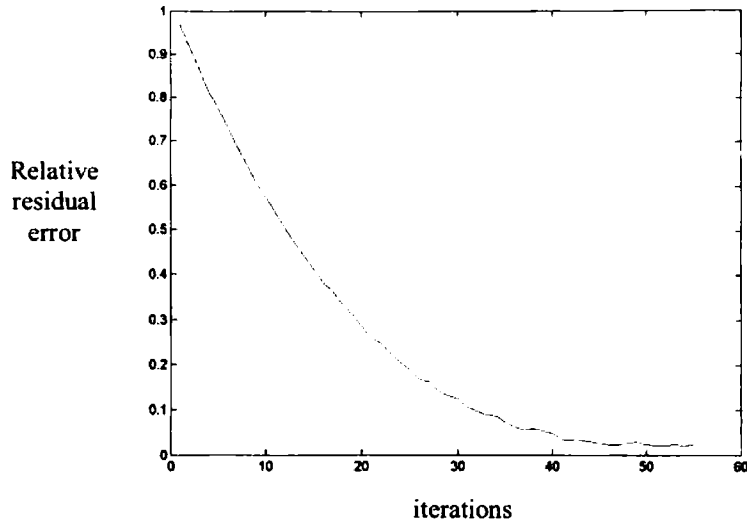
Figure 6.24
The relative residual error versus DBIM iterations

The reconstructions obtained by considering the entire domain in figure 6.20 are not acceptable. The reconstructions obtained employing the reduced imaging domain in figure 6.23, though not ideal, clearly show the location of the scatterer in the investigation domain. The iterations are stopped after the 50th iteration as there was no significant decrease in the relative residual error after that, as illustrated in figure 6.24. Thus the images reconstructed employing the D.O.S formulations were found to be much superior, in addition to significantly decreasing the computation time.

A photograph of the measurement setup in the anechoic chamber is shown in figure 6.25.

Figure 6.25
The measurement setup in the anechoic
chamber facility of DOE, CUSAT

References

1. Karg, R., "Experiments with a multifrequency microwave imaging system", *Nachrichtentechnische Zeitschrift*, vol. 30, p. 651-654, Aug. 1977.

2. Larsen, L. E. and J. H. Jacobi, "Microwave scattering parameter imaging on an isolated canine kidney", *Medical Physics*, Vol. 6, pp 394-403, 1979.

3. Chang, M., P. Chou, H. Lee, "Tomographic microwave imaging for nondestructive evaluation and object recognition of civil structures and materials", *29th Asilomar Conference on Signals, Systems and Computers (2-Volume Set)*, p. 1061, 1995.

4. Franchois, A., A. Joisel, C. Pichot and J. C. Bolomey, "Quantitative Microwave Imaging with a 2.45 GHz Microwave camera", IEEE Transactions on Medical Imaging, Vol. 17, issue 4, pp 550-561, August 1998.

5. Semenov, S. Y., R. H. Svenson, A. E. Boulyshev, A. E. Souvorov, V. Y. Borisov, Y. Sizov, A. N. Starostin, K. R. Dezern, G. P. Statsis and V. Y. Baranov, "Microwave Tomography: Two dimensional system for biological imaging", IEEE Transactions on Biomedical Engineering, Vol. 43, Issue 9, pp 869-877, September 1996.

6. Semenov, S. Y., R. H. Svenson, A. E. Boulyshev, A. E. Souvorov, A. G. Nazarov, Y. Sizov, A. E. Pavlovsky, V. Y. Borisov, B. A. Voinov, G. I. Simonova, A. N. Starostin, V. G. Posukh, G. P. Statsis and V. Y. Baranov, "Three dimensional Microwave Tomography: experimental prototype of the system and Vector Born Reconstruction method", IEEE Transactions

on Biomedical Engineering, vol. 46, Issue 8, pp 937-946, August 1999.

7. Belkebir, K. and M. Saillard, "Special section: Testing Inversion Algorithms against Experimental Data", *Inverse Problems*, Institute of Physics Publishing, vol. 17, pp 1565-1571, 2001.

8. Franchois, A. and A. G. Tijhuis, "A quasi-Newton reconstruction algorithm for a complex microwave imaging scanner environment", *Radio Science*, VOL. 38, NO. 2, 2003

9. Meaney P.M., K. D. Paulsen, M. W. Fanning, D. Li, Q. Fang, "Image accuracy improvements in microwave tomographic thermometry: phantom experience", *International Journal of Hyperthermia*, Taylor and Francis publications, Volume 19, Number 5, pp. 534-550(17)September-October 2003.

10. Li,X., S. K. Davis, S. C. Hagness, D. W. van der Weide and B. D. Van Veen, "Microwave Imaging via Space–Time Beamforming: Experimental Investigation of Tumor Detection in Multilayer Breast Phantoms", *IEEE Transactions on Microwave Theory and Techniques*, Vol. 52, No. 8, pp 155 – 181, August 2004.

11. Tomohisa, O., M. Takashi, S. Tsuyoshi, I. Takashi, "Microwave imaging with a two-way antenna", *Papers of Technical Meeting on Instrumentation and Measurement, IEE Japan*, Vol. IM-06, No.16-23, pp1-6, 2006.

12. van den Berg, P., " Reconstruction of media posed as an optimization problem", *Wavefield Inversion*, Springer Publications, 1999.

13. Lu, C. C. and W. C. Chew, "Processing Ipswich data with Local Shape Function Method", IEEE Antennas and Propagation Magazine, Vol. 38, No. 3, pp 511-53, 1996.

14. Lobel. P, C. Pichot, L. Blanc-Fearud and M. Barlaud, "Microwave imaging: Reconstructions from experimental data using conjugate gradient and enhancement by edge preserving regularization", *International Journal of Imaging Systems Technology*, Vol. 8, pp 337-342, 1997.

15. Fiddy, M. A., M. Testorf and U. Shahid, " Minimum Phase based inverse scattering method applied to IPS 008", *Image Reconstruction from incomplete data III, Proceeding of SPIE*, 5562, pp 188-195, 2004.

16. Curtis, J. W., "The effect of pre orientation on the fracture properties of glassy polymers", *Journal of Physics D: Applied Physics*, Vol. 3, pp 1413-1422, 1970.

17. Jeffries, D. J. and A. Kouloris, "Dielectric loading of ADR Antennas, Experimental results", *antenneX*, online issue 69, January 2003.

18. Jamwal, K. K. S and A. Dhar, " Simple and fast technique for measuring dielectric constant of polymers at microwave frequencies", *Review of Scientific Instruments*, Vol. 52, Issue 5, pp 767-769, May 1981.

19. Franchois A. and C. Pichot, "Microwave Imaging-complex permittivity reconstruction with a Levenberg-Marquardt Method", *IEEE Transactions on Antennas and Propagation*, Vol. 45, no.2, pp 203-215, February 1997.

20. Doughty, V.L and A. Vallance, *Design of machine members*, 4th edition, McGraw Hill, 1964.

CHAPTER 7

Conclusion and future directions

7.1 Introduction

The attempt to find out the internal structure of objects using electromagnetic waves is an important aim of scientists in many disciplines ranging from medical diagnostics to non destructive testing. These problems involve the estimation of certain quantities such as dielectric permittivity, conductivity etc based on measurement of the scattered fields. The inverse problem of electromagnetic imaging is highly non linear and the nonlinearity increases with the dielectric contrast and size of the scatterer, as well as the frequency of illumination. These inverse problems are ill-posed and the ill-posedness increases when only a limited angle measurement of the scattered data is possible, as in the case of imaging buried objects. Therefore the electromagnetic inverse scattering problem is characterized by multiple minima. Thus any procedure to solve the inverse problem of electromagnetic imaging is liable to get trapped in local minima. The computation per iteration for finding the solution of the inverse scattering process is of the order of N^3 where N is the number of unknowns of the inverse scattering process. Thus algorithms designed for computing the solution of the inverse

scattering problem of electromagnetic imaging are beset with convergence and computational issues.

The thesis focused on methods for improving the computational and convergence issues of inverse scattering algorithms employed for electromagnetic imaging.

A multi-scale frequency hopping technique was proposed for the purpose of obtaining globally convergent solutions using any deterministic iterative procedure. Since the deterministic procedures employ linearized search methods to minimize a cost functional, they are liable to get trapped in local minima. The Distorted Born Iterative method and the Newton Kantarovich method were employed for the deterministic iterations in this work. The strategy is independent of the exact deterministic search technique employed. The multi-scaled frequency hopping technique employed a multi-resolution search at a frequency hop for the solution of the inverse scattering problem of electromagnetic imaging. The stability of the solution is larger at a coarser sampling rate. Hence its non uniqueness is less prominent at a lower sampling rate. This solution was taken as the starting point for iterations at increasing sampling rates. Thus the multi-resolution strategy will be less prone to local minima problems than fixed grid methods. However the employment of the cost functional may again introduce local minima. Therefore the multi-scaling strategy was combined with the frequency hopping method suggested by W C Chew et al. The combined strategy was tested on synthetic data as well as experimental data provided by the Centre Commun de Ressourses Micro-ondes (CCRM) of Marseille France. The results were compared against those obtained using frequency hopping alone. The proposed strategy yielded results that were closer to the ground truth and were

found to be better localized in the imaging domain. It was also observed that the total computations per iteration were also significantly reduced. This is attributed to the fact that the multi-scaling strategy at the lower frequencies succeeded in providing a better initial estimate for the iterations at the higher frequencies for this object, than when the solution was computed at the finest scales alone.

The Degree of symmetry formulation was introduced in Chapter 5. The investigation domain where the scatterer is searched for has to be sufficiently large to include all possible locations of the scatterer. However when the investigation domain is large, the number of unknowns of the inverse scattering problem of electromagnetic imaging increases and a deterministic search to image the scatterer may fail to reach a convergent solution. The total computation time also increases when the number of elements to be reconstructed increases. It was observed that the symmetry of the measured scattered field vector could be used to localize the scatterer in the investigation domain when the scatterer was symmetric, leading to the *D.O.S* formulations. Synthetic scattered field data was generated to verify the applicability of the formulations. A Probabilistic neural network, trained with the *D.O.S* vectors, classified the scatterer as belonging to a significantly reduced investigation domain. The entire measured scattered field data was therefore available for the reconstruction of fewer number of investigation domain elements. Thus the degrees of freedom of the inverse scattering problem were reduced, which aided the global convergence of the iterations. The *D.O.S* formulations also resulted in more robust reconstructions of the scatterer. The formulations were also applied to the problem of

encouraging results.

An experimental setup was designed for performing the verification of the *D.O.S* formulations. The experimental results confirmed the applicability of the formulations.

7.2 Shortcomings and Sources of Error

The sources of error and accuracy conditions encountered in the work are detailed below.

➢ The Degree of Symmetry formulation is strictly a two dimensional formulation. The two dimensional model where a 2-D scatterer is illuminated by a TM polarized source, which reduces the scattering equations to scalar ones, has to be applicable. Therefore the *D.O.S* formulations cannot be applied for the reduction of imaging domain when the scatterer is 3 dimensional.

➢ Modeling the incident field with a line source: The experimental verification employed a dipole antenna for generating the incident field. More accurate representations should use the field expressions of dipoles, which however, would make the computations more involved.

➢ Reflections from the measurement setup: Ideally the measured scattered field should be contributed by the scattering from the dielectric object whose cross section is to be profiled. To minimize the scattering from the experimental setup, it is built exclusively using PERSPEX, which is nearly lossless.

> Less than ideal performance of the anechoic chamber: The non ideal performance of the anechoic chamber would mean that reflections from the chamber walls also have to be factored in.

7.3 Possible Directions

Some of the possible extensions that maybe pursued are listed below

> Stochastic search algorithms are extremely slow compared to deterministic search algorithms even though they converge globally and hence were not used in this work. It is suggested that stochastic methods such as Genetic algorithms or Simulated annealing be employed, at least at coarse resolutions, to yield more convergent solutions.

> Variable grid methods such as non linear multi-grid relaxation based methods maybe tried out for multi-resolution search of the solution of the inverse scattering problem of electromagnetic imaging.

> Proper selection of the regularization parameter is critical for the quality of the electromagnetic inverse scattering solution. Zeroth order regularization was employed in this work, with an empirical formula used for computing the value of the regularization parameter. More sophisticated methods based on the stochastic model of the reconstruction process maybe tried.

Reference

1. Agilent 8714 ET Network Analyzer operating and
programming manual

Publications

International Journals

1. **Vinu Thomas**, C. Gopakumar, Anil Lonappan, G.Bindu, V Hamsakutty, K.T Mathew " Microwave Imaging of Two-Dimensional Dielectric Cylinders with a Multiscaled Frequency Hopping Approach" , *Microwave and Optical Technology Letters (USA)* , Vol. 43, No. 4, pp 353-355, 20th November 2004

2. **Vinu Thomas**, C. Gopakumar, A. V. Praveen Kumar, V. Hamsakutty, Anil Lonappan, G. Bindu, K. T. Mathew "A novel technique for reducing the imaging domain in microwave imaging of two dimensional circularly symmetric scatterers" , *Microwave and Optical Technology Letters (USA)* Vol. 44, No. 5, pp 423-427, 5th March 2005

3. **Vinu Thomas**, C. Gopakumar, Jaimon Yohannan, Anil Lonappan, G. Bindu, A.V. Praveen Kumar, V. Hamsakutty, K. T. Mathew_"A Novel Technique for Localizing the Scatterer in Inverse Profiling of Two Dimensional Circularly Symmetric Dielectric Scatterers Using Degree of Symmetry and Neural Networks" *Journal of Electromagnetic Waves and Applications(USA)* Vol. 19, No.15, pp 2113-2121, 2005

4. **Vinu Thomas**, J. Yohannan, A. Lonappan, B. Bindu and K.T.Mathew, "Localization of the investigation domain in inverse profiling of buried 2-D Dielectric pipelines with circular cross section using electromagnetic scattered data", *Progress in Electromagnetic research*, PIER 61, 111-131, 2006

5. V Hamsakutty, Anil Lonappan, Joe Jacob, Jaimon Yohannan, **Vinu Thomas**, G.Bindu, K.T Mathew " A Novel Coupling medium for Microwave Medical Imaging" , *IEE Electronic Letters*, Vol. 39, No. 21, pp 1498-1499, 16th October 2003

6. G.Bindu , Anil Lonappan,V Hamsakutty, **Vinu Thomas**, C.K. Aanandan, K.T Mathew " Microwave Characterisation of Breast Phantom Materials" , *Microwave and Optical Technology Letters (USA)* Vol. 43, No.6, pp 506-508, 20th December 2004

7. G.Bindu , **Vinu Thomas**, Anil Lonappan, A. V. Praveen Kumar, V Hamsakutty, C.K. Aanandan, K.T Mathew " Two Dimensional Microwave Tomographic Imaging of Low Water Content Tissues" , *Microwave and Optical Technology Letters (USA)* Vol. 46, No.6, pp 599-601, 20th September 2005

8. G.Bindu, Santhosh John Abraham, Anil Lonappan, **Vinu Thomas,** C.K. Aanandan, K.T Mathew "A pulsed confocal microwave technique for the detection of dielectric contrast of breast tissue" , *Microwave and Optical Technology Letters (USA)* Vol. 47, No.3, pp 209-212, 5th November 2005

9. G.Bindu, Santhosh John Abraham, Anil Lonappan, **Vinu Thomas,** C.K. Aanandan, K.T Mathew "Effects of reduced contrast coupling medium in microwave breast imaging" , *Microwave and Optical Technology Letters (USA)* Vol. 47, No.5, pp 443-446, 5th December 2005

10. G.Bindu, Santhosh John Abraham, Anil Lonappan, **Vinu Thomas,** C.K. Aanandan, K.T Mathew, "Active microwave imaging for breast cancer detection", *Progress in Electromagnetics Research (USA),* PIERS 58, pp.149-169, 2006

11. G.Bindu, Anil Lonappan, **Vinu Thomas,** C.K. Aanandan, K.T Mathew "Dielectric studies of corn syrup for application microwave breast imaging", *Progress in Electromagnetics Research (USA),* PIER 59, pp.175- 186,2006

12. G.Bindu, **Vinu Thomas,** Anil Lonappan, C.K. Aanandan, K.T Mathew "Microwave studies of a Poly Vinyl Acetate (PVA)- Based Phantom for Applications in Medical Imaging" , *Microwave and Optical Technology Letters (USA)* Vol. 48, No.1, pp 180-183, January 2006

13. Anil Lonappan, **Vinu Thomas,** G.Bindu, C. Rajasekharan, K.T Mathew "Analysis of Human Cerebro Spinal Fluid at the ISM Band of Frequencies" , *Journal of Electromagnetic Waves and Applications(USA)* Vol. 20, No.6, pp 773-779, 2006

14. G.Bindu, Anil Lonappan, **Vinu Thomas,** C.K. Aanandan, K.T Mathew, "Dielectric studies of polyvinyl acetate based phantom for application in medical imaging", *Journal of Material Science,* Vol. 41, No. 22, pp 7419-7424, November 2006.

15. G. Bindu, Santhosh John Abraham, Anil Lonappan, **Vinu Thomas,** C K Aanandan and K. T. Mathew, " Two dimensional microwave tomogaraphic imaging of breast tissues", *International Journal of Cancer Research 2(1),* 57-68, 2006.

16. G.Bindu, Santhosh John Abraham, Anil Lonappan, **Vinu Thomas,** C.K. Aanandan, K.T Mathew, "Detection of dielectric contrast of breast tissues using confocal microwave technique", *Microwave and Optical Technology Letters (USA)* Vol. 48, No.6, pp 1187-1190, June 2006

International Conference Papers

1. **Vinu Thomas**, C. Gopakumar, Jaimon Yohannan, Anil Lonappan, G. Bindu, A.V. Praveen Kumar, V. Hamsakutty, K. T. Mathew "A Novel Technique for Localizing the Scatterer in Inverse Profiling of Two Dimensional Circularly Symmetric Dielectric Scatterers Using Degree of Symmetry and Neural Networks" *Electromagnetics Research Symposium, PIERS 2005*, August 22-26, 2005, Hangzhou, China

2. **Vinu Thomas**, C. Gopakumar, A. V. Praveen Kumar, V. Hamsakutty, Jaimon Yohannan, K. T. Mathew, " Imaging Domain reduction in Microwave Imaging of two dimensional circularly symmetric dielectric scatterers using degree of symmetry vector", 2004 December, *Seventh International Conference on Optoelectronics, Fiber optics and Photonics*, Cochin, India.

3. V Hamsakutty, Anil Lonappan, Joe Jacob, G.Bindu , **Vinu Thomas**, A. V. Praveen Kumar, K.T Mathew " Biomedical Applications of Sodium Meta Silicate Gel as Coupling medium for Microwave Medical Imaging" , *2004 IEEE AP-S International Symposium and USNC/URSI National Radio Science Meeting, APS/URSI 2004*, June 20-26, 2004, Monterey, California, USA

4. Jaimon Yohannan, A. V. Praveen Kumar, **Vinu Thomas**, V. Hamsakutty, Anil Lonappan, K. T. Mathew "Half- Split Cylindrical Dielectric Resonator Antenna" , *5th Conference on Ferroelectrics, Ferroelectrics UK 2005*, April 26- 27, 2005, University of Paisley, Scotland, UK

5. A. V. Praveen Kumar, Jaimon Yohannan, Anil Lonappan, G. Bindu, **Vinu Thomas**, V. Hamsakkutty, K. T. Mathew, "Microstripline Fed Circular Sector Dielectric Resonator Antenna", *IEEE AP-S International Symposium and USNC / URSI National Radio Science meeting, APS/URSI 2005*, July 3-8, 2005, Washington DC, USA

6. Anil Lonappan, **Vinu Thomas**, G. Bindu, C. Rajasekharan, K. T. Mathew," Human Colostrum at S-band of Microwave Frequencies" *Progress in Electromagnetics Research Symposium, PIERS 2007*, March 26 – 30, 2007, Beijing, China

7. Jaimon Yohannan, A. V. Praveen Kumar, **Vinu Thomas**, V. Hamsakutty and K. T. Mathew, "Synthesis of Dielectric Resonators for Microwave Filter Designing", *Progress in Electromagnetics research symposium PIERS 2005*, August 2005, Hangzhou, China.

National Conference Papers

1. C. Gopakumar, **Vinu Thomas** and K. T. Mathew, "A Reduction Technique for imaging domain in microwave imaging of two dimensional circularly symmetric scatterers", *Proceedings of the National Seminar on Information, Communication and Intelligent Systems*, February 2008, pp 86-91, Cochin.

2. C. Gopakumar, **Vinu Thomas** and K. T. Mathew, "A Multiscaled frequency hopping approach in the microwave imaging of two dimensional dielectric cylinders", *Proceedings of the National Seminar on Information, Communication and Intelligent Systems*, February 2008, pp 92-97, Cochin.

3. G.Bindu , Anil Lonappan,V Hamsakutty, A. V. Praveen Kumar, **Vinu Thomas**, C.K. Aanandan, K.T Mathew "Microwave imaging of wax cylinders", December 2004, *APSYM 2004, Antennas and Propagation Symposium*, Department of Electronics, Cochin University of Science and Technology, Cochin, India